Turbulent flowfield downstream of a perpendicular airfoil–vortex interaction

Kenneth S. Wittmer

William J. Devenport, Chair
William H. Mason
Wayne L. Neu
Saad A. Ragab
Roger L. Simpson

October 23$^{\text{rd}}$, 1996
Blacksburg, VA

Turbulent flowfield downstream of a perpendicular airfoil–vortex interaction

Kenneth S. Wittmer

(Abstract)

Experiments were performed to document the turbulent flowfield produced downstream of an airfoil encountering an intense streamwise vortex. This type of perpendicular airfoil–vortex interaction commonly occurs in helicopter rotor flows. The experiments presented here thus provide useful information for the prediction of helicopter noise, particularly BWI noise.

Three-component velocity and turbulence measurements were made in unprecedented detail using a computerized miniature four-sensor hot-wire probe system; revealing much about the structure and behavior of this flow over a range of conditions. The interaction between the vortex and the airfoil wake leaves the vortex surrounded by a large region of intense turbulence unlike the turbulence surrounding an isolated vortex. Even for close separations, the vortex core passes the airfoil virtually unchanged. However, vorticity of opposite sign is shed by the airfoil in response to the angle of attack distribution induced by the vortex resulting in an unstable circulation distribution according to Rayleigh's criterion. Simple theoretical models adequately describe the shed vorticity distribution of the airfoil and the unstable circulation distribution it imparts on the vortex.

As the flow develops, the vortex continuously distorts the airfoil wake. The strain rates imparted by the vortex on the spanwise vorticity contained in the airfoil wake result in an anisotropic, turbulence producing stress field. For several chord lengths downstream, the vortex core remains laminar and little change is seen in the unstable circulation distribution. While the vortex core is laminar, turbulent fluctuations measured in the core are the result of inactive wandering motions and the characteristic length and velocity scales of the flat portion of the vortex wake appear to be appropriate scales for the fluctuations. Eventually, the vortex core becomes turbulent as indicated by an increase in high frequency velocity fluctuation levels of more than an order of magnitude. Subsequently, the circulation distribution reorganizes to a stable distribution. A loss in core circulation occurs due to a decrease in the peak tangential velocity which is proportionately larger than the increase in the vortex core radius. The peak tangential velocity decreases to the point where it is exceeded by the axial velocity deficit—another unstable situation. These effects increase with decreased separation between the vortex and the airfoil, but appear to be largely independent of airfoil angle of attack an only weakly dependent upon vortex strength.

Contents

List of Tables

List of Figures

Nomenclature

b	= wind tunnel height and interaction blade span, $1.83\,\mathrm{m}$
c	= chord length, $0.203\,\mathrm{m}$
d	= radial scale of axial velocity profile through the core center
E_c	= temperature corrected bridge output voltage
E_i	= bridge output voltage from i-th sensor
E_m	= bridge output voltage at temperature T_m
f	= frequency, Hz
G_{uu}, G_{vv}, G_{ww}	= u, v, w velocity autospectra respectively
h_i	= pitch sensitivity of i-th sensor
k	= turbulence kinetic energy, $\frac{1}{2}(\overline{u^2} + \overline{v^2} + \overline{w^2})$
L_b	= length scale of interaction blade wake
L_g	= length scale of generator wake
L_s	= generic scaling length
L_w	= average sensor length
P	= turbulence kinetic energy production
Q	= $\sqrt{U^2 + V^2 + W^2}$
Q_e	= $\sqrt{U_\mathrm{e}^2 + V_\mathrm{e}^2 + W_\mathrm{e}^2}$
r	= radial distance from vortex core center
r_1	= vortex core radius measured from the core center to the point of peak tangential velocity
$r_1\vert_{10}$	= vortex core radius at $x/c = 10$
Re_c	= Reynolds number based on chord length
Re_{L_w}	= Reynolds number based on average sensor length
Re_θ	= Reynolds number based on momentum thickness
s, n	= local curve aligned coordinates defined in Figure 3.31
T_c	= constant temperature used for temperature correction
T_m	= measurement temperature
U, V, W	= mean velocities in the x, y, z directions respectively
U_c	= cooling velocity

U_{d} = axial velocity deficit at vortex core center

U_{b} = velocity scale of interaction blade wake

$U_{\mathrm{e}}, V_{\mathrm{e}}, W_{\mathrm{e}}$ = U, V, W velocity estimates respectively

$U_{\mathrm{eff}_{\mathrm{i}}}$ = effective cooling velocity of the i-th sensor

U_{g} = velocity scale of generator wake

U_{s} = generic scaling velocity

U_{s} = generic scaling velocity

U_{∞} = free-stream velocity

u, v, w = fluctuating velocities in the x, y, z directions respectively

V_s, V_n = mean velocities in the s and n directions respectively

V_x = axial velocity in vortex aligned coordinate system

V_θ = tangential velocity in vortex aligned coordinate system

V_{θ_1} = peak tangential velocity of vortex

$V_{\theta_1}|_{10}$ = peak tangential velocity of vortex at $x/c = 10$

v_s, v_n = fluctuating velocities in the s and n directions respectively

x, y, z = coordinates defined in Figure 2.2

α = angle of attack, positive for right hand rotation about the negative y axis shown in Figure 2.2

α_1 = angle of attack of the vortex generator, positive for right hand rotation about the negative y axis shown in Figure 2.2

α_2 = angle of attack of the interaction blade, positive for right hand rotation about the negative y axis shown in Figure 2.2

β = sideslip angle

Δ = blade–vortex separation distance in the z-direction, defined in Figure 2.2

$\Delta C_{\mathrm{L_{max}}}$ = maximum incremental change in lift coefficient

Δ_y = distance between sensors 2 and 4

Δ_z = distance between sensors 1 and 3

δ = boundary layer thickness

$\delta^\star$ = displacement thickness

Γ = circulation

Γ_0 = root circulation of the vortex generator calculated using lifting line theory

Γ_1 = vortex core circulation defined as $2\pi r_1 V_{\theta 1}$

γ = vortex sheet strength

θ = momentum thickness

θ_i = i-th sensor angle (see Figure 2.4)

$\theta_{\mathrm{eff}_{\mathrm{i}}}$ = effective sensor angle of i-th sensor

Ω_x = mean axial vorticity

Chapter 1

Introduction

1.1 Purpose

Much of the noise generated by a helicopter is a consequence of the interaction of its blades with their own vortex wakes. The objective of the work described here is to improve understanding of the effects which perpendicular blade–vortex interactions (*i.e.* the axis of the vortex is perpendicular to the blade leading edge) have upon those wakes. Changes in the vortex wakes are of interest mainly because of their influence on noise generated by subsequent interactions. Understanding how tip vortices are affected by a perpendicular interaction is therefore critical to the accurate prediction of the helicopter noise, rotor aerodynamics, and blade loading associated with those interactions.

1.2 Some rotor flow details

The flowfield produced in and around a helicopter rotor is very complex and is dependent upon numerous parameters—even in steady flight for a particular helicopter configuration—such as the thrust coefficient, advance ratio, and tip-path-plane angle. Each blade is continuously shedding a vortex sheet, the edge of which quickly rolls up into a concentrated vortex. There are many opportunities for significant interactions between the main rotor vortices and following blades for many low to moderate flight speed conditions. In hover, Landgrebe [1] shows through smoke flow visualization that the tip vortex initially moves radially towards the hub and has only a very small downward movement. It is not until the next blade passes, creating another vortex, that the first vortex is convected downward. In forward flight, experiments have shown that there can be a strong upwash on the upstream part of the rotor disk initially forcing some vortices above the rotor disk (Simons *et al.* [2]). An often used method for determining the wake structure of a helicopter rotor for identification of possible blade–vortex interactions is through the lifting line helicopter trim code CAMRAD (Comprehensive Analytical Model of Rotorcraft Aerodynamics and Dynamics) (Johnson [3]). An example of the results obtained from use of this code are presented

by Preisser *et al.* [4] which predict that multiple interactions can occur (in agreement with their acoustic measurements) and these interactions can be either above or below following blades.

1.3   Importance for BVI noise

Blade–vortex interactions, where the axis of the vortex is nearly parallel to the blade leading edge (Figure 1.1), result in impulsive blade loading which produces impulsive noise referred to as BVI noise (or blade slap).   BVI noise often occurs in the flight regime where the rotorcraft is near the ground with a frequency content in the middle of the audible range which, combined with its impulsive nature, makes it particularly annoying and highly detectable (George [5]). A majority of the research concerning helicopter noise prediction has concentrated on parallel interactions because experimental (see Hoad [6] in conjunction with Egolf and Landgrebe [7]) and theoretical (see Widnall and Wolf [8], Hardin and Lamkin [9]) studies have indicated that the intensity of the impulsive noise increases as the tip vortex becomes more nearly parallel to the blade.

An interaction where the vortex axis is nearly perpendicular to the blade leading edge (Figure 1.1) is an important subset of blade–vortex interactions. Since multiple interactions can occur in the rotor plane, a perpendicular interaction might precede a noise producing oblique or parallel interaction, and the effects of the perpendicular interaction on the vortex must be known to subsequently predict the noise resulting from a later interaction. Many theoretical schemes have shown that the prediction of BVI noise is very sensitive to the input values chosen for the vortex core size, strength, and circulation distribution (see Widnall and Wolf [8], Srinivasan *et al.* [10], Tadghighi *et al.* [11], Lee and Smith [12]) confirming the importance of the effects a previous perpendicular interaction might have on the vortex. Depending upon the advance ratio, perpendicular interactions can occur at a variety of radial locations. If the interaction occurs far inboard of the blade tip, the interaction will be subsonic and the interacting blade might be considered locally two-dimensional (depending on the blade loading). For interactions occurring near the tip, the interaction may be transonic and the downstream interaction with the tip vortex shed from the interacting blade will be important as shown in the case of hover by Landgrebe [1].

1.4   Importance for BWI noise

Perpendicular interactions are of primary importance in the prediction of blade–wake interaction (BWI) noise. This noise source is defined by Brooks *et al.* [13] as the mid-frequency, broadband noise due to blade interaction with turbulent portions of previous blade wakes. They found that BWI noise dominates the mid-frequency range at flight conditions slightly away from where peak BVI noise occur. Devenport *et al.* [14] studied the turbulence and spectral structure of an undisturbed trailing vortex and incorporated the data into the BWI noise prediction scheme of Glegg [15].

Their results showed that the turbulence of an undisturbed vortex is insufficient to account for most of the BWI noise generated. A perpendicular interaction (occurring before a noise producing BWI) may alter the turbulent flowfield significantly, and may therefore be a necessary feature for BWI. To investigate this hypothesis, Wittmer *et al.* [16] examined the effects of a perpendicular interaction by placing a finite span blade in the path of a streamwise trailing vortex and made detailed turbulence measurements from 4 chord lengths upstream to 15 chord lengths downstream of the blade. For small blade–vortex separations they found that the interaction weakens the vortex core, greatly increases its size, and results in a region of turbulence flow of much greater cross-section and intensity than that presented by the original vortex. This new turbulence, incorporated into the BWI noise prediction scheme (see Devenport *et al.* [17]), improved the prediction of BWI noise. Providing detailed descriptions of the fluid dynamics governing the interaction was difficult with this configuration due to the complicating effects of the vortex shed by the finite span blade.

1.5 Importance for tail rotor noise

The flowfield produced after a perpendicular interaction is also important in the prediction of the noise produced by the tail rotor. Leverton [18] notes that vortices originating from the front of the main rotor disc are likely to interact with another blade far inboard before interacting with the tail rotor which may be the source of most tail rotor noise. Similar to the prediction of BVI noise, the vortex core parameters are significant parameters for the prediction of tail rotor noise (Schlinker and Amiet [19], and Leverton [20]).

1.6 Scaling and Mach number considerations

The tips of the rotor blades of a typical helicopter blade experience a local Mach number which is in the transonic regime, while the Mach number of the perpendicular interaction depends on the radial location. The present study does not address the dependence of the interaction upon Mach number. Many studies have attempted to quantify the effects which Mach number and Reynolds number have on the vortex in the far-field; however much of the information is conflicting. For example, a study by Rorke *et al.* [21] suggests that the vortex core parameters (normalized on blade chord) of the rectangular planform wings with rounded tips are independent of both Reynolds number and Mach number. However, the work of Follin [22] shows a significant dependence of velocity profiles through the core of the trailing vortex produced by a rectangular wing with a blunt tip for chord Reynolds numbers between 530,000 and 1,600,000.

1.7   Perpendicular interaction studies by other groups

Most previous work on perpendicular interactions has been concerned with effects on the aerodynamic characteristics of the blade rather than on the vortex itself. Some of this research was aimed at determining whether perpendicular interactions are directly responsible for noise generation while other research was directed towards determining air-loads for performance and structural considerations of helicopters or aircraft with canard configurations.

Ham [23] made pressure measurements on a rotating blade experiencing a perpendicular interaction with an independently generated vortex. Discrepancies were seen between theoretical pressure distributions predicted by the lifting surface theory of Johnson [24] and experimental data for blade–vortex separations of less than one-half of the rotor blade chord. The discrepancies were thought to be the result of local separation occurring due to the vortex-induced loading which lead to a non-rotating, perpendicular interaction study (Ham [25]). For this study, an instrumented two-dimensional airfoil was placed seven chord lengths downstream of the vortex generator with the planforms of the two blades lying in perpendicular planes. The configuration allowed the blade–vortex separation to be continuously varied by oscillating the vortex generator in its spanwise direction. Pressure measurements were made at the 10% chord location on the interaction blade to determine the differential pressure induced by the passing vortex. An empirical relation is derived which suggests that the spanwise pressure gradient supplied by the vortex limits, through flow separation, the amount of loading which can be induced on the blade. For typical helicopter rotor blade–vortex interactions, this limits the maximum incremental lift coefficient to less than 0.3. Peak loading induced by the vortex was found to be independent of the frequency of vortex impingement and proportional to vortex strength (he argues that this peak value is dependent on the two thirds power of the vortex circulation). The angle of attack of the interaction blade did not appear to effect the peak loading except to increase the scatter of the data as the angle of attack was increased. Small deviations in yaw of the interaction blade—producing a non-perpendicular interaction—appeared to have a small, unpredictable effect on the peak loading.

Patel and Hancock [26] investigated the perpendicular interaction of a vortex generated by a rectangular wing (13.6% Clark Y airfoil section) lying in the vertical plane with a wing (same airfoil section and chord) and with a flat plate lying in the horizontal plane: both spanned the entire wind tunnel and were located 10 chords downstream of the vortex generator. Oil and smoke flow visualizations were performed for various heights of the vortex above the wing. Surface pressure measurements were also made. The oil flow visualizations shows that the vortex is displaced spanwise as it passes the wing with a separation distance of 0.5 chords. For a closer separation of 0.2 chords a secondary separation line (indicated by the edge of a three-dimensional herringbone pattern) occurs and the vortex does not appear to be deflected in the spanwise direction. At 0.1 chords it appears that the vortex has caused a local stalling of the airfoil due to the upwash induced

by the vortex. With the vortex impinging on the wing, no flow patterns are observed. Smoke flow visualizations were done at an extremely low Reynolds number of about 10,000. Vortex breakdown is observed to occur further upstream for closer separations. This trend is also seen for the case of the vortex approaching a flat plate at zero angle of attack which leads them to conclude that it is not a pressure gradient effect. They assumed that it is a surface boundary layer effect which causes the instability, but offer no explanation as to how this is propagated upstream ahead of the airfoil. After the broken down vortex passes the wing, they observe a reassembly of the vortex. Pressure measurements are compared with the inviscid theory of Hancock [27] showing only qualitative agreement.

Paterson *et al.* [28] used a configuration similar to Patel and Hancock's where a perpendicular interaction was produced using a fixed 4 in chord NACA 0012 generator and a 9 in chord full-span NACA 0012 blade whose planforms lie in perpendicular planes. The suction side of the interacting airfoil was instrumented with microphones and the vortex passed approximately 0.11 chords below the wing (pressure side passage). The noise creating mechanism was concluded to be "trailing edge noise" due to the interaction between eddies created from localized stall and the airfoil trailing edge. A stall region was found to extend into the spanwise portion of the airfoil where downwash is experienced. This region is characterized as being dominated by low frequency pressure fluctuations.

Phillipe and Armand [29] studied the influence of a trailing vortex on the integrated lift and drag of a rectangular NACA 0012 blade at a Mach number of 0.6 for a constant blade–vortex separation. The vortex was found to reduce the blade lift and increase drag by as much as 40% in the presence of the vortex.

Seath and Wilson [30] studied interactions with a two-dimensional, rectangular NACA 64A015 blade at zero angle of attack at a chord Reynolds number of 417,000. They observed substantial changes in the pressure distribution on the blade in the vicinity of the vortex. A spanwise drift of the vortex was also seen to occur in a direction consistent with the velocity component which would be induced by an image vortex. Flow visualizations were also performed which show three-dimensional separation and reattachment lines induced by the nearby vortex.

Müller [31] studied the "mid vortex" resulting from the interaction of a vortex with a blade, and studied the "double vortex" produced by a blade with a downward pointing winglet. The main thrust of the experiment was to prove the existence of these flow phenomena. The investigation of the "mid vortex" was done with two fixed (non-rotating), blades in perpendicular planes. The disturbing wing created a streamwise vortex which passed to the pressure side of the twisted interaction blade near its tip (a twisted blade was used to approximate the loading of a rotor blade in hover). Flow visualizations and LDV measurements were made in a water tunnel for a chord Reynolds number of 120,000. The LDV measurements clearly showed the "mid vortex" in vorticity contour plots. He also subtracted the contributions from the disturbing vortex and the tip vortex shed from the interaction blade to the velocity field by assuming a Lamb or Oseen-Hammel vortex

core tangential field approximation. The trajectories of the three vortices are also presented for a short distance downstream of the blade trailing edge. Based on his measurements and theoretical considerations, he postulates that the disturbance caused by the vortex on the blade lift distribution causes the local shedding of a "mid vortex" with a strength of one quarter to one third of that of the blade tip vortex.

Kalkhoran *et al.* [32] examined the influence of a trailing vortex on a two-dimensional rectangular NACA 0012 blade at zero incidence for Mach numbers of 0.68–0.9 and blade–vortex separations of 0.1–0.3 chords. Pressure measurements in the flowfield were made at the leading and trailing edges of the interaction blade as well as on the surface of the airfoil. Most of the changes in the pressure distribution on the airfoil were found to be confined to the leading 30% of the chord. These pressure changes were found to be a function of vortex strength and separation distance, but are relatively insensitive to the Reynolds number. The vortex drifted in the spanwise direction as it passed over the blade under the influence of its image in the blade surface. Large unsteady fluctuations in pressure were observed near the vortex center at the blade trailing edge after interaction (this result is most likely caused by buffeting of the vortex due to the nearby separated flow). Two minimum pressure regions were observed in the pressure survey behind the blade for one separation distance, suggesting the possibility of a second vortex. This second vortex may have been formed due to a breakup of the primary vortex or caused by separated flow due to the interaction.

1.8   Flow over the blade

Beginning with the results cited above one can infer some major features of flow over a blade in the presence of a streamwise vortex (Figure 1.2). Velocities associated with the vortex change the local angle of attack (α) of the blade; increasing it outboard of the vortex center and decreasing it inboard. These changes will significantly alter the pressure distribution on the blade and also have a strong influence on the blade boundary layer and subsequent wake. Outboard of the vortex center the thickness of the suction-side boundary layer and the resulting wake are increased by the additional angle of attack. If the vortex is sufficiently strong, or the encounter sufficiently close, a local separation may be induced on the suction surface. Conversely, inboard of the vortex center the boundary layer and wake thickness will be decreased by the presence of the vortex. Since the vortex produces a change in angle of attack along the blade span it also induces the formation of streamwise vorticity in the blade boundary layers which is shed into the wake. Inboard and outboard of the core $\partial \alpha / \partial y$ is positive and thus positive vorticity is shed. In the immediate vicinity of the core negative vorticity is shed. As the vortex passes over the blade it drifts under the influence of its image: inboard for pressure-side passage, outboard for suction-side passage (depicted in Figure 1.2). Downstream of the blade it is expected that the vortex will interact with both the blade wake and the blade tip vortex.

1.9   Objectives and approach

The effects of perpendicular blade–vortex interaction on tip vortex wakes remain largely undocumented. It appears that there are no measurements, other than those performed here at Virginia Tech, of the turbulence structure resulting from a perpendicular interaction, and thus little to base BWI noise predictions on. Wittmer *et al.* [16] studied the effects of a perpendicular interaction in the vicinity of a blade tip revealing much about the overall form and physics of the interaction, however many of the more subtle effects were obscured by the second vortex shed from the blade tip. The present study has therefore concentrated on the effects of perpendicular blade–vortex interactions occurring much further inboard, where the effects of this second tip vortex are negligible. To accomplish this, a fixed blade spanning the entire wind tunnel was placed near the path of a streamwise vortex generated by a fixed blade located upstream.

Considering the lack of information relevant to the BWI noise prediction problem, the study described here had the following objectives:

1. Perform velocity measurements in the turbulent flowfield downstream of an idealized perpendicular interaction with a miniature four-sensor hot-wire probe capable of measuring all three velocity components simultaneously.

2. Adequately document the downstream development of the turbulent flowfield for a single configuration to provide insight into the fluid dynamics governing the interaction.

3. Alter the experimental configuration to determine the effects of blade–vortex separation (sometimes referred to as the miss distance), vortex strength, and blade angle of attack; and assess their relative importance.

4. Develop theoretical models capable of extending the results to configurations beyond the scope of the test matrix.

The following chapter contains descriptions of the major experimental apparatus used in this study, as well as a complete description of the hot-wire technique. The discussion of the experimental data which provides significant information concerning the effects of the interaction is contained in Chapter 3. Chapter 4 outlines some simple theoretical models which were developed to predict some of the flowfield features, and compares the results of the models with the experimental data. A summary of the significant findings of this study is contained in Chapter 5.
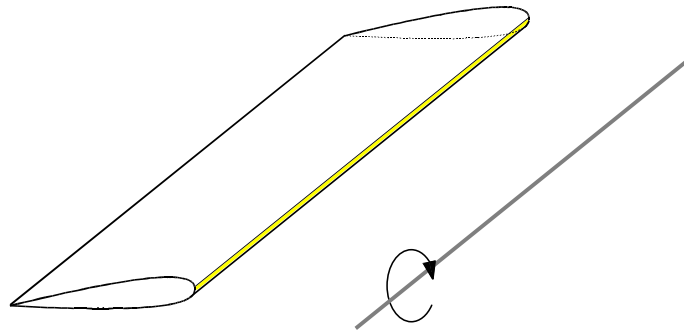
(a) Parallel interaction
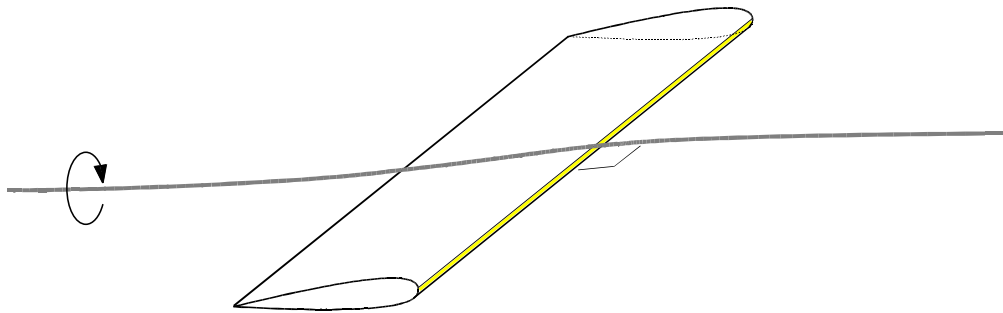
(b) Perpendicular interaction

Figure 1.1: Two types of blade–vortex interactions

Positive vorticity shed by blade
outside core region

Negative vorticity shed by blade
in immediate vicinity of core

Spanwise drift

$\partial\alpha/\partial y > 0$

$\partial\alpha/\partial y < 0$

$\partial\alpha/\partial y > 0$

Vortex decreases local
angle of attack of blade

Increase in suction-side boundary layer thickness
due to local increase in angle of attack and vortex
lifting flow away from blade surface

Vortex increases local
angle of attack of blade

Figure 1.2: Primary features of a perpendicular blade–vortex interaction (suction side passage shown)

9

Chapter 2

Apparatus and instrumentation

The following contains descriptions of the main components of apparatus and instrumentation used to study the flowfield resulting from the perpendicular interaction between a streamwise vortex and an airfoil. A detailed description of the hot-wire technique is also given.

2.1   Wind tunnel

Experiments were performed in the Virginia Tech Stability Wind Tunnel (Figure 2.1).   It is a closed-circuit tunnel powered by a 600 horsepower axial fan. The test section has a square cross section, $1.83\,\mathrm{m} \times 1.83\,\mathrm{m} \times 7.33\,\mathrm{m}$. Flow in the empty test section is closely uniform with a turbulence intensity of less than 0.1%. A slight favorable pressure gradient $(\partial C_p/\partial x = -0.003/\mathrm{m})$ exists along the test section due to boundary layer growth which causes some convergence of the streamlines. Flow angles are small near the middle of the section but increase to about $2°$ near the walls Choi and Simpson [33]).

The free stream dynamic pressure and flow temperature are monitored continuously during operation of the wind tunnel. The former is measured using a pitot-static probe located at the upstream end of the test section connected to a Barocell electronic manometer. The latter is sensed using an Omega thermocouple located within the test section boundary layer—there is no significant temperature gradient across the boundary layer.

2.2   Blades

Untwisted NACA 0012 blades were used: one to generate the vortex and the other to interact with it. Both had a rectangular planform of $0.203\,\mathrm{m}$ chord (c). The vortex generator blade was milled out of a single, $1.22\,\mathrm{m}$ span, piece of aluminum by a numerically controlled milling machine. The interaction blade was assembled from $0.61\,\mathrm{m}$ span half-sections of solid aluminum milled by the same machine which were bolted together to form a $2.44\,\mathrm{m}$ span blade. The thickness distributions

of each blade are accurate to within 0.025 mm.

Effective boundary layer trips were placed on both blades. These consisted of 0.5 mm diameter glass beads glued in a random pattern along the entire span between the 20% and 40% chord locations. The resulting turbulent boundary layers were documented by Devenport *et al.* [14] (see Table 2.1).

The vortex generator blade (hereafter simply referred to as the generator) was mounted vertically as a half-wing at the center of the upper wall of the test section entrance with 0.879 m protruding into the flow (Figure 2.2). The mount allowed the angle of attack of the generator (α_1), and therefore the strength of the shed vortex, to be varied by rotating the generator about its quarter-chord.

The interaction blade was also mounted vertically. It completely spanned the test section $14c$ downstream of the vortex generator. A full-span blade was used to eliminate the complicating effects of an additional blade tip vortex which would have been shed otherwise. To vary the blade–vortex separation distance (Δ) and the strength of the interaction, the z-position and angle of attack of the interaction blade (α_2) could both be varied. To do this, the mount sketched in Figure 2.3 was devised. The upper end of the blade was affixed to a turntable in a cantilever fashion with the center of rotation at the quarter-chord of the blade. The turntable could slide on a pair of rails which allowed it to moved in the z-direction to precise locations. Once the z-position was determined, the turntable was locked in place and the bottom of the wing was bolted to the wind tunnel floor.

The interaction blade was instrumented with 40 static pressure ports and was set at zero angle of attack by equalizing the pressures on both sides. The generator was then placed in the tunnel and set at zero angle of attack by equalizing the pressures on both sides of a removable wing tip holding 48 static pressure ports.

2.3   Hot-wire anemometry

A miniature four-sensor hot-wire probe was used for velocity measurements in the turbulent flowfield downstream of the interaction. Multiple sensor hot-wire probes offer some desirable characteristics for measuring moderately turbulent flows away from walls. They give continuous, low-noise signals required for the measurement of low turbulence levels and velocity spectra; and can provide the type of statistical turbulence information usually used by turbulence modellers. X-wire probes are relatively easy to operate but produce large uncertainties in the complete Reynolds stress tensor field because all three velocity components cannot be measured simultaneously. Triple wire probes are capable of simultaneous three-component measurements, but their usually large measurement volume and sensor configuration make them sensitive to velocity gradient errors, particularly those associated with streamwise vorticity (Devenport *et al.* [14]). Four-sensor probes consisting of two

orthogonal X-wire arrays (Figure 2.4)—normally associated with vorticity measurements (Kovasznay [34])—are capable of simultaneous three-component velocity measurements from a relatively compact measurement volume and appear to overcome some of the gradient error problems associated with triple wire probes.

Initially it might appear that there are several difficulties associated with the use of a four-sensor probe for velocity measurements. Standard hot-wire angle response equations derived via Jorgensen's method (Jorgensen [35]) yield a non-linear set of equations which are inaccurate at large flow angles due to effects like prong interference. Most direct calibration methods improve accuracy but usually require sophisticated interpolation schemes. The calibration technique for the four-sensor probe described here overcomes these limitations, and velocity gradient errors suffered by the probe are analyzed. The complete hot-wire system is capable of rapid and accurate, three-component, velocity, turbulence, and spectral measurements.

2.3.1 The four-sensor probes and measurement system

Probes

Probes were manufactured by Auspex Corporation (type AVOP-4-100). Eight stainless steel or nickel plated tungsten tapered prongs (75 mm in diameter at their tips) position the wires some 40 mm upstream of the main part of the probe (Figure 2.5). The sensors are etched tungsten wire of 5 mm diameter with an approximate length of 0.8 mm giving a length to diameter ratio of 160. The measurement volume of the probes are approximately $0.5\,\text{mm}^3$.

The sensors are arranged as two orthogonal X-wire arrays with each wire inclined at a nominal $45°$ angle to the probe axis. Figure 2.4 defines the coordinate system and sensor numbering convention. The velocity components U, V, and W are directed along the x, y, and z axes respectively. One X-wire array is formed by sensors 1 and 3 (both parallel to the x-y plane), the other X-wire array is formed by sensors 2 and 4 (both parallel to the x-z plane). The subscript i will be used to denote quantities associated with the i-th sensor where $i = 1\ldots4$. Angles (θ_i) associated with the sensors are acute angles measured from the x-axis.

Measurement system

A block diagram of the measurement system is shown in Figure 2.6. Hot-wire sensors are operated separately using a Dantec 56C17/56C01 constant temperature anemometer unit. Anemometer bridges are optimized to give a frequency response greater than 25 kHz. The output voltages from the anemometer bridges are recorded by an IBM AT compatible computer using an Analogic 12 bit HSDAS-12 A/D converter which contains four separate converters. Hot-wire signals are buffered by four $\times10$ buck-and-gain amplifiers. The amplifiers contain calibrated RC-filters which limit their frequency response to 50 kHz, providing high frequency noise attenuation. The buck-and-gain is used so that the anemometer voltage outputs span the full range of the A/D converter over

the velocity range of the measurement. Voltage outputs from a digital thermometer and pressure transducer are also sampled by the A/D converter. The digitized raw voltage data is stored on optical disk. An 18-8 Laboratories PL2510 array processor is used to calculate velocity estimates "on line". Calibration procedures outside of the wind tunnel are accomplished by placing the probe in the uniform potential jet of a TSI model 1125 calibrator. The probe can be manually pitched and yawed to a known angle in this jet with use of two rotary stages.

2.3.2 Calibration techniques

Outside the wind tunnel

The majority of the calibration procedures are performed outside of the wind tunnel. The purpose of these procedures are to determine the effective sensor angles and establish an angle calibration.

Effective sensor angles

Although the geometric sensor angles can be measured fairly easily, the determination of so called "effective" sensor angles can simplify the calibration procedure. Considering the i-th wire, the probe is pitched (for $i = 1$ and 3) or yawed (for $i = 2$ and 4) in the calibrator jet to determine the angle where maximum cooling (highest output voltage) occurs—approximately the geometric sensor angle. At this angle, a Kings law calibration is performed to relate the output voltage E_i of the sensor to the cooling velocity U_c which it experiences (Equation 2.1).

$$E_i^2 = A_i + B_i U_c^n \tag{2.1}$$

An exponent n of 0.45 is used and the constants A_i and B_i are determined by linear regression from 10 or more calibration points (jet speeds U_c). Calibrations with curve fit errors of less than 0.5% at the calibration points are not difficult to obtain. A measurement is then taken with the probe axis parallel to the flow at a speed approximately equal to the wind tunnel free-stream speed U_∞. Using the Kings law calibration, effective cooling velocities U_{eff_i} are inferred. The effective sensor angles θ_{eff_i} can then be determined from

$$\cos \theta_{\mathrm{eff}_i} = \frac{U_{\mathrm{eff}_i}}{U_\infty}. \tag{2.2}$$

Angle response

To calibrate the angle response, a method similar to that of Mathioudakis and Breugelmans [36] is used. They developed this method to greatly extend the useful range of flow angles which can be accurately measured by a triple wire probe. In this adaptation of their method, the four-sensor probe is placed in the uniform jet of the calibrator at a known flow direction and a velocity equal to the wind-tunnel free-stream velocity. The cooling velocities are then measured as the probe is

pitched and yawed over all likely angle combinations; usually $\pm 45°$ in increments of $5°$ or less.

Following Jorgensen [35] we obtain expressions for the velocity estimates U_e, V_e, W_e by writing the effective cooling velocity of each sensor in terms of: the velocity components it experiences U_i, V_i, W_i; the effective sensor angle; and a pitch sensitivity h_i (Equations 2.3–2.6).

$$U_{\text{eff}_1}^2 = (U_1 \sin \theta_{\text{eff}_1} + V_1 \cos \theta_{\text{eff}_1})^2 + (h_1 W_1)^2 \tag{2.3}$$

$$U_{\text{eff}_2}^2 = (U_2 \sin \theta_{\text{eff}_2} + W_2 \cos \theta_{\text{eff}_2})^2 + (h_2 V_2)^2 \tag{2.4}$$

$$U_{\text{eff}_3}^2 = (U_3 \sin \theta_{\text{eff}_3} - V_3 \cos \theta_{\text{eff}_3})^2 + (h_3 W_3)^2 \tag{2.5}$$

$$U_{\text{eff}_4}^2 = (U_4 \sin \theta_{\text{eff}_4} - W_4 \cos \theta_{\text{eff}_4})^2 + (h_4 V_4)^2 \tag{2.6}$$

Note that an axial sensitivity is not included because it has been our experience that the effective wire angles incorporate this factor. Assuming for now that the measurement volume is infinitely small ($U_i = U_e$, $V_i = V_e$ etc.), V_e^2/U_e^2 and W_e^2/U_e^2 terms are small compared to 1 or $U_e V_e/U_e^2$, and $\sqrt{1 + x}$ may be approximated as $1 + \frac{1}{2}x$ for small x, this set of equations may be linearized and inverted to give explicit equations for the velocity component estimates *i.e.*

$$V_e = \frac{C_1\sqrt{C_3}U_{\text{eff}_3} - C_3\sqrt{C_1}U_{\text{eff}_1}}{C_1 D_3 - C_3 D_1} \tag{2.7}$$

$$W_e = \frac{C_2\sqrt{C_4}U_{\text{eff}_4} - C_4\sqrt{C_2}U_{\text{eff}_2}}{C_2 D_4 - C_4 D_2} \tag{2.8}$$

$$U_e = \frac{1}{2} \left(\frac{U_{\text{eff}_1}}{\sqrt{C_1}} - \frac{D_1}{C_1}V_e + \frac{U_{\text{eff}_2}}{\sqrt{C_2}} - \frac{D_2}{C_2}W_e \right) \tag{2.9}$$

where $C_i = \sin^2 \theta_{\text{eff}_i}$ and $D_i = \sin \theta_{\text{eff}_i} \cos \theta_{\text{eff}_i}$. Equation 2.9 is simply an average of the two U estimates obtained from the X-wire arrays formed by sensors 1 and 3, and sensors 2 and 4. As will be shown later, this averaging minimizes the contamination effect which axial vorticity has on the U-component.

At each pitch and yaw combination in the angle calibration, velocity component estimates are compared with the actual velocity components U, V, W inferred from the known flow angles. Specifically, the error fractions $(V - V_e)/Q_e$, $(W - W_e)/Q_e$, $(Q - Q_e)/Q_e$ are formed where $Q_e = \sqrt{U_e^2 + V_e^2 + W_e^2}$ and $Q = \sqrt{U^2 + V^2 + W^2}$. By interpolating the calibration data these fractions are then tabulated as functions of V_e/Q_e and W_e/Q_e. The tables are then used to correct instantaneous estimates of V_e, W_e, and Q_e (and therefore U_e) obtained during a measurement.

However, interpolation of the error fraction data into tabular form is not straight forward because of the limited acceptance cone of the probe (the region within which a single valued relationship between the cooling velocities and velocity components can be established). Non-

uniqueness occurs because a point outside the acceptance cone can have the same estimated velocity ratios $(V_e/Q_e, W_e/Q_e)$ as a point inside, confusing the interpolator. An important part of the table generation is therefore the determination of the acceptance cone. Figure 2.7 shows an example of the folded surface formed if, for example, the Q_e error fraction is plotted vs. V_e/Q_e and W_e/Q_e including data both inside and outside the acceptance cone. The folds lie outside the acceptance cone. By using vector arithmetic to determine the direction of the normal to the surface, these folds can be identified and then eliminated from the interpolation. For example, consider two non-parallel vectors $\vec{p}$ and $\vec{q}$ such as the ones shown in Figure 2.8 $e.g.$

$$\vec{p} = \frac{\partial(V_e/Q_e)}{\partial V}\hat{i} + \frac{\partial(W_e/Q_e)}{\partial V}\hat{j} \tag{2.10}$$

$$\vec{q} = \frac{\partial(V_e/Q_e)}{\partial W}\hat{i} + \frac{\partial(W_e/Q_e)}{\partial W}\hat{j}. \tag{2.11}$$

Using these vectors, points lie outside the acceptance cone if $\|\vec{p} \times \vec{q}\| < 0$.

Error fraction contours plotted as a function of $(V/Q, W/Q)$ are shown in Figure 2.9 for flow angles within the acceptance cone of the probe. These plots show that sophisticated interpolation is not required because the corrections vary slowly over most of the acceptance cone—an advantage of this method over others in which look up tables are used ($e.g.$ Browne $et\ al.$ [37], Leuptow $et\ al.$ [38], Döbbeling $et\ al.$ [39]). The acceptance cone has a roughly diamond shaped limit (marked by the dashed line) indicating that larger flow angles can be measured if the flow direction corresponds to a near pure pitch or yaw (refer to Figure 2.4 for coordinate system). The maximum flow angle which can be measured in pure pitch or yaw is approximately $40°$. This is the expected limit since angles greater than the nominal $45°$ sensor angle create reverse flow on a sensor. For flow angles which are not pure pitch or yaw the limits are less as a result of prong interference effects. However, regardless of the roll orientation of the probe, flow angles less than $30°$, $i.e.$ $\sqrt{V^2 + W^2}/Q < \sin 30°$, can always be measured. Contours of the error fraction $(V - V_e)/Q_e$ shown in Figure 2.9a indicate that the V-component of velocity is estimated well if the probe is in pure yaw and likewise, contours of $(W - W_e)/Q_e$ (Figure 2.9b) indicate that the W-component of velocity is estimated well if the probe is in pure pitch. The W_e error fraction contours have an appearance similar to the V_e error fraction contours—as expected due to the symmetry of the sensors—however the errors increase more rapidly. The difference is likely due to differing prong interference effects and a non-ideal sensor geometry (the sensors do not lie precisely in the x-y and y-z planes). The Q_e error fraction (Figure 2.9c) shows that Q is consistently overpredicted by the linearized equations, but the corrections vary even more slowly than the V_e and W_e error fractions.

Inside the wind tunnel

Once the angle calibration has been completed, only velocity calibrations need to be performed inside the wind tunnel. All four sensors are calibrated simultaneously via King's law with the probe approximately parallel to the wind tunnel free-stream using Equation 2.12.

$$E_i^2 = A_i + B_i U_{\text{eff}}^n \tag{2.12}$$

However when the probe is placed at the selected calibration location in the wind tunnel, it most likely will not have the same alignment to the free-stream flow as to the calibration jet. Therefore, the effective cooling velocities here are not the same as those used to determine the effective sensor angles. To measure this difference in flow angle, a calibrated seven hole yaw probe is used. The effect this difference in the angle of attack (α) and sideslip angle (β) of the probe has on the effective cooling velocities is well estimated by the following Jorgensen [35] style equations if α and β are small:

$$U_{\text{eff}_1}^2 = (U \sin \theta_{\text{eff}_1} + V \cos \theta_{\text{eff}_1})^2 + (h_1 W)^2 \tag{2.13}$$

$$U_{\text{eff}_2}^2 = (U \sin \theta_{\text{eff}_2} + W \cos \theta_{\text{eff}_2})^2 + (h_2 V)^2 \tag{2.14}$$

$$U_{\text{eff}_3}^2 = (U \sin \theta_{\text{eff}_3} - V \cos \theta_{\text{eff}_3})^2 + (h_3 W)^2 \tag{2.15}$$

$$U_{\text{eff}_4}^2 = (U \sin \theta_{\text{eff}_4} - W \cos \theta_{\text{eff}_4})^2 + (h_4 V)^2; \tag{2.16}$$

where $U = U_\infty \cos \beta \cos \alpha$, $V = U_\infty \sin \beta$, and $W = U_\infty \cos \beta \sin \alpha$. The constants A_i and B_i of Equation 2.12 are determined with the use of Equations 2.13–2.16 from 10 or more calibration points. The reference velocity U_∞ is the free-stream velocity measured by the wind tunnel's pitot-static probe.

Velocity calibrations were easily performed whenever the velocity measured by the hot-wire probe at the calibration point differed significantly from the free-stream velocity measured by the reference pitot-static probe; typically once every two hours. Re-calibrations account for fouling (which will change the cooling rate) and changes in the electrical characteristics of the sensor, and also limit the amount of temperature compensation required.

Temperature corrections

The temperature is continuously monitored and recorded during all measurements. Ambient temperature drift is corrected using the method of Bearman [40]. This method provides a means of predicting the bridge output voltage E_c which would have existed if the measurement occurred at a constant temperature T_c. The correction to the measured bridge output voltage E_m taken at

temperature T_m is shown in Equation 2.17 for a known overheat ratio γ.

$$E_\mathrm{c} = E_\mathrm{m}\sqrt{\frac{\gamma - 1}{\gamma - T_\mathrm{m}/T_\mathrm{c}}} \tag{2.17}$$

2.3.3   Useage considerations

Probe geometry effects

A major feature of this direct angle calibration method is that accurate measurements can be made for non-ideal probe geometries. For example, a probe whose sensors do not lie precisely in the x-y and y-z planes (see Figure 2.4) can be calibrated just as easily. The angle calibration has also been found to be insensitive to the sensor properties if the probe tip geometry remains unaltered—meaning that it only needs to be performed once—as indicated by re-calibration of the angle response of a probe after many hours of measurements and broken sensors were repaired. This is not surprising since the velocity calibrations performed inside the wind tunnel account for varying sensor properties and is a definite advantage of this calibration method because the angle calibration is a slow, time consuming procedure.

Reynolds number effects

One possible drawback of this calibration method is the implicit assumption that the angle calibration is independent of velocity. However for the velocity ranges encountered in many turbulent flows away from walls, this assumption appears to have only a small effect as shown in Figure 2.10. For Reynolds numbers Re_{L_w} (based on an average sensor length L_w of 0.77 mm for this probe) between 1,000 and 3,000 (velocities between 19 and 57 m/s), the error fractions are plotted for angle calibration points $(V/Q, W/Q)$ of $(0, 0.342)$ and $(0.342, 0.321)$. The maximum slope of each error curve is less than $1.5\%/1{,}000\,Re_{L_\mathrm{w}}$ indicating negligible dependence of the error fractions (less than $\pm 0.5\%$) for $\pm 15\%$ velocity variations centered at a Re_{L_w} of 2,000 (Re_c of 530,000).

Velocity gradient effects

Velocity gradients are of interest to the four-sensor probe analysis because the finite measurement volume of the probe results in each sensor experiencing a different flow—in fact, the flow also varies along the length of each sensor. Vukoslavĉević and Wallace [41] investigated the effects of cross-stream velocity and velocity gradients on streamwise vorticity measurements in a turbulent boundary layer. They determined that streamwise vorticity can be accurately measured with this type of probe in flows where the axial velocity gradients $\partial U/\partial y$ and $\partial U/\partial z$ can be neglected with respect to the cross-flow velocity gradients $\partial V/\partial z$ and $\partial W/\partial y$—rarely the case for practical boundary layer flows. For example, they found errors as large as 30% in instantaneous streamwise vorticity measurements and as much as 80% in the instantaneous cross-stream velocity components v and w. For all measured flow variables, they found that reducing the wire spacing reduced these

errors. These limitations are of little consequence if the probe is used for three-component velocity measurements (not for instantaneous streamwise vorticity measurements) in wake flows with weak axial velocity gradients.

The following is an analysis similar to that of Vukoslavĉević and Wallace [41], and Cutler and Bradshaw [42], which was adapted to determine the significance of errors produced by velocity gradients for this particular four-sensor probe. Specifically, the errors resulting from use of equations 2.7–2.9 where the velocity field is assumed constant across the measurement volume will be analyzed. This analysis therefore does not consider the look-up tables.

If the velocity field about a point located at the center of the measurement volume (U, V, W) is expanded as a first order Taylor series, the velocity field experienced by the center of the i-th sensor (U_i, V_i, W_i) is:

$$U_1 = U - \Delta_z \frac{\partial U}{\partial z}, \; V_1 = V - \Delta_z \frac{\partial V}{\partial z}, \; W_1 = W - \Delta_z \frac{\partial W}{\partial z} \tag{2.18}$$

$$U_2 = U - \Delta_y \frac{\partial U}{\partial y}, \; V_2 = V - \Delta_y \frac{\partial V}{\partial y}, \; W_2 = W - \Delta_y \frac{\partial W}{\partial y} \tag{2.19}$$

$$U_3 = U + \Delta_z \frac{\partial U}{\partial z}, \; V_3 = V + \Delta_z \frac{\partial V}{\partial z}, \; W_3 = W + \Delta_z \frac{\partial W}{\partial z} \tag{2.20}$$

$$U_4 = U + \Delta_y \frac{\partial U}{\partial y}, \; V_4 = V + \Delta_y \frac{\partial V}{\partial y}, \; W_4 = W + \Delta_y \frac{\partial W}{\partial y}; \tag{2.21}$$

where $2\Delta_y$ is the distance between sensors 2 and 4, and $2\Delta_z$ is between sensors 1 and 3. Substituting equations 2.18–2.21 into 2.3–2.6 and using the same assumptions used to obtain equations 2.7–2.9, we find the errors due to the velocity gradients are:

$$U - U_{\mathrm{e}} = \frac{\Delta_z \frac{\partial V}{\partial z}[\cos(\theta_1 - \theta_3) + \cos(\theta_1 + \theta_3)] - \Delta_z \frac{\partial U}{\partial z}\sin(\theta_3 - \theta_1)}{2\sin(\theta_1 + \theta_3)}$$

$$+ \frac{\Delta_y \frac{\partial W}{\partial y}[\cos(\theta_2 - \theta_4) + \cos(\theta_2 + \theta_4)] - \Delta_y \frac{\partial U}{\partial y}\sin(\theta_4 - \theta_2)}{2\sin(\theta_2 + \theta_4)} \tag{2.22}$$

$$V - V_{\mathrm{e}} = \frac{\Delta_z \frac{\partial U}{\partial z}[\cos(\theta_1 - \theta_3) - \cos(\theta_1 + \theta_3)] + \Delta_z \frac{\partial V}{\partial z}\sin(\theta_3 - \theta_1)}{\sin(\theta_1 + \theta_3)} \tag{2.23}$$

$$W - W_{\mathrm{e}} = \frac{\Delta_y \frac{\partial U}{\partial y}[\cos(\theta_2 - \theta_4) - \cos(\theta_2 + \theta_4)] + \Delta_y \frac{\partial W}{\partial y}\sin(\theta_4 - \theta_2)}{\sin(\theta_2 + \theta_4)}. \tag{2.24}$$

For simplicity, consider the case of an ideal probe with $\theta_{\mathrm{eff}_i} = 45°$, $\Delta_y = \Delta_z$. Equations 2.22–2.24

reduce to:

$$U - U_{\mathrm{e}} = -\frac{1}{2}\Delta_y \left(\frac{\partial V}{\partial z} + \frac{\partial W}{\partial y} \right) \tag{2.25}$$

$$V - V_{\mathrm{e}} = -\Delta_y \frac{\partial U}{\partial z} \tag{2.26}$$

$$W - W_{\mathrm{e}} = -\Delta_y \frac{\partial U}{\partial y}. \tag{2.27}$$

These equations illustrate the basic relationships between the velocity errors and the local velocity gradients and are similar to those derived by Cutler and Bradshaw [42]. The averaging of the two U estimates results in the streamwise velocity gradient error (Equation 2.25) being proportional streamwise strain rate for the case of an ideal probe intead of the streamwise vorticity. This averaging is essential for trailing vortex measurements where $\partial V_\theta / \partial r$ is very large at the core center (r is the radial distance from the core center and V_θ is the circumferential velocity component). Since the axisymmetry of the flow results in $\partial V/\partial z = -\partial W/\partial y$ at the core center (the location of maximum axial vorticity), the U-component gradient error is zero for the case of an ideal probe.

2.3.4 Sample measurement data

A quantitative analysis of the relative importance of the full angle calibration and velocity gradient effects is contained in Appendix A. The full angle calibration is shown to be very important, especially for the accurate measurement of turbulence quantities. The errors in the mean velocities produced by velocity gradients are estimated to be very small, indicating that this type of probe is suitable for the measurements contained within this study.

2.4 Traversing mechanism

Probe positioning inside the wind tunnel was aided by a computer controlled two-axis (y and z) traverse which is accurate to approximately 0.25 mm. The hot-wire probe was sting mounted parallel to the free stream flow using 12.7 mm diameter steel tubing. The tip of the probe was placed 0.5 m upstream of the 19 mm diameter horizontal traverse support (see Figure 2.11)—the maximum distance at which no vibrations were visible.

2.5 Helium bubble flow visualization

To determine the location of the vortex core relative to the interaction blade, flow visualizations were performed by seeding the flow with helium-filled soap bubbles produced by a Sage Action Inc. model 5 generator. Being lighter than air, the bubbles centrifuge into the vortex core, marking

it clearly. The bubbles were introduced through a streamlined strut located in the wind tunnel's contraction and illuminated using a Varian arc lamp (model p150s-7) located at the end of the test section. Varying either the strut location or the arc lamp position produced no visible effects on the vortex and its path. It was therefore assumed that they produced no significant disturbances to the flowfield. Both the strut and arc lamp were removed for all velocity measurements.

	Pressure side	Suction side
$\delta/c \times 100$	4.35	6.22
$\delta^\star/c \times 100$	0.99	1.61
$\theta/c \times 100$	0.58	0.87
Re_θ	2900	4355

Table 2.1: Boundary layer properties for the generator at 5° estimated from near-wake profile measurements at $x/c = 1.05$, $y/c = 1.2$. Data from Devenport *et al.* [14].
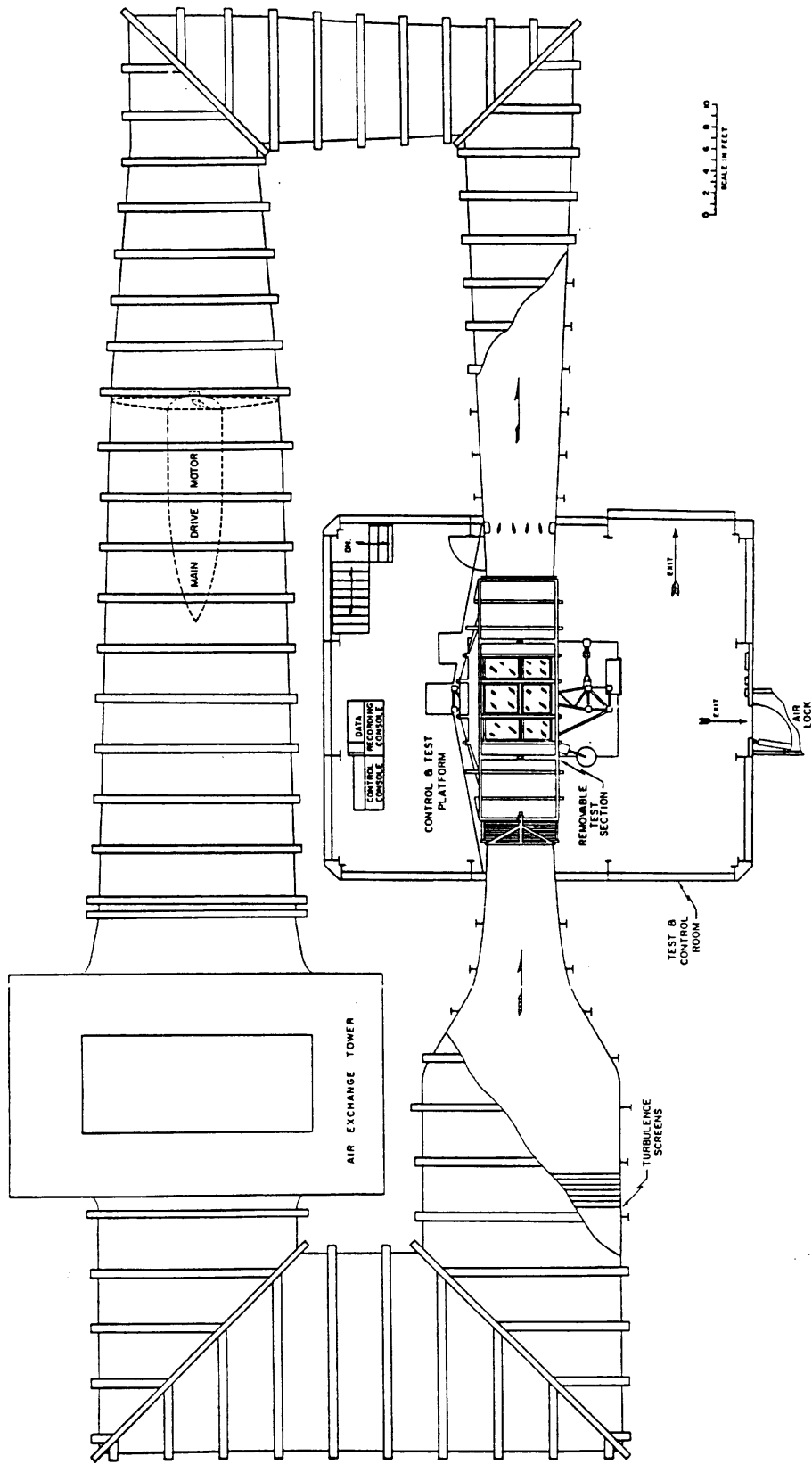
Figure 2.1: Virginia Tech Stability Wind Tunnel
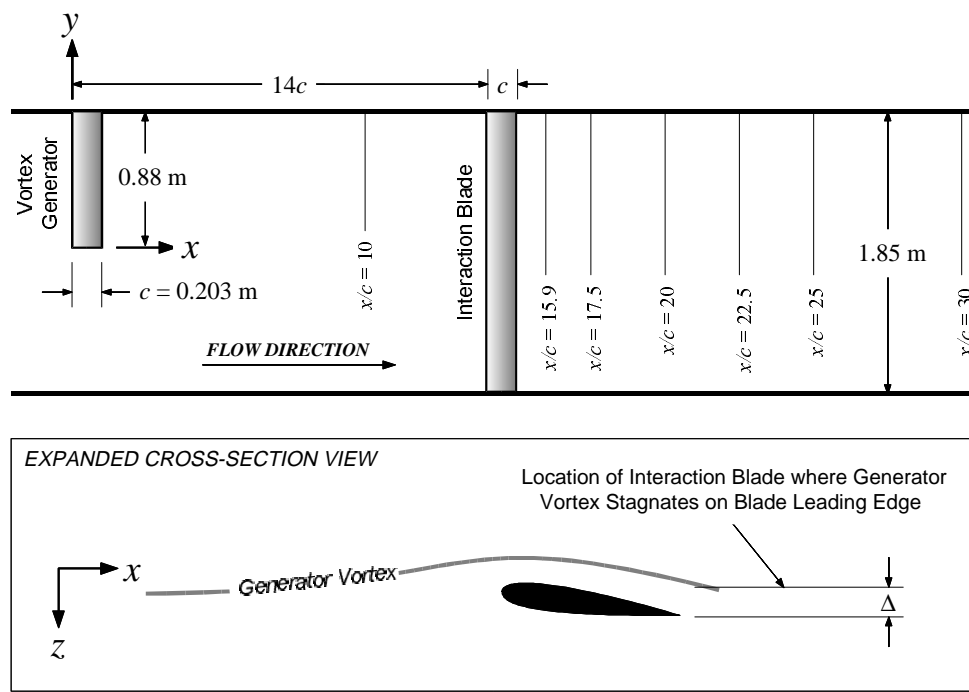
Figure 2.2: Wind tunnel schematic and coordinate system
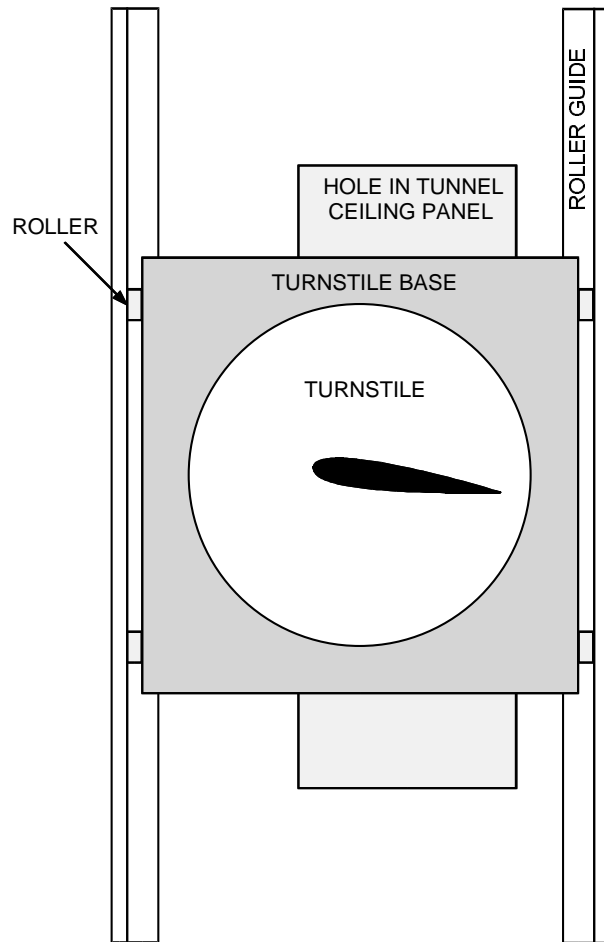
Figure 2.3: Sketch of mount used to position the interaction blade
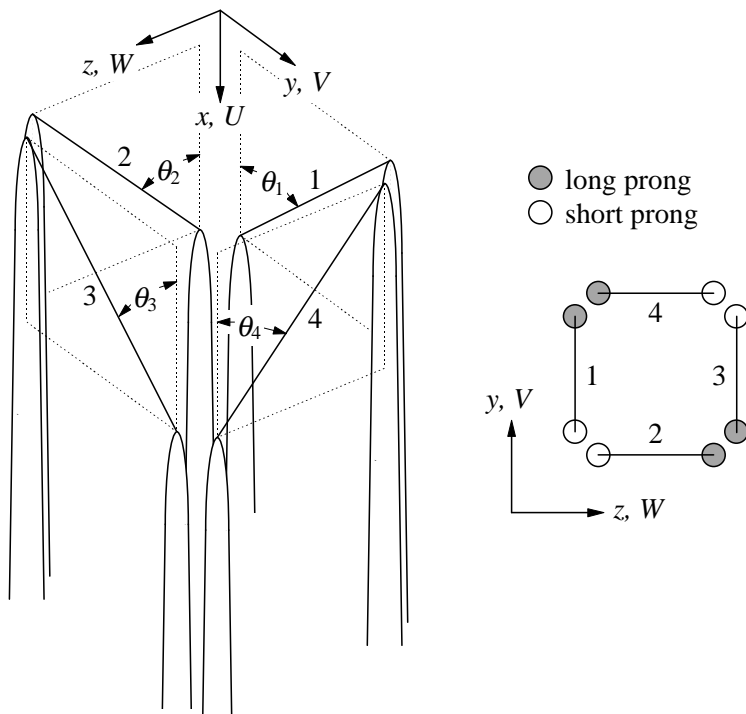
Figure 2.4: Four-sensor probe prong geometry

Ceramic Tubes
(length ~ 10mm)

Delrin Block, (length = 50mm,
7.9mm square cross-section)

DUPONT BergCon
Type Connector

Probe Prongs
(length ~ 40mm)

Stainless Steel Casing
(length = 63mm, diam. = 4.3mm)

Electrical Leads
(length ~ 50mm)
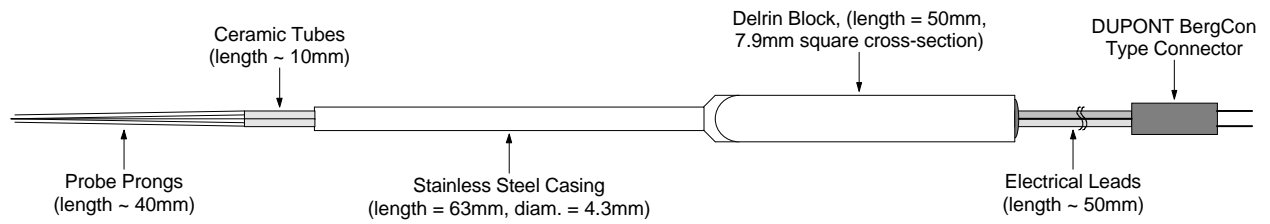
Figure 2.5: Auspex Corporation four-sensor probe (type AVOP-4-100) construction
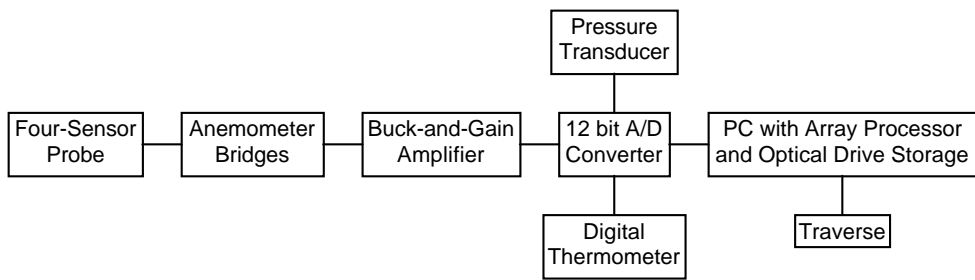
Figure 2.6: Measurement system block diagram
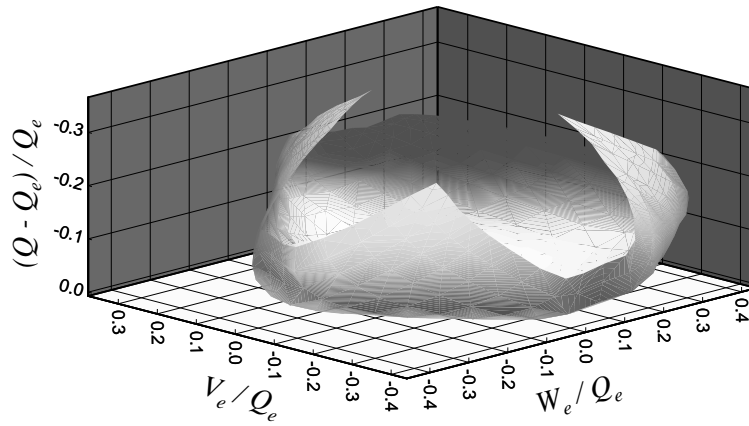
Figure 2.7: Surface formed by Q_e error fraction for pitch and yaw combinations less than $\pm 45°$
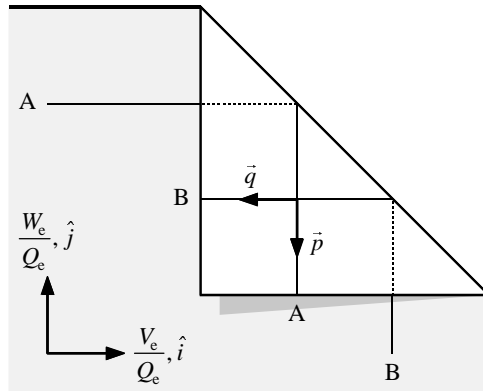
Figure 2.8: Simplified diagram illustrating vectors used to remove points outside acceptance cone
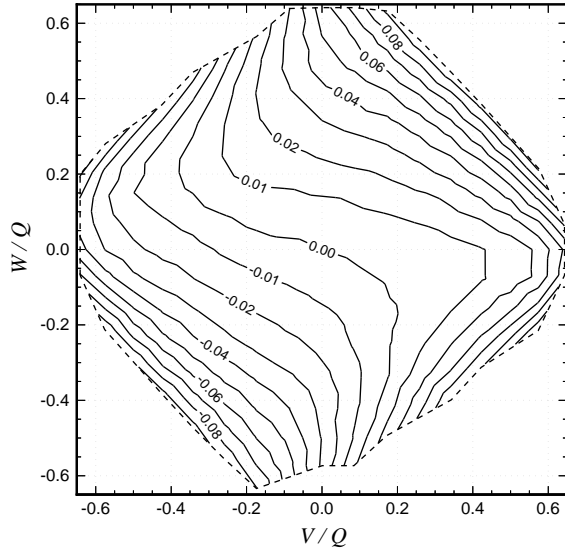
(a) $(V - V_\mathrm{e})/Q_\mathrm{e}$
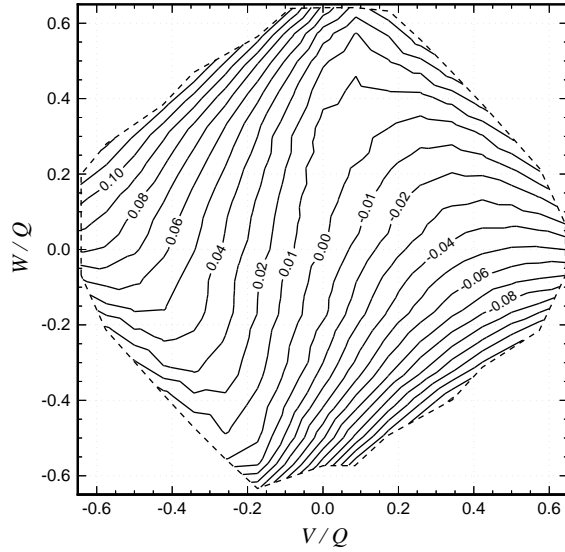
(b) $(W - W_\mathrm{e})/Q_\mathrm{e}$
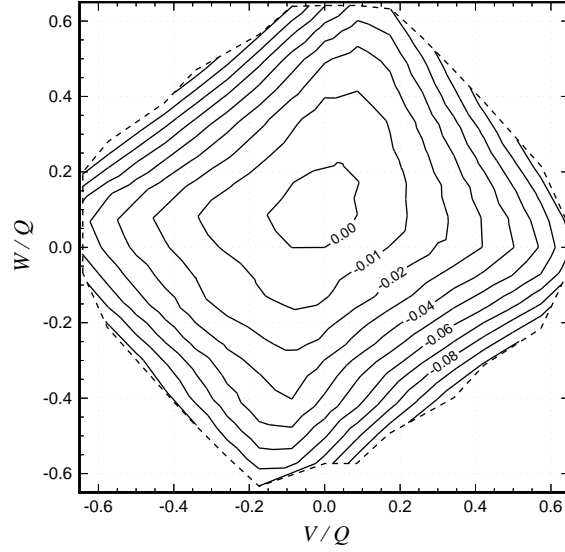
(c) $(Q - Q_\mathrm{e})/Q_\mathrm{e}$

Figure 2.9: Error fraction contours throughout acceptance cone of probe
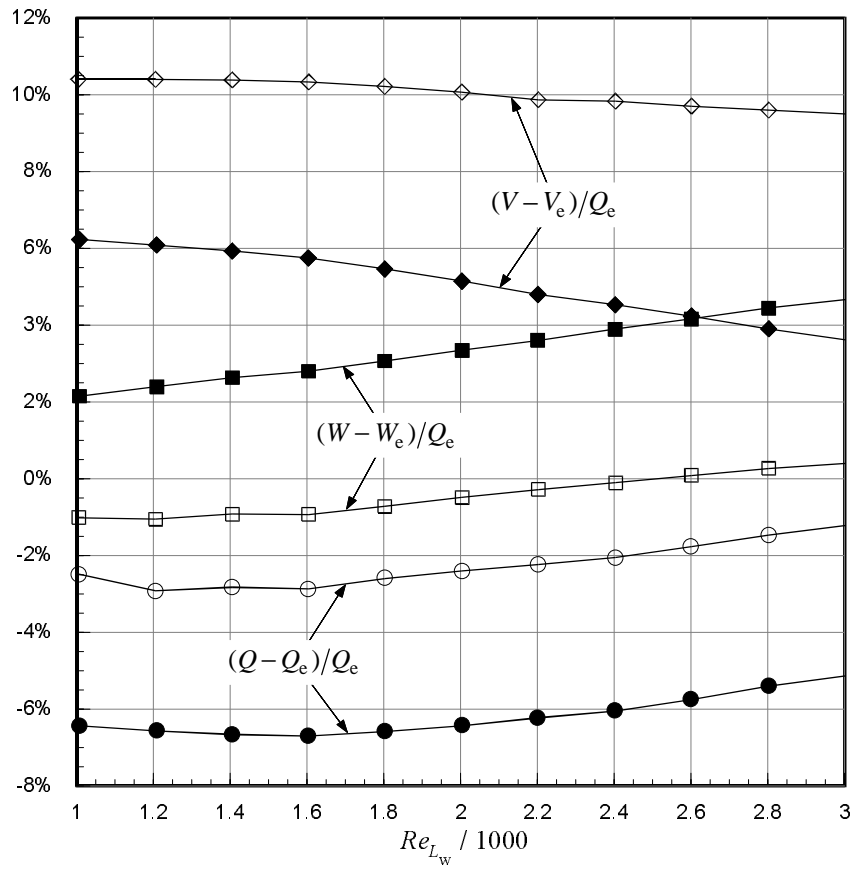
Figure 2.10: Effects of Reynolds number on error fractions for two sample calibration points. Open symbols are for $(V/Q, W/Q) = (0, 0.342)$, solid symbols for $(-0.342, 0.321)$.
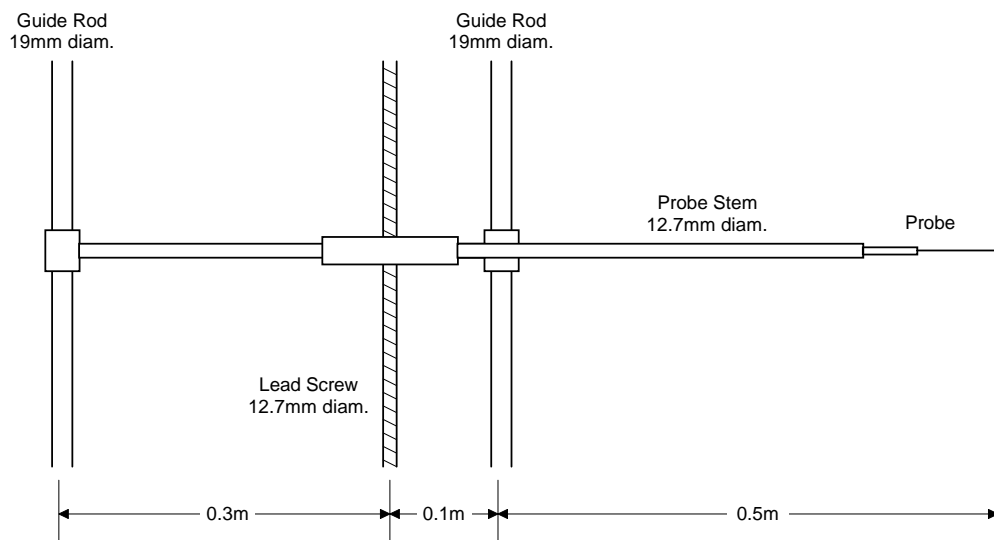
Figure 2.11: Sketch of the wind tunnel horizontal traverse and probe mount

Chapter 3

Results and discussion

3.1 Data sampling and presentation

3.1.1 Coordinate system

Measurements will be presented in the wind-tunnel aligned coordinate system (x, y, z) shown in figure 2.2. Coordinate x is measured downstream from the generator leading edge, y inboard from its tip, and z from the quarter chord line so as to complete the right-handed system. The mean velocity components U, V, W; and fluctuating components u, v, w; are defined in the x, y, z directions respectively. In this system, the leading edge of the interaction blade is at $x/c = 14$. All measurements are presented in non-dimensional form. Most are normalized on the free-stream velocity (U_∞) indicated by the wind tunnel pitot-static probe, and blade chord. All measurements were performed at a chord Reynolds number (Re_c) of 530,000, corresponding to a free-stream velocity of about $40\,\mathrm{m/s}$.

A blade–vortex separation (Δ) of zero corresponds to the blade z position where the streamline marking the vortex center stagnates upon the interaction blade's leading edge. Δ is negative when the vortex passes on the pressure side of the interaction blade, and positive when it passes on the suction side. Zero Δ configurations were determined using helium bubble flow visualizations at $Re_c =$ 260,000.

Some velocity profile measurements are presented in terms of core-aligned mean (V_x, V_θ, V_r) and fluctuating (v_x, v_θ, v_r) velocity components. This system is obtained by rotating the wind-tunnel fixed system twice (a rotation about its y-axis, and then a rotation about the resulting z-axis) so that local mean velocity of the vortex core center is defined solely by V_x. All profiles were measured along lines parallel to the z-axis. Distances in these profiles are expressed in terms of the coordinate r representing distance from the core center (r is considered negative if the location is in the negative z-direction from the core center).

3.1.2   Measurement conditions

The present study attempts to document many aspects of blade–vortex interactions. Experiments were performed for many combinations of blade–vortex separation, streamwise position, blade angle of attack, and vortex strength (controlled by generator angle of attack). A full list of these locations and conditions is given in Table 3.1.

3.1.3   Sampling information

The hot-wire signals were digitized at two different sampling frequencies, depending upon the data deduction to be performed. For statistical velocity measurements, a sampling frequency of 1.5 kHz was used. At this frequency, at least 20 blocks of 1024 samples were recorded over a time period of about 30 seconds. To evaluate the frequency content of turbulence fluctuations at the vortex core center, a sampling frequency of 50kHz was used to record 100 blocks of 4096 samples over a time period of approximately two minutes. Velocity autospectra was obtained from these measurements via FFT using non-overlapping Hanning windows of 2048 samples, resulting in 200 averages.

3.1.4   Contouring

Much of the data measured in the y-z plane is presented as color flooded contour plots. These contours were determined using Amtec Engineering's Tecplot™ computer program.

3.2   The undisturbed vortex

Devenport *et al.* [43] made velocity measurements to document the undisturbed structure and development of the tip vortex shed by the generator as functions of downstream distance and generator angle of attack. Measurement locations and conditions, and vortex core parameters for these cases are summarized in Table 3.2.   These data have been already analyzed and discussed by Devenport *et al.* [43], so only details relevant to the blade–vortex interaction problem are discussed here. Particular emphasis here is placed on measurements made at $x/c = 10$ since these characterize the inflow to the interaction blade (mounted at $x/c = 14$) for many of the perpendicular BVI tests of this study. Uncertainty estimates for the velocity measurements of Devenport *et al.* [43] and those presented in this study are given in Table 3.3.

3.2.1   Streamwise development

To document the streamwise development of the undisturbed vortex, Devenport *et al.* [43] made measurements at $x/c = 5$, 10, 15, 20, 25, and 30 with the generator at $5°$ angle of attack. Figure 3.1 illustrates the overall form of the vortex in terms of contours of axial normal turbulent stress ($\overline{u^2}/U_\infty^2$) measured at these six streamwise locations.   More detailed views of the flow

structure surrounding the vortex core region at $x/c = 10$ are given by the contours of: mean axial velocity deficit, mean axial vorticity (Ω_x), axial normal turbulent stress, summed cross-flow normal turbulent stresses ($(\overline{v^2} + \overline{w^2})$), turbulence kinetic energy (k), and turbulence kinetic energy production (P) shown in Figure 3.2.   Equation 3.1 contains the definition of k, and Equation 3.2 the definition of P (neglecting streamwise derivatives).

$$k = \frac{1}{2}(\overline{u^2} + \overline{v^2} + \overline{w^2}) \tag{3.1}$$

$$P = -\overline{v^2}\frac{\partial V}{\partial y} - \overline{w^2}\frac{\partial W}{\partial z} - \overline{uv}\frac{\partial U}{\partial y} - \overline{uw}\frac{\partial U}{\partial z} - \overline{vw}\left(\frac{\partial W}{\partial y} + \frac{\partial V}{\partial z}\right) \tag{3.2}$$

Mean cross-flow velocity vectors ($V\hat{\imath} + W\hat{\jmath}$) are shown in Figure 3.3, and a detailed view of the mean axial (V_x/U_∞) and tangential (V_θ/U_∞) velocity profile (measured in the z-direction through the core center) is shown in Figure 3.4.

Figures 3.1—3.4 show the vortex to consist of a small concentrated core surrounded by a circulating velocity field that has wound the wing wake into a spiral. This wake spiral dominates the turbulence structure outside the core—the region of axisymmetric turbulent flow around the core is small, if present at all. The turbulence measurements made at $x/c = 10$ (Figures 3.2c–e) indicate a variation of turbulence levels along the spiral. Far from the core, the flow is essentially a two-dimensional turbulent wake. Three-dimensional effects become apparent as one moves outboard. Peak turbulence levels first rise, reaching a maximum in the region where the wake begins to curve ($y/c = 0.1$, $z/c = 0.38$), and then fall as the core is approached along the spiral. Devenport *et al.* [43] show these variations to be a consequence of the mean rates of strain and lateral curvature suffered by the turbulence. These secondary strain rates, which are in places larger than the peak (primary) axial velocity gradient, appear in velocity spectra to be inhibiting the motions of larger turbulent eddies.

Moving into the core, the apparent turbulence levels increase dramatically as show in Figures 3.2c–e). Devenport *et al.* [43] show this to be a consequence of vortex core wandering with an r.m.s. amplitude between 11% and 35% of the vortex core radius, depending on streamwise position. This is also the likely cause of the uncertain contours of turbulence kinetic energy production near the core (Figure 3.2f). Some clues as to the true turbulence structure in the core region are given by the series of velocity autospectra shown in Figure 3.5.   These were measured at $x/c = 10$ along a z-wise profile from the spiral wake centerline ($y/c = -0.037, z/c = -0.160$) to the core center ($-0.037, 0.006$) (see Figure 3.2). At non-dimensional frequencies less than $fc/U_\infty = 20$, spectral levels rise as the core center is approached because of wandering and other inactive motions of the core. At frequencies greater than $fc/U_\infty = 20$—where the influence of smaller turbulent structures would be expected to be seen—spectral levels fall, becoming an order of magnitude smaller at the core center than they are in the wake. Even in the region just outside the core edge where the

mean tangential and axial rates of strain reach their maxima (*e.g.* $z/c = -0.039$), spectral levels in this frequency range are substantially lower than in the spiral wake. This could indicate that the velocity field of the vortex core may be generating little if any turbulence of its own.

In fact, Devenport *et al.* [43] demonstrate by several means that the core is laminar. They show the rate of evolution of the core mean velocity profiles to be consistent with laminar flow and that small scale turbulence levels in the core are very low. They also argue that the scaling of the high-frequency part of the velocity spectrum at the core center should reveal the scaling and therefore the source of any turbulent velocity fluctuations in the core. They find that the spectrum does not scale on parameters of the core mean-velocity field (implying an absence of any locally generated turbulence) but upon the axial velocity deficit and thickness of the unrolled-up portion of the spiral wake. They conclude that the core is laminar and that the velocity fluctuations within it are generated as the core is buffeted by turbulence in the surrounding spiral wake. Examples of this scaling are shown in Figure 3.6 where velocity autospectra measured in the core center at the six streamwise stations are shown normalized on the reference parameters U_∞ and c and on the velocity and length scales of the unrolled-up part of the spiral wake (U_g and L_g respectively).

Mean velocities obtained from a z-wise profile through the core at $x/c = 10$ are shown in Figure 3.4. The tangential (V_θ) velocity profile is closely antisymmetric about the core center and contains a steep gradient at the core center. The measured peak tangential velocity ($V_{\theta_{1m}}$) is $0.273\,U_\infty$ and the measured core radius (r_{1m})—defined as the radius where the peak tangential velocity occurs—is $0.036\,c$. Assuming an axisymmetric core, this implies a measured core circulation of $0.257\,\Gamma_0$ where Γ_0 is the root circulation of the vortex generator calculated using lifting line theory. The axial (V_x) velocity profile is approximately Gaussian in the vicinity of the core and has a value at the core centerline of $0.847\,U_\infty$. This measured deficit of $0.153\,U_\infty$ is presumed to be the result of the drag of the vortex generator superimposed on the surplus generated by the low pressure at the core center (see Batchelor [44], Moore and Saffman [45]). Devenport *et al.* [43] corrected the profile data in the vicinity of the core for wandering effects. Their method assumes that the velocity field of the undisturbed vortex core generates little or no turbulence of its own. After correction the core parameters become: core radius, $r_1 = 0.037c$; peak tangential velocity, $V_{\theta_1} = 0.286\,U_\infty$; core circulation, $\Gamma_1 = 0.274\,\Gamma_0$; core centerline axial velocity deficit, $U_d = 0.152\,U_\infty$.

The tangential velocity profile can also be used to estimate a circulation distribution $\Gamma(r)$ based upon circular paths centered on the vortex core assuming an axisymmetric mean velocity flowfield. The circulation distribution can also be calculated from the cross flow velocities measured in the y-z plane. Both of these estimates are shown in Figure 3.7. As can be seen from the mean streamwise vorticity contours (Figure 3.2b), the loose spiral of the blade wake contains a measurable amount of vorticity, showing the limitation of assuming axisymmetric flow. However, the y-z plane data is sparse near the core center (where the flow is likely to be more axisymmetric), therefore the circulation distribution calculated from the profile data is considered to be more reliable there.

These measured circulation distributions are compared with the predicted circulation distribution of the vortex using Betz's theory (Betz [46], simplified by Rossow [47] and Donaldson *et al.* [48]) which assumes inviscid two-dimensional flow and complete roll up of the vortex to an axisymmetric state. Lifting line theory was used to estimate the lift distribution of the vortex generator required for the Betz's theory calculation, and the theoretical root circulation (Γ_0) was used to normalize the curves. Γ/Γ_0 increases continuously with radius for both the measured and computed distributions, indicating that the vortex is stable according to Rayleigh's criterion. Outside the core region ($r/c > 0.1$) Betz's theory over-predicts the circulation distribution. Whether this disagreement is a consequence of the assumptions made by Betz or the limitations of the theoretical lift distribution on which the predictions were based is not clear. However, it does appear that the vortex is fully rolled up since measurements made at the other streamwise locations show little variation in circulation distribution with downstream distance.

Figure 3.8 shows the variations of the core parameters (corrected for wandering) with streamwise distance (values listed in Table 3.2). Consistent with laminar diffusion none of the parameters varies significantly over the measured streamwise length.

3.2.2 Angle of attack variations

Devenport *et al.* [43] also made velocity measurements at $x/c = 10$ with the vortex generator at angles of attack $2.5°$, $3.75°$, and $7.5°$ which are used here to characterize the inflow to the interaction blade as a function of vortex strength. Velocity profiles, circulation distributions, and core parameters corrected for wandering are presented in Figures 3.9–3.11 respectively. Numerical values of the core parameters are in Table 3.2. Cross-sectional turbulence measurements were not made in these cases, but turbulence stress profiles (not shown) and the scaling of velocity spectra measured at the core center (Figure 3.12) reveal a structure very similar to the one seen at $5°$ (*i.e.* a laminar core in which velocity fluctuations scale on the parameters of the surrounding spiral wake). The measurements show the vortex core size and the peak tangential velocity to increase approximately in proportion to the angle of attack. The proportion of the circulation contained within the core also increases from $16.4\% \, \Gamma_0$ at $2.5°$ to $32.8\% \, \Gamma_0$ at $7.5°$. The circulation distributions (Figure 3.10) for $\alpha_1 = 3.75°$ and $7.5°$ are quite similar to the $5°$ distribution out to $r/c = 0.25$. None of the distributions match the Betz's theory very well at locations outside the core region ($r/c > 0.1$) where the theory over predicts all of the distributions.

3.3 Evolution of flow after interaction

One objective of the present study was to document the evolution of the turbulent flowfield surrounding the vortex downstream of the interaction. To accomplish this, mean velocity and turbulence measurements were made from $0.16c$ to $15c$ downstream of the interaction blade trailing

edge at $x/c = 15.16, 15.95, 17.5, 20, 22.5, 25,$ and 30. Both the vortex generator and interaction blade at angles of attack of 5°, with a blade–vortex separation of $\Delta/c = -0.125$ (pressure side passage). A less detailed set of measurements at the same downstream locations after interaction was also made for a suction side passage of $\Delta/c = 0.125$. Measurement locations and conditions, and resulting vortex core parameters for these cases are summarized in Table 3.4.

3.3.1 Pressure side passage

Overall form of the interaction

At all seven locations downstream of the blade, cross-sectional measurements were made in the y-z plane. Contours of mean axial velocity deficit, mean axial vorticity, axial normal turbulent stress, summed cross-flow normal turbulent stresses $(\overline{v^2} + \overline{w^2})$, turbulence kinetic energy, and turbulence kinetic energy production are shown in Figures 3.13–3.18.   Scatter plots of the measurement locations are shown in Figure 3.19.   Both the y-z plane data and the z-wise profile data were used to determine the contours.

The initial effect of the blade on the vortex is to cut it in two. At $x/c = 15.16$ the turbulence contours (Figures 3.15–3.17) clearly show how the blade wake bisects the spiral arm of the vortex. Note that there is some dislocation of the spiral across the blade wake caused by differing spanwise velocities above the suction and below the pressure side surfaces of the blade. Vectors of the mean cross-flow velocities (Figure 3.20) clearly show a jump in the spanwise velocity component (V) which occurs above and below the line $z/c = -0.25$.   This $\partial V/\partial z$ contributes significantly to the streamwise vorticity $(\Omega_x = \partial W/\partial y - \partial V/\partial z)$ resulting in the region of negative vorticity centered at approximately $z/c = -0.25$ seen in Figure 3.14.

Progressing downstream, the vortex begins to distort and interact with the wake. Most noticeable is the tongue of turbulent fluid that forms between the core and wake between $x/c = 15.95$ and 17.5 (near $y/c = 0.55$, $z/c = -0.05$). Turbulence kinetic energy levels in the center of this region at $x/c = 17.5$ are 2.5 times as large as those in the undistorted sections of blade wake far from the vortex core. Another feature of the flow noticeable at the locations $x/c = 15.16, 15.95,$ and 17.5 is the thicker, more turbulent blade wake outboard of the vortex center (more negative y) than inboard. This was predicted from our discussion of the expected flow over the blade where it was mentioned that outboard of the vortex there is an increase in the local angle of attack on the blade, thereby increasing the thickness of the suction side boundary layer and the resulting wake—possibly to the extent that local separation occurs. Lifting of fluid away from the blade surface by the rotational motion of the vortex may also increase the wake thickness inboard of the vortex center, but this effect is clearly smaller here.

Further downstream, the intense region of new turbulence continues to grow, ultimately engulfing the core and producing a very large region of turbulence surrounding it. Confirming the formation of new turbulence rather than a simple roll-up of the blade wake are contours of tur-

bulence kinetic energy production (Figure 3.18). The large uncertainties (indicated by extreme gradients) seen in these contours in the core region are most likely the result of vortex core wandering effects (see Devenport *et al.* [43] for more information on these effects). Levels in the region between the blade wake and vortex core are over 10 times higher than those in the undisturbed portion of the blade wake at $x/c = 20$. Peak turbulence levels in the blade wake furthest from the vortex are decreasing with downstream distance as expected; but in the distorted portion, levels are not decreasing due to this significant amount of turbulence production. The distortion and rolling up of the blade wake is seen to continue after $x/c = 20$, progressing to a state where the two portions of the blade wake appear to be associated more with the vortex than each other.

Vortex instability

The magnification and intensification of the turbulent flowfield would be consistent with a new flow instability. The contours of mean axial vorticity and circulation distributions centered on the vortex provide some insight into the instability. For $x/c \leq 15.95$, vorticity contours (Figure 3.14) show strong positive values in the still compact vortex core as well as negative values in the blade wake. The negative vorticity region was shed from the blade in response to local angle of attack variations produced by the vortex (refer to Section 1.8). Initially, at $x/c = 15.16$, it spans over one chord. Moving downstream to $x/c = 20$, it has been distorted with the blade wake and levels decrease presumably because of turbulent mixing with the rest of the vortex.

When the region of negative streamwise vorticity in the blade wake is imposed on the vortex, a non-monotonic circulation distribution results. Figure 3.21 shows circulation, integrated around circular paths concentric with the vortex from the y-z plane data, plotted as a function of radius. In the undisturbed vortex, circulation increases continuously with radius. The negative streamwise vorticity shed by the interaction blade greatly reduces circulation for $r/c > 0.15$ producing a strongly non-monotonic variation. Non-monotonic circulation distributions are unstable according to Rayleigh's criterion and thus are expected to produce turbulence and rapidly diffuse. Indeed, downstream of $x/c = 17.5$ the peak in the circulation distribution begins to diffuse and by $x/c = 25$ the distribution has regained a monotonic form. The intense production seen at $x/c = 20$ and other locations is presumably associated with this instability.

The development of the vortex core parameters shown in Figure 3.22 were obtained from the detailed z-wise profiles through the core center plotted in Figure 3.23. (Circulation distributions calculated from these core profiles (Figure 3.24) are surprisingly similar to those calculated from the y-z plane data (Figure 3.21) since the flow within the core is the only area of the flowfield where axisymmetry is expected to dominate.) The core radius remains fairly constant until $x/c = 20$, with a small increase seen at $x/c = 22.5$, and then increases roughly linearly to a size about 67% larger than the undisturbed value. The effects of the interaction upon the tangential velocity field of the vortex core are felt significantly further upstream: there is a slight increase immediately

after the interaction, but it decreases steadily after $x/c = 15.95$ to 37% of the undisturbed value at $x/c = 30$. These changes result in the core circulation falling quickly between $x/c = 17.5$ and 22.5 likely due to the incorporation of the nearby negative vorticity into the core. A similar delay between the fall in the peak tangential velocity and the growth of core radius is also seen in the temporal variation of a Taylor vortex (which also has a similar region of negative vorticity surrounding its core) calculated by Sreedhar and Ragab [49].

Interestingly, the recovery to a monotonic circulation distribution does not appear to be accompanied by a return to vortex stability. The rapid decay of the core triggered by the non-monotonic circulation distribution causes the peak tangential velocity to fall below the centerline axial velocity deficit at $x/c = 30$. According to the stability computations of Mayer and Powell [50] and direct numerical simulations by Ragab and Sreedhar [51], such a vortex is unstable.

A note on wandering corrections

As with the inflow data, the coherent wandering motions of the vortex affect the measured values of the core parameters. Unfortunately, the assumption used for the undisturbed vortex data that turbulence levels in the core are almost entirely due to wandering is not believed to be valid after the interaction as evidenced by the velocity autospectra data presented in the next section. If the wandering is assumed to be produced by unsteady changes in the flow direction in the wind tunnel test section, the wandering amplitudes presented by Devenport *et al.* [43] for the isolated vortex can be used instead of assuming a laminar vortex core as done for the undisturbed vortex data. Tangential velocity profiles normalized on the measured core radius and peak tangential velocity as shown in Figure 3.25 are all of similar shape to Bachelor's [44] q-vortex profile defined as

$$\frac{V_\theta}{V_{\theta_1}} = \frac{r_1}{r}\left(1 + \frac{1}{2\alpha_q}\right)\left[1 - \exp\left(-\alpha_q\frac{r^2}{r_1^2}\right)\right] \quad \text{where } \alpha_q = 1.25643. \tag{3.3}$$

Therefore, the analytical equations derived by Devenport *et al.* [43] can be used to correct the measured core parameters. All of the core parameters presented in this study have been corrected for wandering effects in this fashion.

Spectral decomposition

Velocity autospectra were measured in the vortex core center at each location downstream of the interaction. Autospectra normalized on free-stream velocity and chord length as a function of downstream distance is shown in figure 3.26. For a while following the interaction ($x/c = 15.16$, 15.95, and 17.5), the autospectra drop rapidly at high frequencies ($fc/U_\infty > 6$) similar to the undisturbed vortex, suggesting that the core is still laminar.[1] However, further downstream ($x/c \geq 20$) autospectra appear to indicate that a fundamental change in the turbulence structure

---

[1]Devenport *et al.* [43] provide detailed evidence that the undisturbed vortex core is laminar as discussed in Section 3.2.

has occurred—levels at all frequencies jump up at least one-half a decade and a short inertial sub-range develops. These changes may signal that the core has become turbulent. Spectral levels at frequencies above $fc/U_\infty = 20$ are at least an order of magnitude greater than those seen upstream at $x/c = 15.16$ to 17.5. This change in turbulence structure of the core corresponds directly to the growth of the core radius which is seen to occur shortly after $x/c = 20$.

The jump in spectral levels and the change in spectral shape seen between $x/c = 17.5$ and 30 persists regardless of the manner in which the spectra are normalized. However, different normalizations do provide a measure of collapse of the spectra for $x/c \le 17.5$ and for $x/c \ge 20$ implying some scaling of the velocity fluctuations. Figures 3.27–3.30 show the spectra re-plotted as $G_{uu}U_\infty/(V_s^2 L_s)$ $vs.$ fL_s/U_∞, where U_s and L_s are respectively; the velocity (U_g) and width (L_g) scales of the vortex generator wake (Figure 3.27), the velocity (U_b) and width (L_b) scales of the interaction blade wake (Figure 3.28), the core centerline axial velocity deficit (U_d) and radial scale of the deficit profile (d) of the vortex (Figure 3.29), and the peak tangential velocity $(V_{\theta 1})$ and radius (r_1) of the vortex core (Figure 3.30).   The normalizations presume that the convective velocity of any disturbances should be close to U_∞.

The best normalization for locations $x/c \le 17.5$ was obtained using the velocity and length scales of the generator wake (Figure 3.27 obtained from the isolated vortex study by Devenport et $al.$ [43]. Their data indicated that the evolution of the axial velocity and turbulence profiles in the flat portion of the wake far from the core was well described by only one length and one velocity scale, which respectively grow and decay approximately as the square root of the streamwise distance. Using this normalization, the autospectra collapse onto two distinct bands. For frequencies $fL_g/U_\infty > 2$ the spectra for $x/c = 10$, 15.16, 15.95 and 17.5 collapse onto nearly the same curve. The collapse of the curves further downstream $(x/c \ge 20)$ is not easily explained and is most likely coincidence. Devenport et $al.$ [43] conclude that this scaling works in the case of the undisturbed vortex because the velocity fluctuations in the laminar flow core are the result of inactive motions produced as it is buffeted by the surrounding wake turbulence. In the present case the close proximity of the highly turbulent blade wake would appear to make it a more reasonable flow feature to scale upon, especially downstream where the vortex appears to be associated more closely with the blade wake. Using the characteristic length and velocity scales of the undistorted portion of the blade wake shows improving collapse of the spectra with downstream distance (Figure 3.28). However, scales based on the axial velocity deficit profile of the vortex core provide a more significant amount of collapse for $x/c \ge 20$ especially in the mid-frequency range $(0.2 \le fd/U_\infty \le 20)$. If the velocity fluctuations were a consequence of the turbulence generated by the rotational motion of the core, $V_{\theta 1}$ and r_1 would seem to be appropriate scales. This is clearly not the case as shown in Figure 3.30. Note that the curves for $x/c \le 17.5$ show the same correlation as the normalization using the constant values of U_∞ and c since $V_{\theta 1}$ and r_1 are also roughly constant over this range of x/c.

Turbulence kinetic energy production

The interaction between the positive vorticity of the vortex and the negative vorticity of the blade wake has been identified as the cause of the turbulence kinetic energy production. A closer look at the contours of turbulence kinetic energy production and axial normal stress at $x/c = 17.5$ is shown in Figure 3.31. A series of points evenly spaced by $0.025c$ has been identified on the contours which starts in the center of the nearly two-dimensional portion of the interaction blade wake, and follows the ridge of maximum axial normal stress levels (indicative of the wake centerline) towards the peak at $(0.55, -0.03)$. At each point, an aligned coordinate system is defined such that the s direction is tangent to the curve which passes though the points and the n direction points towards the center of curvature.[2] The turbulence kinetic energy production in this coordinate system is

$$P = \left(\overline{v_n^2} - \overline{v_s^2} \right) \frac{\partial V_s}{\partial s} - \overline{uv_s}\frac{\partial U}{\partial s} - \overline{uv_n}\frac{\partial U}{\partial n} - \overline{v_s v_n}\left(\frac{\partial V_n}{\partial s} + \frac{\partial V_s}{\partial n} \right) \qquad (3.4)$$

if streamwise derivatives are ignored and continuity is satisfied. Figure 3.32 shows the production remains roughly constant between Locations 1 and 5 and increases approximately exponentially between Locations 5 and 22 where the wake has been significantly distorted by the vortex. The fractional contributions of each production term of Equation 3.4 is shown in Figure 3.33. Two terms: $-\overline{uv_s}(\partial U/\partial s)$ and $-\overline{uv_n}(\partial U/\partial n)$, can immediately be discounted as major sources of production; although, $-\overline{uv_n}(\partial U/\partial n)$ is certainly the main source of production in the two-dimensional wake away from its centerline. The main sources of production can therefore be attributed to the rates of stretching $(\partial V_s/\partial s)$ and skewing $(\partial V_n/\partial s + \partial V_s/\partial n)$ experienced by the blade wake. Figure 3.34 shows that these strain rates increase along the path due to the rotational field of the vortex; reaching maxima near Location 25 where the blade wake appears to form a cusp. These strain rates would be expected to lead to anisotropy in the stress field due to the stretching of the in-plane vorticity of the large, "energy-containing" eddies (see Tennekes and Lumley [52]). Since significant amounts of spanwise vorticity exist in the interaction blade wake, the distortion of the wake would be expected to cause an increase in anisotropy. Indeed, the quantities $\left(\overline{v_n^2} - \overline{v_s^2} \right) \partial V_s/\partial s$ and $-\overline{v_s v_n}$ increase along the path towards the cusp (Figure 3.35), thereby contributing to the turbulence production.

3.3.2 Suction side passage

Velocity profiles were taken through the center of the vortex core for suction side passage of $\Delta/c = 0.125$ at $x/c = 15.16$, 15.95, 17.5, 20, 22.5, 25, and 30 (Figure 3.36[3]). The profiles appear very similar to those for pressure side passage (Figure 3.23) with the obvious difference that the

---

[2]Mean velocities in the s and n directions are denoted V_s and V_n respectively. Fluctuating velocities in the s and n directions are denoted v_s and v_n respectively.

[3]The $x/c = 30$ profile is not plotted due to drift associated with a failing sensor, but it is believed that the core parameters derived from this profile are reasonably accurate.

blade wake lies on the other side of the vortex core. The axial velocity profile at $x/c = 15.16$ shows the blade wake to be centered at approximately $r/c = 0.13$ (several points are off the scale of the figure). This is about $0.04\,c$ closer to the vortex center than the pressure side passage case. Therefore, the negative vorticity contained in the blade wake is initially closer to the vortex core also evidenced by the tangential velocity profile and the circulation distribution estimated from the profile (Figure 3.37). Velocity autospectra measured in the core center normalized on vortex generator wake scales (Figure 3.38) suggest that a laminar to turbulent transition of the vortex core may occur at approximately $x/c = 17.5$: slightly further upstream than for pressure side passage (Figure 3.26) which occurred between $x/c = 17.5$ and 20. The earlier transition is not surprising considering that the blade wake was initially closer to the vortex core for suction side passage.

Vortex core parameters are presented in Figure 3.22 and Table 3.4 along with the values for pressure side passage for comparison. Similar to the downstream development of a pressure side passage, the peak tangential velocity increases before a growth in core radius. There is a noticeable decrease in the core radius from $x/c = 15.16$ to 17.5 which is intriguing because the aforementioned large eddy simulation of a Taylor vortex by Sreedhar and Ragab [49] also showed an initial decrease in the core radius before increasing later after the core became turbulent. After the initial decrease, the core radius consistently increases after $x/c = 17.5$—again correlating directly with the hypothesized core transition. The overall trend of the core radii, peak tangential velocities, and implied core circulations is that the suction side passage has a stronger effect on the vortex. Since for $|\Delta/c| = 0.125$ it appears that the interaction of the vortex with the blade wake causes the vortex core to become turbulent, facilitating the reorganization of the vortex core; the closer proximity of the blade wake for suction side passage explains both the earlier transition and the differences seen in the core parameter trends.

3.4   Effects of blade–vortex separation

The present study also examined the effects of blade–vortex separation through measurements made at $x/c = 30$ for a range of separations between $\pm 0.5\,c$. To determine a baseline variation for this study, the vortex generator and the interaction blade were both set at angles of attack of $5°$, and measurements were for both pressure and suction side passages of the vortex. Other configurations were also studied to determine the effects of blade angle of attack, vortex strength, and core radius on the baseline variation. All of the measurement locations and conditions, and resulting vortex core parameters for these cases are summarized in Table 3.5.

3.4.1   Baseline variation

Velocity measurements were made for fourteen different blade–vortex separations between $\pm 0.5\,c$ at $x/c = 30$, with $\alpha_1 = \alpha_2 = 5°$. Velocity profiles for pressure side passages are shown in Figure 3.39,

suction side passages in Figure 3.40.   The velocity profiles in the core region ($r/c < 0.1$) appear to be unaffected by the interaction (or lack thereof) for blade–vortex separations greater than $0.25\,c$. Core center velocity autospectra (Figures 3.41–3.42) suggest laminar flow in the cores for $\Delta/c = \pm 0.5$ and ± 0.375 by the steep roll-off of the spectra at frequencies $fc/U_\infty > 6$—levels are uniformly higher for $\Delta/c = \pm 0.375$.   The extremely high spectral levels of the summed cross-flow autospectra ($G_{vv} + G_{ww}$) at low frequencies ($fc/U_\infty < 3$) are a result of wandering motions of the core. For separations of $\pm 0.25\,c$, the peak tangential velocity is seen to decrease slightly, while the core radius remains constant. At these separations, high frequency axial velocity autospectral levels in the core center have increased to roughly 10 times those levels seen for $\Delta/c = \pm 0.375$, with the high frequency roll-off being not quite as steep, possibly due to intermittency between laminar and turbulent flow. For separations smaller than $0.25\,c$, the velocity gradient in the core is considerably weakened. This is presumably due to the core becoming turbulent as evidenced by the change in shape of the velocity autospectrum at frequencies above $fc/U_\infty = 3$.

Plots of the core parameters shown in Figure 3.43 (Table 3.6 contains data) indicates that enough separations were considered to define the functional variations.   The core radius is not significantly affected for $|\Delta/c| \geq 0.25$, but is greatly increased for smaller separations. The peak tangential velocity at the core edge is more sensitive, there being a significant effect of the interaction for blade vortex separations less than $0.375\,c$. All the effects are very dramatic for small blade–vortex separations. For example, the peak tangential velocity is less than 20% of its undisturbed value for $\Delta/c \leq 0.0625$, while the core radius is between 3 and 6 times larger than its undisturbed value in this range, resulting in a loss in core circulation of over 40%. The decrease in peak tangential velocity seen at separations where the vortex core radius is unaffected indicates that the vortex core has only recently become turbulent. This conclusion is drawn from the the downstream development of the flow discussed in Section 3.3 which showed the growth in core radius lags the decrease in peak tangential velocity.

The data indicates that the core is weakened most for a separation of $0.0312\,c$ with the variations being fairly symmetric about this value. This difference was also discussed in Section 3.3.2 where it was seen that the blade wake was initially closer to the core center for suction side passage of the vortex. This resulted in a weaker vortex core compared to pressure side passage. Several factors may be causing this, each with an unknown contribution. Uncertainty in the zero Δ location of the blade may be one; due to changes in the flow angularity of the wind tunnel between the speed where the helium bubble flow visualization was done (Re_c =260,000), and the speed at which measurements were taken ($Re_c = 530,000$). The other possible causes are much more complex. The vortex experiences a complex pressure gradient field at close separations—with suction side passages likely to have larger gradients—which may lead to vortex bursting or other instabilities. For separations less than $0.031\,c$, the helium bubble flow visualizations performed by Rife and Devenport [53] on a similar configuration suggest that the vortex core is split by the blade into two

separate vortical structures which remain distinct for several chord lengths downstream. Vortex splitting effects might not be symmetric with respect to Δ. The viscous interaction with the blade boundary layer is yet another effect which will differ depending on which side the vortex passes: note that the measured suction side boundary layer is significantly thicker (Table 2.1).

Velocity measurements were made in the y-z plane with $\Delta = 0$ to reveal the cross-sectional structure of the flow field surrounding the core. The turbulent flowfield, represented by the contours of turbulence kinetic energy shown in Figure 3.44a, indicates that blade wake is even more distorted by the interaction with the vortex for zero separation compared to pressure side passage of $\Delta/c = -0.125$ (Figure 3.17). Also apparent is the expected thicker, more turbulent blade wake on the outboard side of the vortex core (more negative y)—features discussed in Section 3.3.1.

Turbulence levels near the core center for $\Delta/c = 0$ are roughly one-fourth the levels with $\Delta/c = -0.125$. If the vortex core is split as it passes the blade, a very complex, highly turbulent vorticity field is likely to exist just downstream of the blade. Contours of mean axial vorticity (Figure 3.44b) show that there is a weak organization of vorticity at $x/c = 30$. It is therefore hypothesized that the vorticity is quickly diffused and reorganized to the point where turbulence producing strain rates are small, allowing the turbulence levels to decay significantly with downstream distance.

3.4.2 Decreased blade angle of attack

To examine the effects of blade angle of attack on the functional variation of core parameters with blade–vortex separation, measurements were made with the blade at zero angle of attack, $i.e.$ $\alpha_2 = 0°$. All other factors were same as the baseline variation. Measurement locations and conditions, and vortex core parameters for these cases are summarized in Table 3.5. All passages were with the vortex on the same side of the blade. These passages were all considered to be 'suction side' ($\Delta \leq 0$) passages because the vortex passed on what would have been the suction side of the blade if it were at a positive angle of attack as in the baseline variation. Since the undisturbed inflow vortex was shown in Section 3.2 to be non-axisymmetric, this may be of some importance.

Mean velocity profiles (Figure 3.45) vary in a fashion similar to those for the baseline variation (Figures 3.39 and 3.40). As the blade–vortex separation is decreased, a decrease in peak tangential velocity occurs before the core radius is seen to increase. Core center velocity autospectra (Figure 3.46) indicate laminar flow in the core for $\Delta/c = 0.375$ (by the steep roll-off of the spectra at frequencies $fc/U_\infty > 6$), and turbulent flow for all of the closer separations. The extremely high spectral levels of the summed cross-flow autospectra at low frequencies ($fc/U_\infty < 3$) are a result of wandering motions of the core.

The core parameters are plotted as functions of blade–vortex separation in Figure 3.43 (values listed in Table 3.5) as well as the values for $\alpha_2 = 5°$ (the baseline variation). As previously discussed, these data show an increase in vortex core size and a reduction in the peak tangential

velocity with decrease in the magnitude of the blade–vortex separation. These effects appear to be largely independent of the blade angle of attack. This might be expected since an inviscid analysis (see Section 4.1) shows that the vortex sheet shed from the blade is independent of its angle of attack, and changes to the core occur have been shown to occur primarily due to its interaction with the negative part of that sheet. The only significant effects of blade angle of attack are seen in the core radius for blade–vortex separations less than the initial core size of $0.037\,c$. As mentioned in Section 3.4.1, for such close separations the vortex core might be split by the blade. This complicates the flowfield greatly, and there is no reason to assume that splitting effects would be independent of the interaction blade angle of attack.

3.4.3 Increased vortex strength

To examine the effects of initial vortex strength on the functional variation of core parameters with blade–vortex separation, measurements were made with the vortex generator at an angle of attack of $10°$. All other factors were the same as the baseline variation. Measurement locations and conditions, and vortex core parameters for these cases are summarized in Table 3.5.

Mean velocity profiles are shown in Figure 3.47 and core center velocity autospectra in Figure 3.48. The autospectra suggest laminar flow in the core for $\Delta/c = 0.5$ and 0.375, and turbulent flow for all closer separations (as in the baseline variation). The core parameters are plotted as functions of blade–vortex separation in Figure 3.49 (values listed in Table 3.5) as well as the values for $\alpha_1 = 5°$ (the baseline variation). Initially, the effects of the interaction appear heavily dependent upon the generator angle of attack. Although in both cases, as the magnitude of the blade–vortex separation is decreased, a decrease in peak tangential velocity occurs before the core radius is seen to increase. If these parameters are normalized on their undisturbed values measured at $x/c = 10$ ($r_1|_{10}$ and $V_{\theta_1}|_{10}$) then the effects of the generator angle of attack appear much weaker as shown in Figure 3.50. Since the strength of the vorticity shed by the blade would be proportional to the vortex strength, the nature of the interaction therefore appears to be more dependent upon the spacial arrangement of the vorticity field than it is on the absolute strengths of the vorticity regions involved.

3.5 Angle of attack variations with fixed blade–vortex separation

Several measurements were made at $x/c = 30$ for different angle of attack combinations of the vortex generator and interaction blade with a fixed blade–vortex separation of $-0.125\,c$. Table 3.6 summarizes the measurement locations and conditions, and vortex core parameters for these cases.

3.5.1 Changing interaction blade angle of attack

As discussed in Section 3.4.2, the blade angle of attack appeared to have little effect on the variation of the core parameters as a function of the blade–vortex separation. Additional measurements were made at $x/c = 30$, for a fixed blade–vortex separation of $-0.125\,c$ to confirm this observation. The vortex generator angle of attack remained constant at $5°$. Blade angles of attack of $2.5°$ and $7.5°$ were studied in addition to $5°$.

The mean velocity profiles shown in Figure 3.51 indicate that increasing the blade angle of attack does have a small effect on the velocity profiles, causing a reduction in peak tangential velocity of and increase in core radius. Interestingly, the small effects the blade angle of attack has on the core radius and peak tangential velocity are of equal proportion (about 30%) resulting in nearly identical core circulations (Table 3.6). The complex pressure gradient field the vortex experiences as it passes the blade—the magnitudes of which increase with blade angle of attack—may be one source of the differences seen. Also, the viscous interaction with the blade boundary layer will differ with blade angle of attack. Downstream of the blade, its turbulent wake will initially be wider and stronger for increasing angles of attack—effects which are likely to increase vortex instability and more rapidly diffuse vorticity. Velocity autospectra (Figure 3.52) show nearly identical turbulence structures in the core centers with the u-component being slightly less for $\alpha_2 = 5°$ and $7.5°$ presumably due to the vortex core becoming turbulent further upstream than for $\alpha_2 = 2.5°$.

3.5.2 Changing vortex strength and blade angle of attack simultaneously

Measurements were made at $x/c = 30$ with a fixed blade–vortex separation of $-0.125\,c$ for a range of vortex strengths (controlled by α_1) and blade angles of attack (α_2) where $\alpha_1 = \alpha_2$. Table 3.6 summarizes the measurement locations and conditions, and vortex core parameters for these cases. Angles studied were from $2.5°$ to $10°$.

Mean velocity profiles are shown in Figure 3.53. The core parameters (Figure 3.54) show that the variation in core radius is roughly parabolic in shape with a minimum value of $0.058\,c$ for $3.75°$ and a value over 5 times as large at $10°$. Interestingly enough, the variation in the peak tangential velocity is such that the core circulation remains almost constant. Core center velocity autospectra (Figure 3.55) are all of a similar turbulent shape, with levels increasing with angle from $2.5°$ to $6.25°$, then decreasing from $6.25°$ to $10°$. The practical destruction of the vortex core measured with $\alpha_1 = \alpha_2 = 10°$ shows that the generalizations made about the interaction being independent of both the vortex strength and the blade angle of attack do not hold for this extreme case.

Measurements were made in the y-z plane for $\alpha_1 = \alpha_2 = 2.5°$ and $7.5°$ in addition to the ones made with $\alpha_1 = \alpha_2 = 5°$ which were presented in Section 3.3.1. Contours of turbulence kinetic energy are shown in Figure 3.56 for $\alpha_1 = \alpha_2 = 2.5°$ and $7.5°$ (see Figure 3.17 for $\alpha_1 = \alpha_2 = 5°$) showing that increased angles produce a much larger and more turbulent region of flow. This would

be expected since the increased strength of the vortex generator causes more negative vorticity to be shed by the blade and it is the interaction of the vortex with this negative vorticity which is responsible for the turbulent region.

x/c	α_1 (°)	α_2 (°)	Δ/c
15.16	5	5	±0.125
15.95	5	5	±0.125
17.5	5	5	±0.125
20	5	5	±0.125
22.5	5	5	±0.125
25	5	5	±0.125
30	5	5	±0.125
30	5	5	±0.5
30	5	5	±0.375
30	5	5	±0.25
30	5	5	±0.125
30	5	5	0.0938
30	5	5	±0.0625
30	5	5	±0.0312
30	5	5	0
30	5	0	0.375
30	5	0	0.25
30	5	0	0.125
30	5	0	0.0938
30	5	0	0.0625
30	5	0	0.0312
30	5	0	0
30	10	5	0.5
30	10	5	0.375
30	10	5	0.25
30	10	5	0.125
30	10	5	0.0938
30	10	5	0.0625
30	10	5	0.0312
30	10	5	0
30	5	2.5	−0.125
30	5	5	−0.125
30	5	7.5	−0.125
30	2.5	2.5	−0.125
30	3.75	3.75	−0.125
30	5	5	−0.125
30	6.25	6.25	−0.125
30	7.5	7.5	−0.125
30	10	10	−0.125

Table 3.1: Measurement locations and conditions for study of BVI effects

x/c	α_1 ($^\circ$)	r_1/c	V_{θ_1}/U_∞	Γ_1/Γ_0	U_d/U_∞
5	5	0.036	0.286	0.267	0.165
10	5	0.037	0.286	0.275	0.152
15	5	0.036	0.277	0.260	0.141
20	5	0.040	0.278	0.287	0.153
25	5	0.033	0.275	0.236	0.147
30	5	0.036	0.263	0.248	0.160
10	2.5	0.019	0.166	0.164	0.144
10	3.75	0.021	0.231	0.167	0.160
10	5	0.037	0.286	0.275	0.152
10	7.5	0.045	0.422	0.328	0.085

Table 3.2: Measurement locations and conditions, and resulting core parameters of undisturbed generator vortex. Data from Devenport *et al.* [43].

Quantity	Uncertainty	
	Wake	Core
U/U_∞	0.015	0.015
V/U_∞	0.015	0.015
W/U_∞	0.015	0.015
$\overline{u^2}/U_\infty^2$	3.1×10^{-6}	1.4×10^{-5}
$\overline{v^2}/U_\infty^2$	9.5×10^{-6}	1.5×10^{-5}
$\overline{w^2}/U_\infty^2$	9.9×10^{-6}	2.0×10^{-5}
$\overline{uv}/U_\infty^2$	4.3×10^{-6}	1.4×10^{-5}
$\overline{vw}/U_\infty^2$	4.5×10^{-6}	2.3×10^{-5}
$\overline{uw}/U_\infty^2$	2.9×10^{-6}	8.5×10^{-6}

Table 3.3: Uncertainties in velocity measurements calculated for 20:1 odds at typical locations in wake and core regions

x/c	α_1 (°)	α_2 (°)	Δ/c	r_1/c	V_{θ_1}/U_∞	Γ_1/Γ_0	U_{d}/U_∞
10	5			0.037	0.286	0.275	0.152
15.16	5	5	-0.125	0.035	0.303	0.279	0.182
15.95	5	5	-0.125	0.036	0.318	0.296	0.149
17.5	5	5	-0.125	0.036	0.294	0.275	0.144
20	5	5	-0.125	0.035	0.232	0.215	0.167
22.5	5	5	-0.125	0.039	0.177	0.179	0.160
25	5	5	-0.125	0.047	0.139	0.173	0.138
30	5	5	-0.125	0.061	0.105	0.168	0.111
10	5			0.037	0.286	0.275	0.152
15.16	5	5	0.125	0.036	0.310	0.289	0.173
15.95	5	5	0.125	0.033	0.297	0.255	0.159
17.5	5	5	0.125	0.031	0.264	0.251	0.178
20	5	5	0.125	0.036	0.179	0.168	0.181
22.5	5	5	0.125	0.050	0.121	0.158	0.153
25	5	5	0.125	0.055	0.104	0.149	0.132
30	5	5	0.125	0.062	0.065	0.105	0.130

Table 3.4: Measurement locations and conditions, and resulting core parameters for investigation of downstream development after interaction

x/c	α_1 (°)	α_2 (°)	Δ/c	r_1/c	V_{θ_1}/U_∞	Γ_1/Γ_0	$U_{\rm d}/U_\infty$
30	5	5	-0.5	0.035	0.305	0.275	0.131
30	5	5	-0.375	0.037	0.294	0.283	0.138
30	5	5	-0.25	0.037	0.256	0.250	0.140
30	5	5	-0.125	0.061	0.105	0.168	0.111
30	5	5	-0.0625	0.109	0.056	0.158	0.076
30	5	5	-0.0312	0.139	0.039	0.143	0.066
30	5	5	0	0.174	0.023	0.105	0.048
30	5	5	0.0312	0.199	0.021	0.107	0.027
30	5	5	0.0625	0.159	0.034	0.140	0.041
30	5	5	0.0938	0.101	0.039	0.102	0.072
30	5	5	0.125	0.062	0.065	0.105	0.130
30	5	5	0.25	0.038	0.237	0.235	0.142
30	5	5	0.375	0.036	0.291	0.272	0.136
30	5	5	0.5	0.034	0.302	0.270	0.131
30	5	0	0.375	0.037	0.267	0.260	0.148
30	5	0	0.25	0.038	0.221	0.222	0.153
30	5	0	0.125	0.071	0.081	0.149	0.106
30	5	0	0.0938	0.109	0.050	0.142	0.074
30	5	0	0.0625	0.146	0.033	0.127	0.057
30	5	0	0.0312	0.595	0.022	0.342	0.021
30	5	0	0	0.580	0.021	0.311	0.048
30	10	5	0.5	0.053	0.498	0.342	0.030
30	10	5	0.375	0.053	0.426	0.293	0.070
30	10	5	0.25	0.053	0.298	0.205	0.214
30	10	5	0.125	0.119	0.103	0.160	0.144
30	10	5	0.0938	0.141	0.081	0.149	0.124
30	10	5	0.0625	0.200	0.054	0.141	0.090
30	10	5	0.0312	0.250	0.041	0.132	0.042
30	10	5	0	0.450	0.043	0.253	0.039
30	5	5	0.5	0.216	0.072	0.409	0.087
30	5	5	0.25	0.189	0.057	0.283	0.085
30	5	5	0.125	0.194	0.039	0.199	0.058
30	5	5	0.125	0.246	0.039	0.251	0.073
30	5	5	0.0625	0.260	0.031	0.211	0.056
30	5	5	0	0.465	0.024	0.286	0.034
30	5	5	0	0.444	0.023	0.267	0.047
30	5	5	-0.125	0.456	0.029	0.351	0.030
30	5	5	-0.125	0.248	0.032	0.208	0.078
30	5	5	0.5	0.375	0.047	0.459	0.074
30	5	5	0.25	0.420	0.025	0.269	0.063
30	5	5	0.125	0.680	0.017	0.309	0.056
30	5	5	0.125	0.596	0.024	0.374	0.060
30	5	5	0.0625	0.649	0.022	0.373	0.058
30	5	5	0	0.680	0.017	0.309	0.025
30	5	5	0	0.656	0.023	0.395	0.035
30	5	5	-0.125	0.440	0.020	0.230	0.016
30	5	5	-0.125	0.577	0.024	0.362	0.058

Table 3.5: Measurement locations and conditions, and resulting core parameters for investigation of blade–vortex separation effects

x/c	α_1 (°)	α_2 (°)	Δ/c	r_1/c	V_{θ_1}/U_∞	Γ_1/Γ_0	$U_{\rm d}/U_\infty$
30	5	2.5	-0.125	0.052	0.123	0.167	0.116
30	5	5	-0.125	0.061	0.105	0.168	0.111
30	5	7.5	-0.125	0.068	0.093	0.164	0.098
30	2.5	2.5	-0.125	0.058	0.056	0.170	0.065
30	3.75	3.75	-0.125	0.055	0.093	0.178	0.092
30	5	5	-0.125	0.061	0.105	0.168	0.111
30	6.25	6.25	-0.125	0.072	0.110	0.166	0.114
30	7.5	7.5	-0.125	0.104	0.093	0.168	0.111
30	10	10	-0.125	0.300	0.054	0.212	0.055

Table 3.6: Measurement locations and conditions, and resulting core parameters for investigation of angle of attack variations with fixed blade–vortex separation
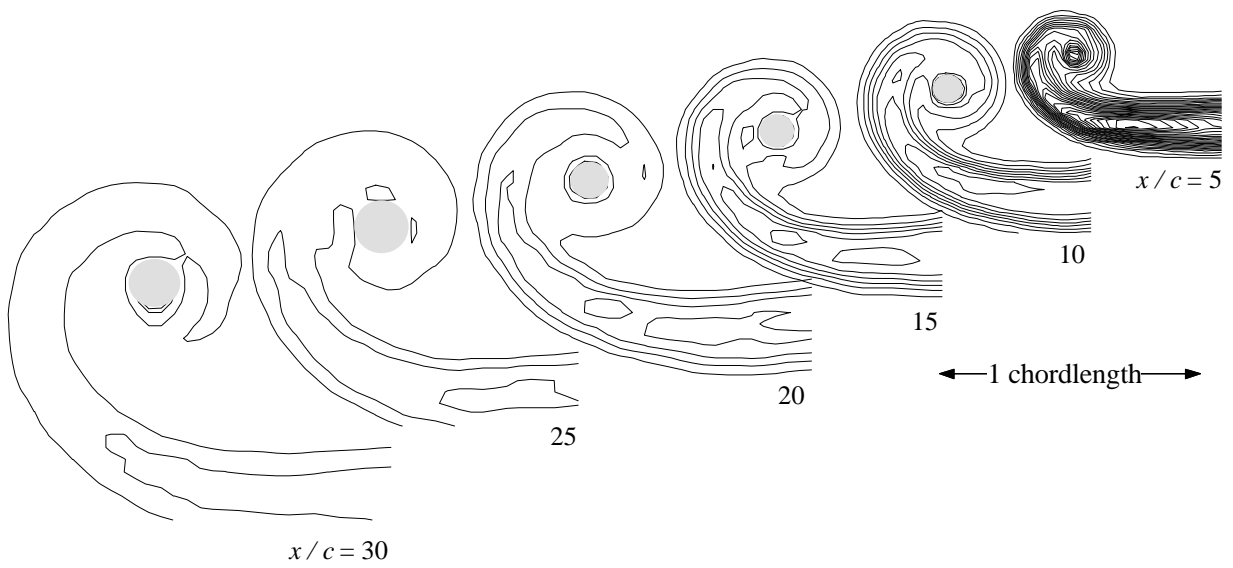
Figure 3.1: Contours of axial normal stress $(\overline{u^2}/U_\infty^2)$ downstream of vortex generator $(\alpha_1 = 5°)$ measured with the interaction blade removed. Contours are at intervals of 5×10^{-5}. Shaded regions are where the contribution from wandering exceeds 30% of the measured stress. Taken from Devenport *et al.* [43].

(a) $(1 - U)/U_\infty$

(b) $\Omega_x c/U_\infty \times 10$

(c) $\overline{u^2}/U_\infty^2 \times 10^5$

(d) $(\overline{v^2} + \overline{w^2})/U_\infty^2 \times 10^5$

(e) $k/U_\infty^2 \times 10^5$

(f) $Pc/U_\infty^3 \times 10^5$
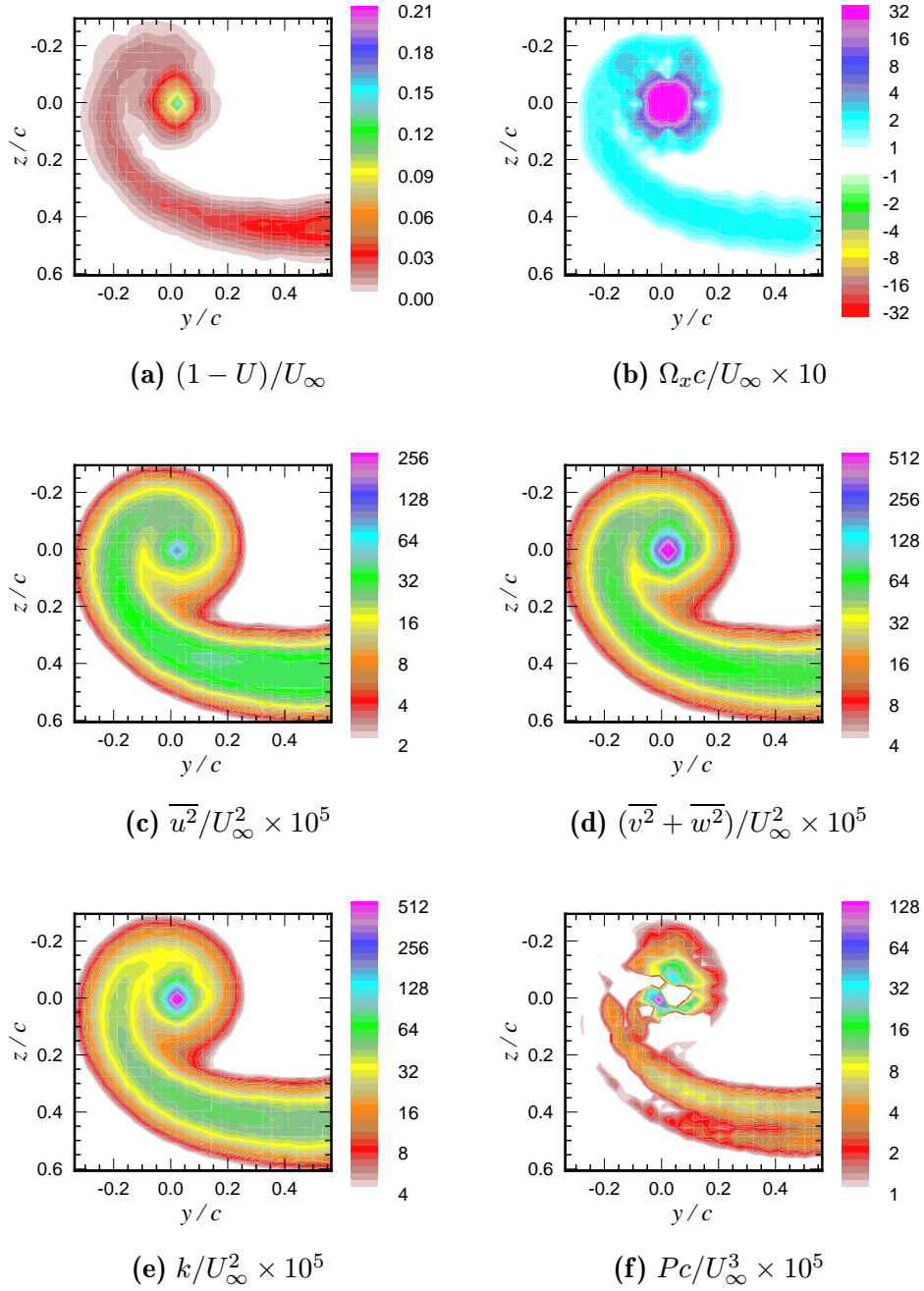
Figure 3.2: Contours of: **(a)** mean axial velocity deficit, **(b)** mean axial vorticity, **(c)** axial normal turbulent stress, **(d)** summed cross-flow normal turbulent stresses, **(e)** turbulence kinetic energy, and **(f)** turbulence kinetic energy production, downstream of vortex generator ($\alpha_1 = 5°$) at $x/c = 10$. Data from Devenport *et al.* [43].
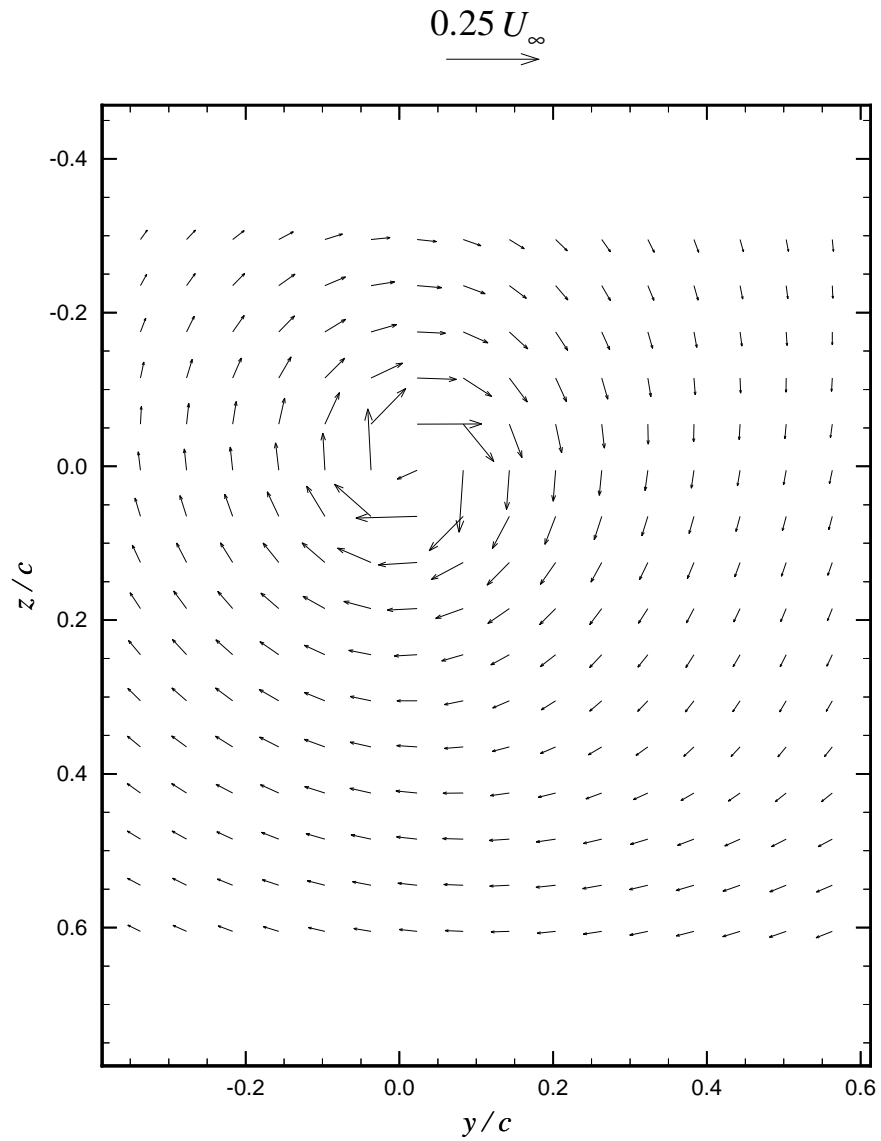
Figure 3.3: Mean cross flow velocity vectors $(V\hat{\imath} + W\hat{\jmath})$ downstream of vortex generator $(\alpha_1 = 5°)$ at $x/c = 10$. Data from Devenport *et al.* [43].
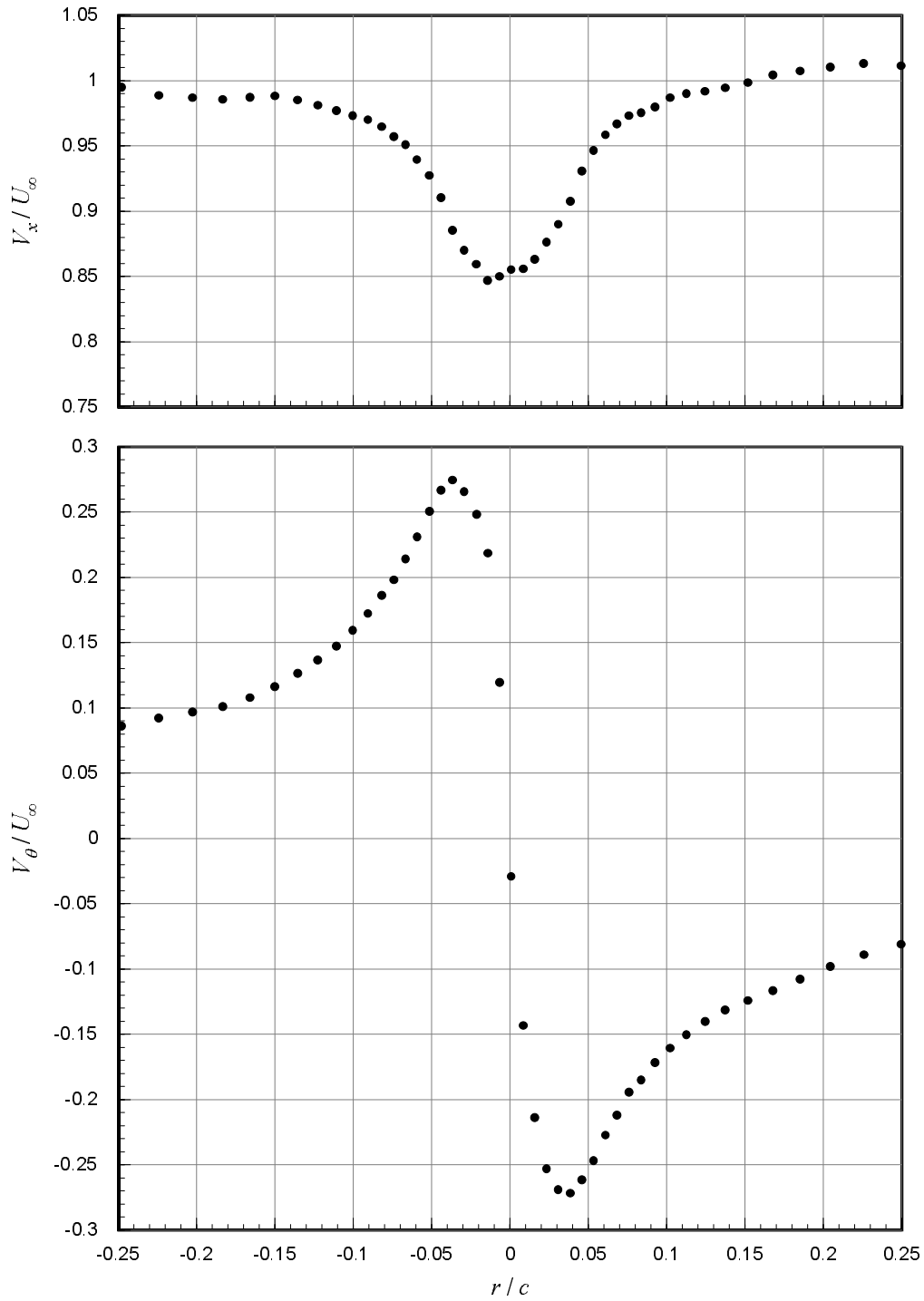
Figure 3.4: Mean axial and tangential velocities at $x/c = 10$ measured along a z-wise profile through the vortex core center ($\alpha_1 = 5°$). Data from Devenport *et al.* [43].
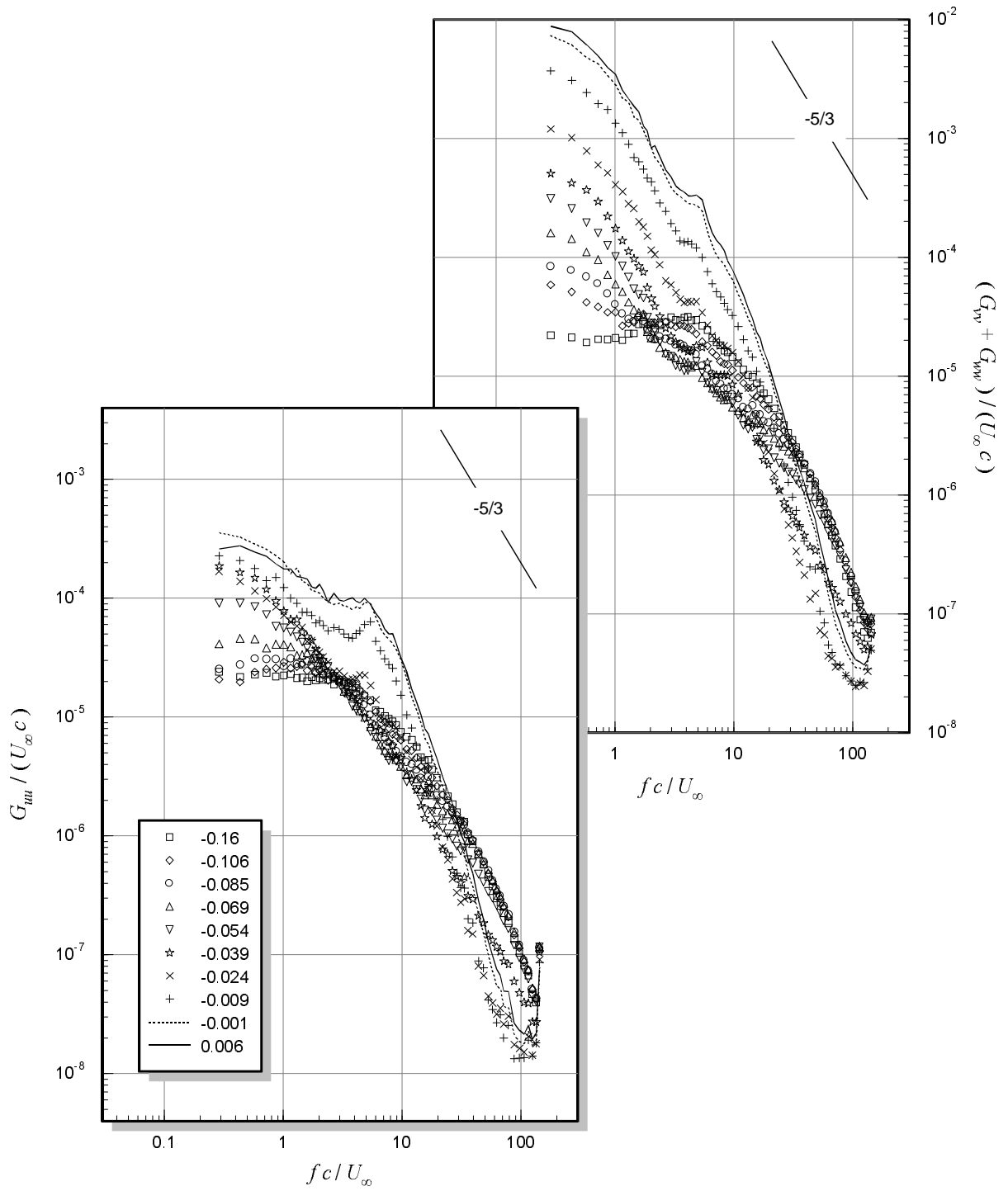
Figure 3.5: Velocity autospectra measured at $x/c = 10$ through along the line $y/c = -0.037$. $\alpha_1 = 5°$. Numbers in legend are z/c locations (core center at 0.006). Data from Devenport *et al.* [43].
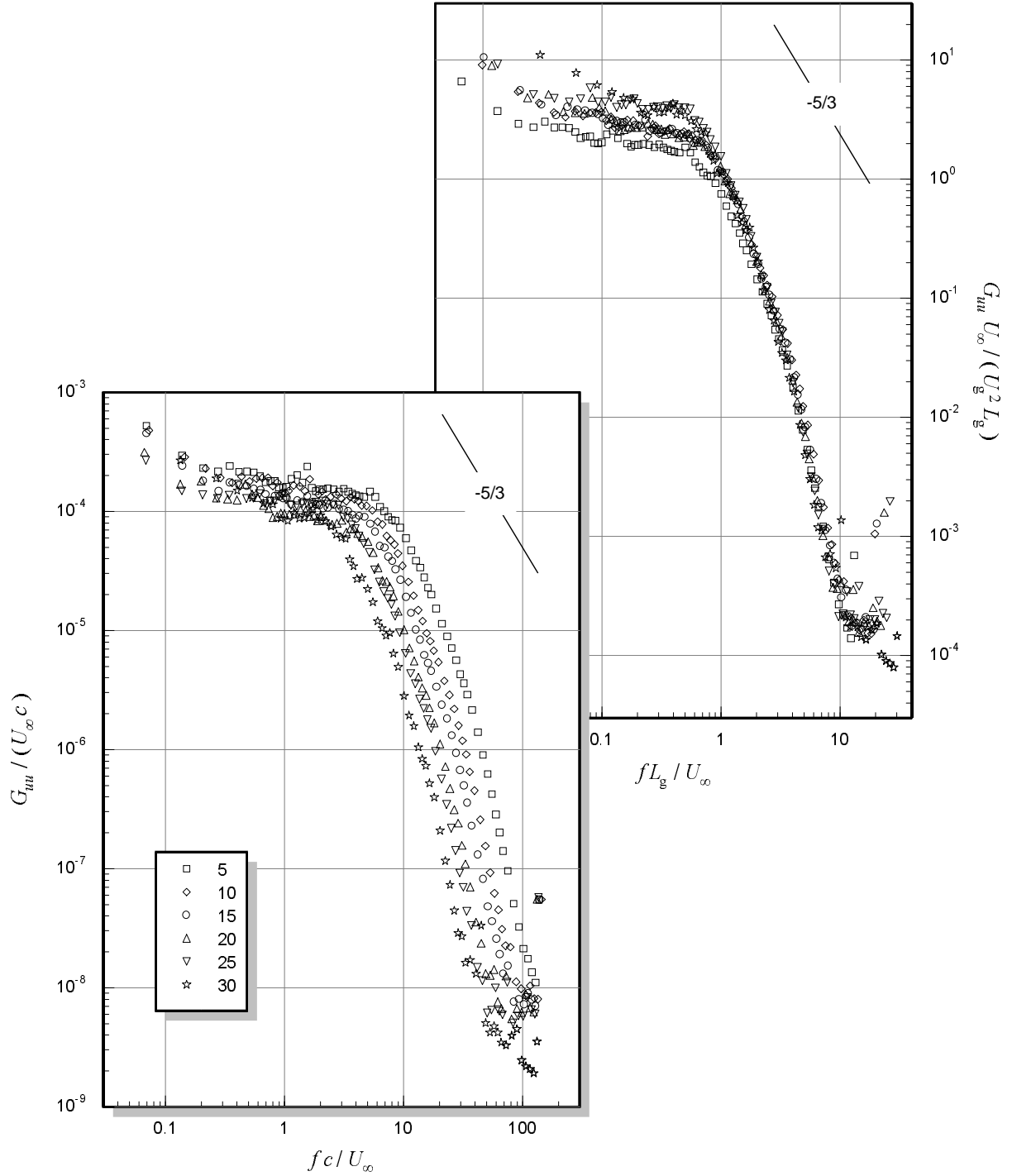
Figure 3.6: Core center axial velocity autospectra at various locations downstream of the vortex generator ($\alpha_1 = 5°$) with the interaction blade removed. Two normalizations shown: free-stream velocity and blade chord, and two-dimensional wake parameters. Numbers in legend are x/c locations. Data from Devenport *et al.* [43].
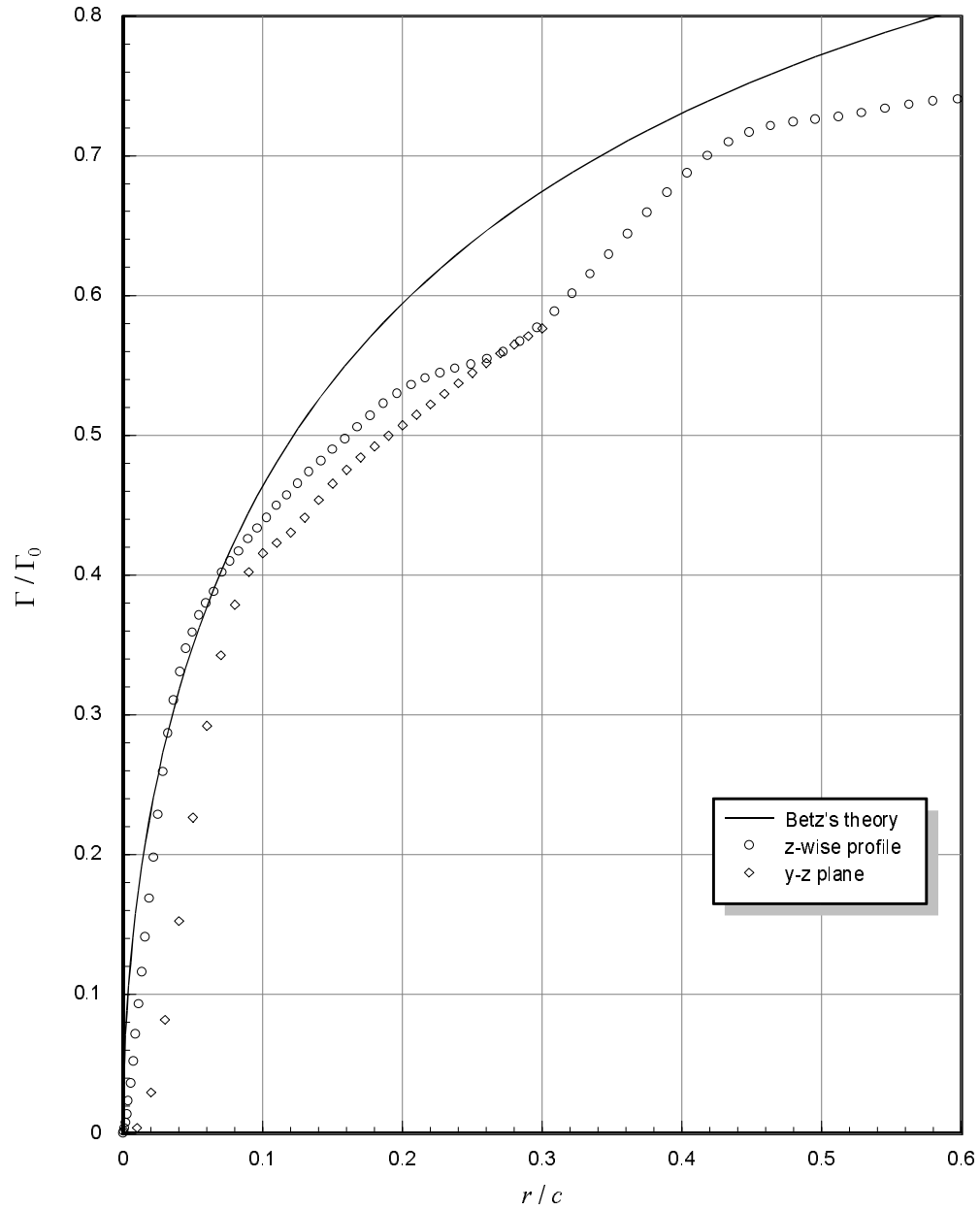
Figure 3.7: Circulation distributions at $x/c = 10$ estimated from z-wise profile and from y-z plane data compared with Betz's theory. $\alpha_1 = 5°$. Data from Devenport *et al.* [43].
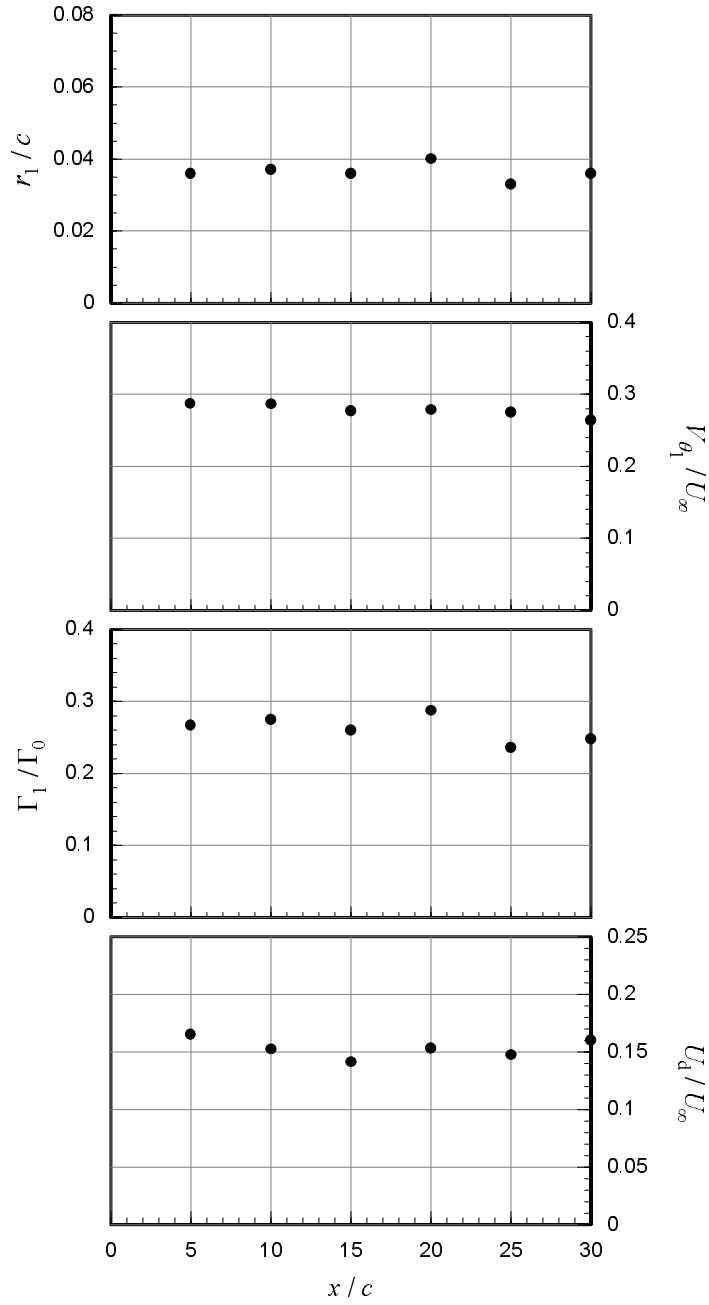
Figure 3.8: Core parameters (radius, peak tangential velocity, core circulation, and axial velocity deficit) as a function of downstream distance with interaction blade removed. $\alpha_1 = 5°$. Data from Devenport *et al.* [43].
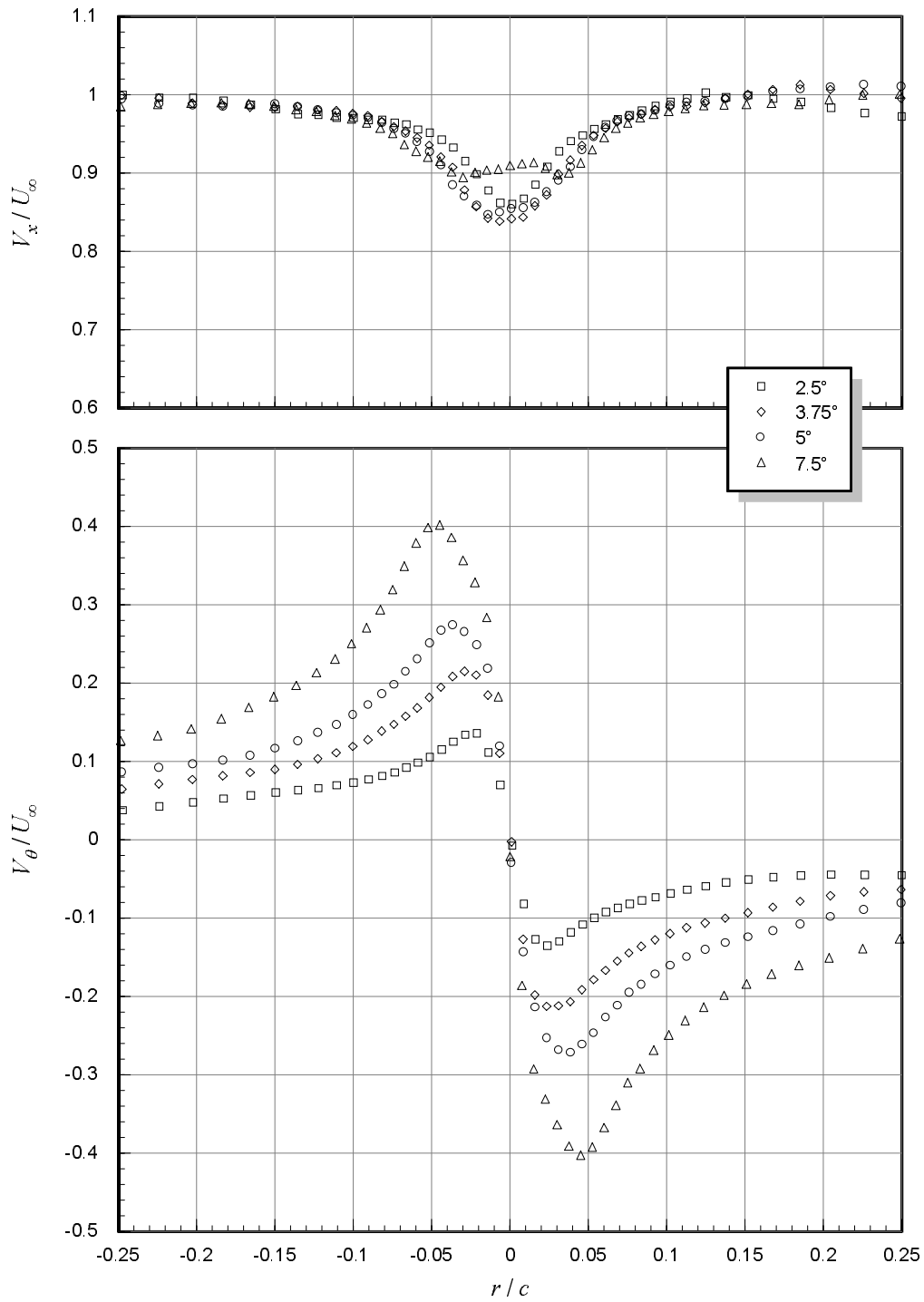
Figure 3.9: Mean axial and tangential velocities at $x/c = 10$ measured along z-wise profiles through the vortex core center for various generator angles of attack. Numbers in legend are α_1 values. Data from Devenport *et al.* [43].

63
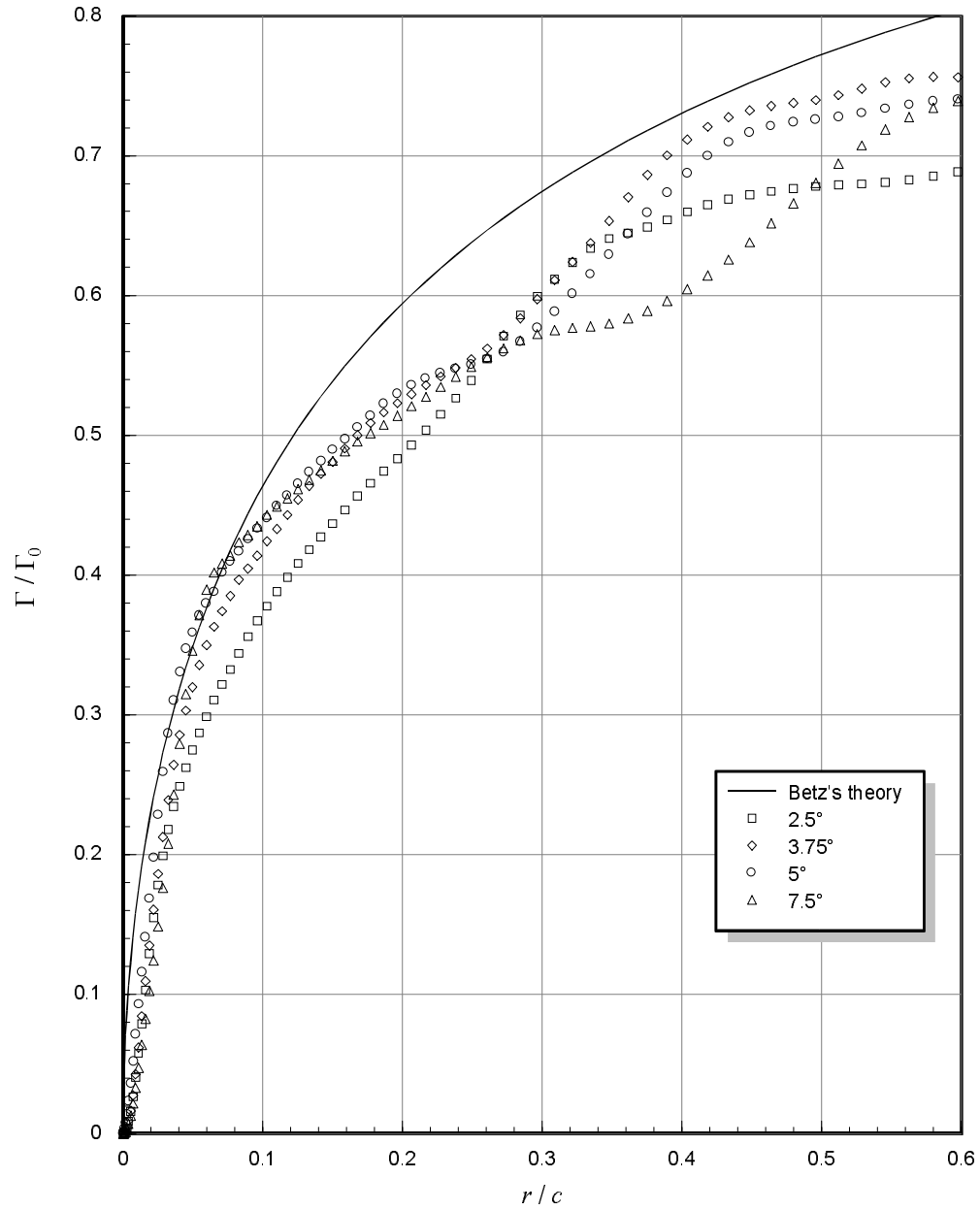
Figure 3.10: Circulation distributions at $x/c = 10$ estimated from z-wise profiles for various generator angles of attack. Numbers in legend are α_1 values. Data from Devenport *et al.* [43].
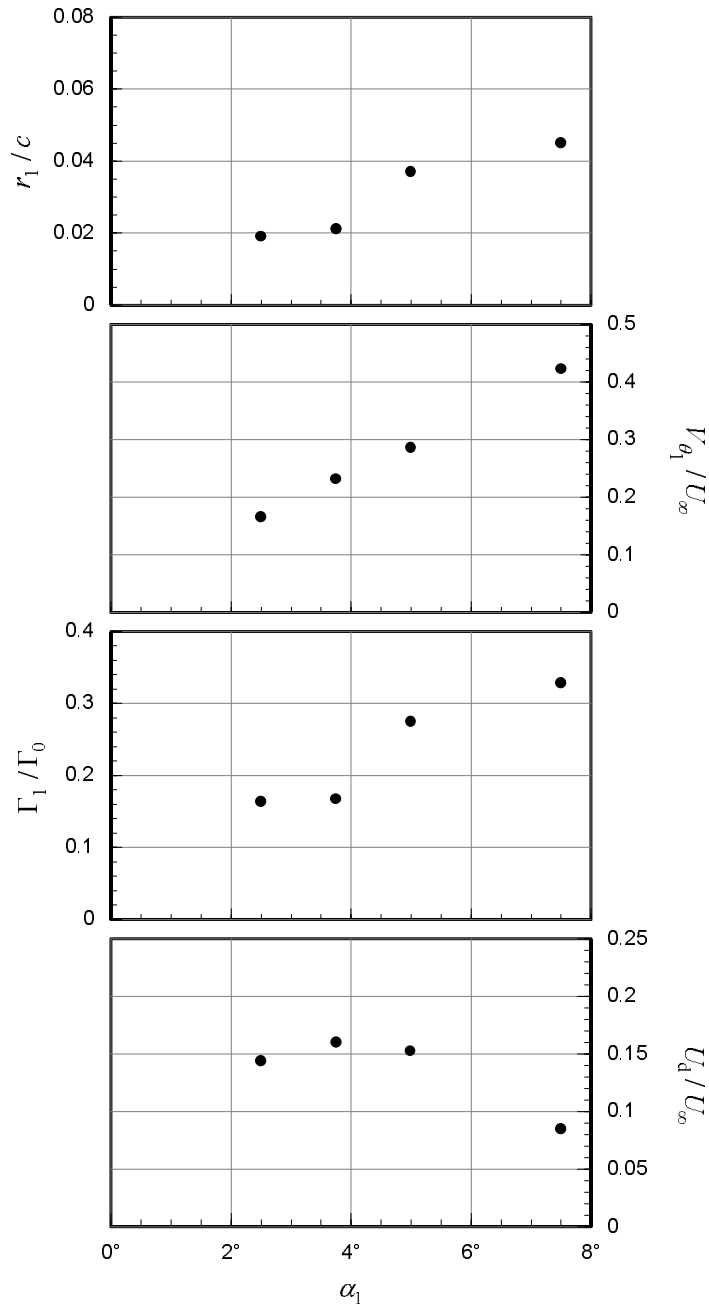
Figure 3.11: Core parameters (radius, peak tangential velocity, core circulation, and axial velocity deficit) at $x/c = 10$ as a function of generator angle of attack. Numbers in legend are α_1 values. Data from Devenport *et al.* [43].
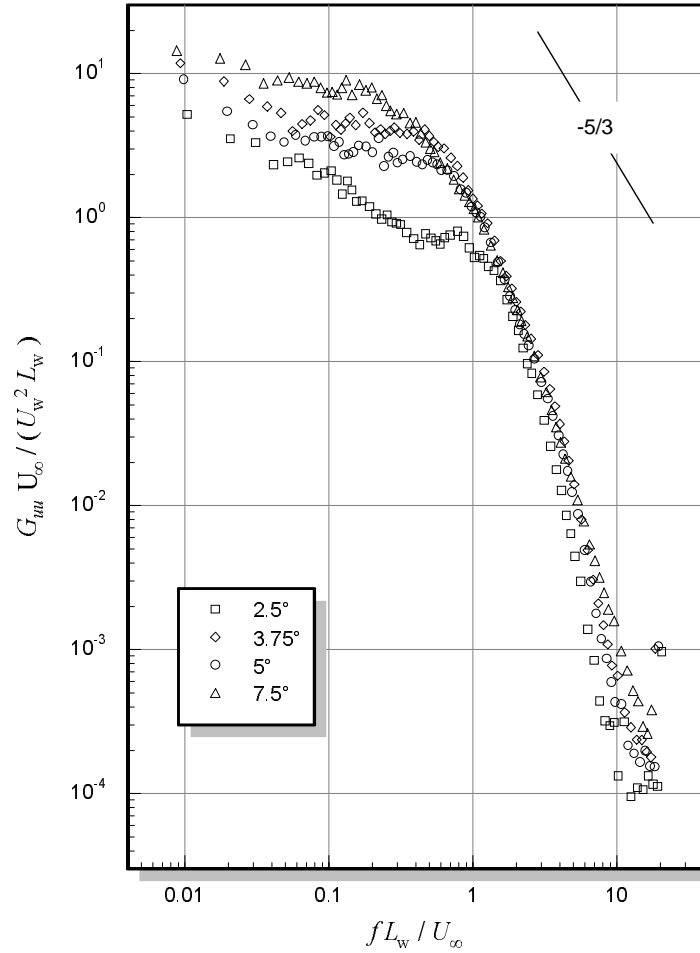
Figure 3.12: Core center axial velocity autospectra at $x/c = 10$ for various generator angles of attack. Numbers in legend are α_1 values. Data from Devenport *et al.* [43].

66
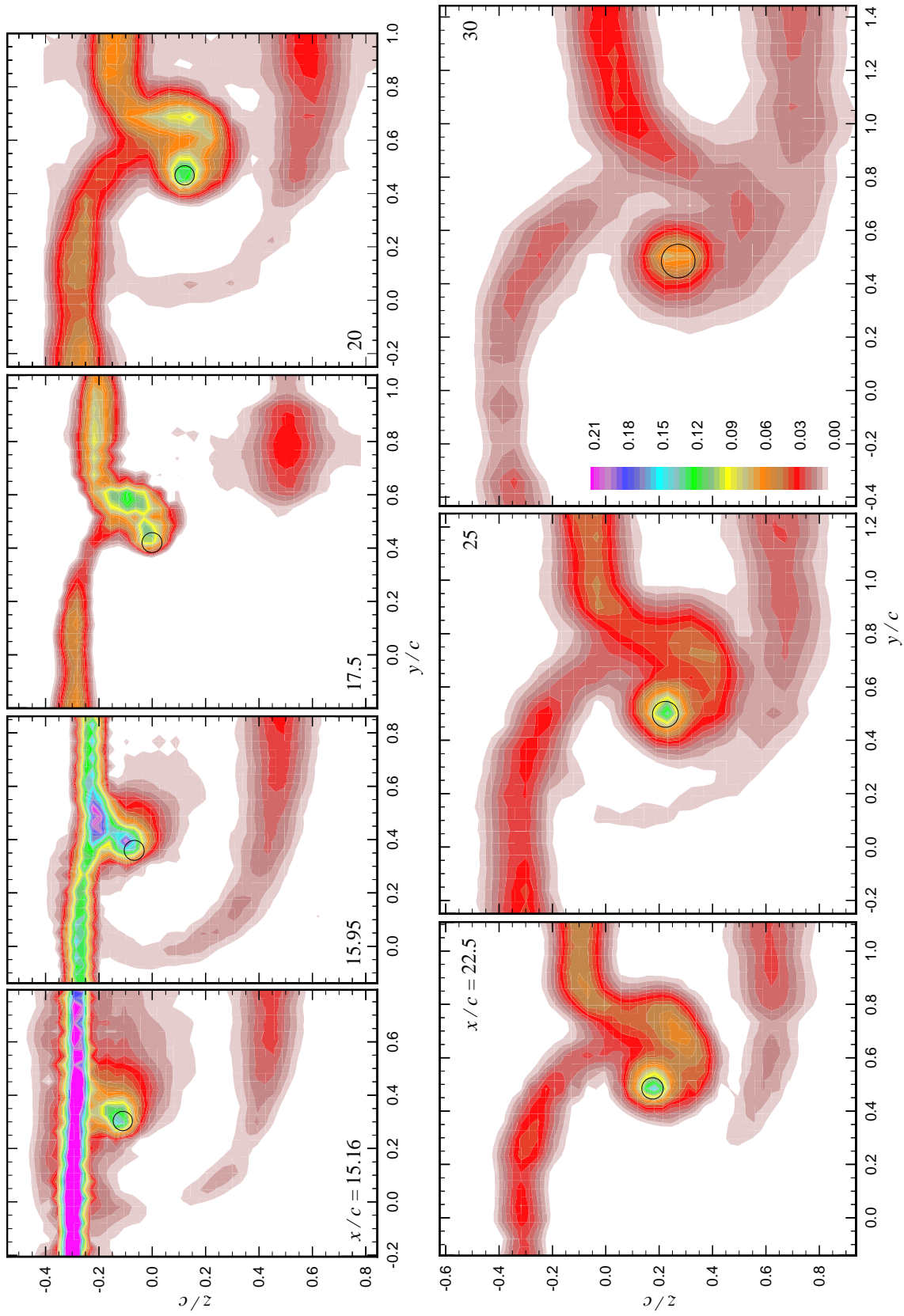
Figure 3.13: Contours of mean axial velocity deficit ($(1 - U)/U_\infty$) for pressure side passage of $\Delta/c = -0.125$. $\alpha_1 = \alpha_2 = 5°$. Core edge outlined by circle.
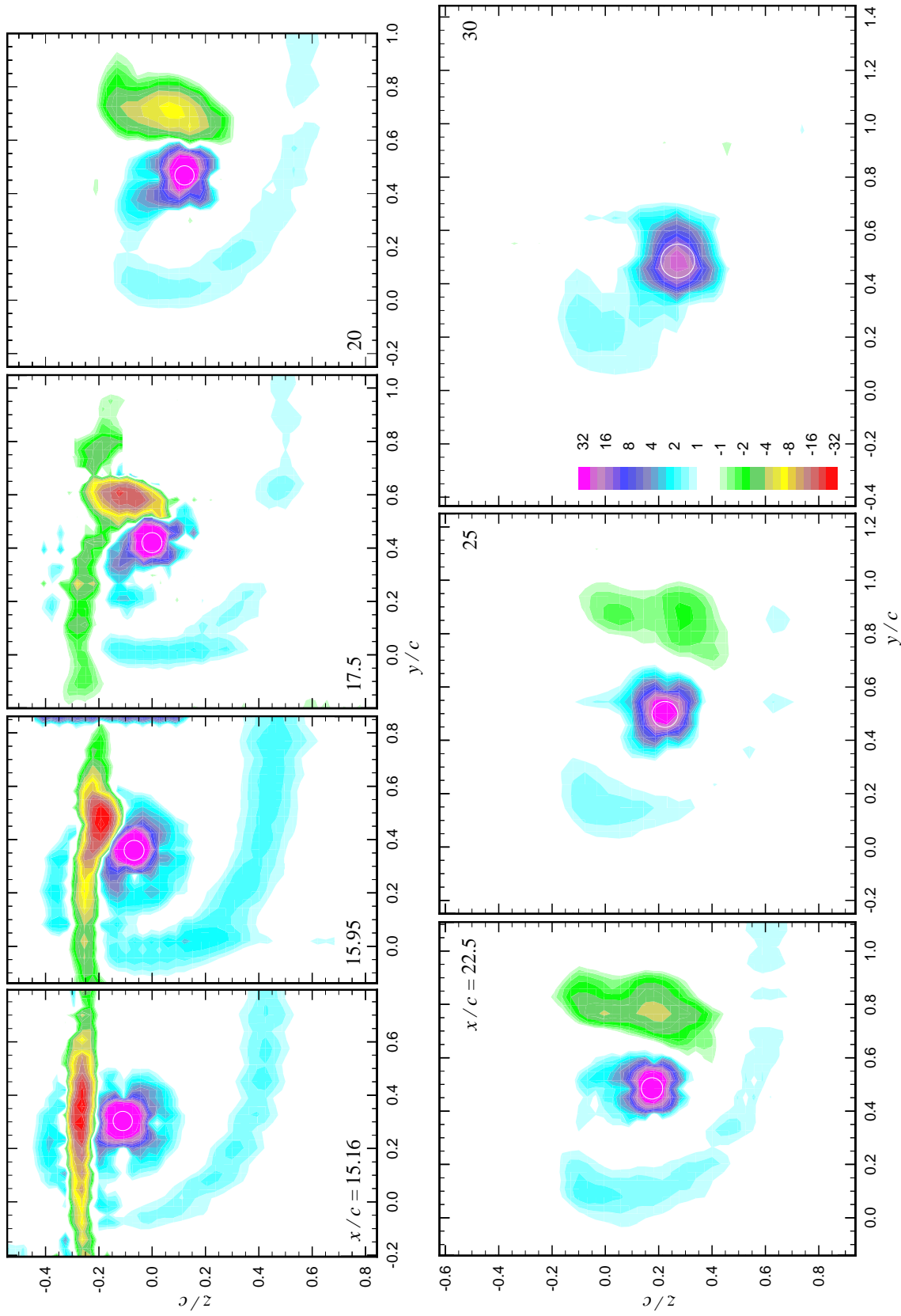
Figure 3.14: Contours of mean axial vorticity ($\Omega_x c/U_\infty \times 10$) for pressure side passage of $\Delta/c = -0.125$. $\alpha_1 = \alpha_2 = 5°$. Core edge outlined by circle.
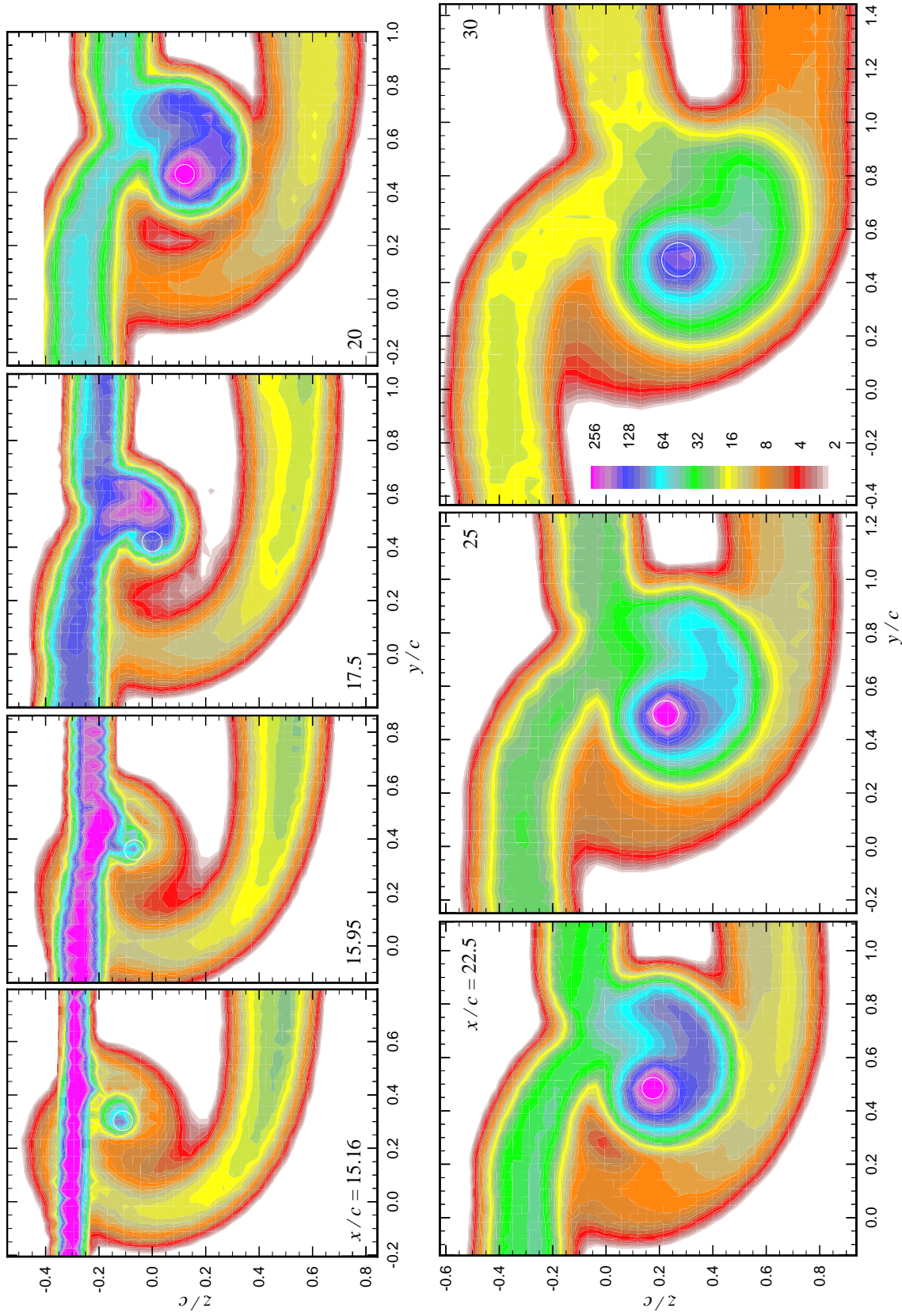
Figure 3.15: Contours of axial normal turbulent stress ($\overline{u^2}/U_8^2 \times 10^5$) for pressure side passage of $\Delta/c = -0.125$. $\alpha_1 = \alpha_2 = 5°$. Core edge outlined by circle.
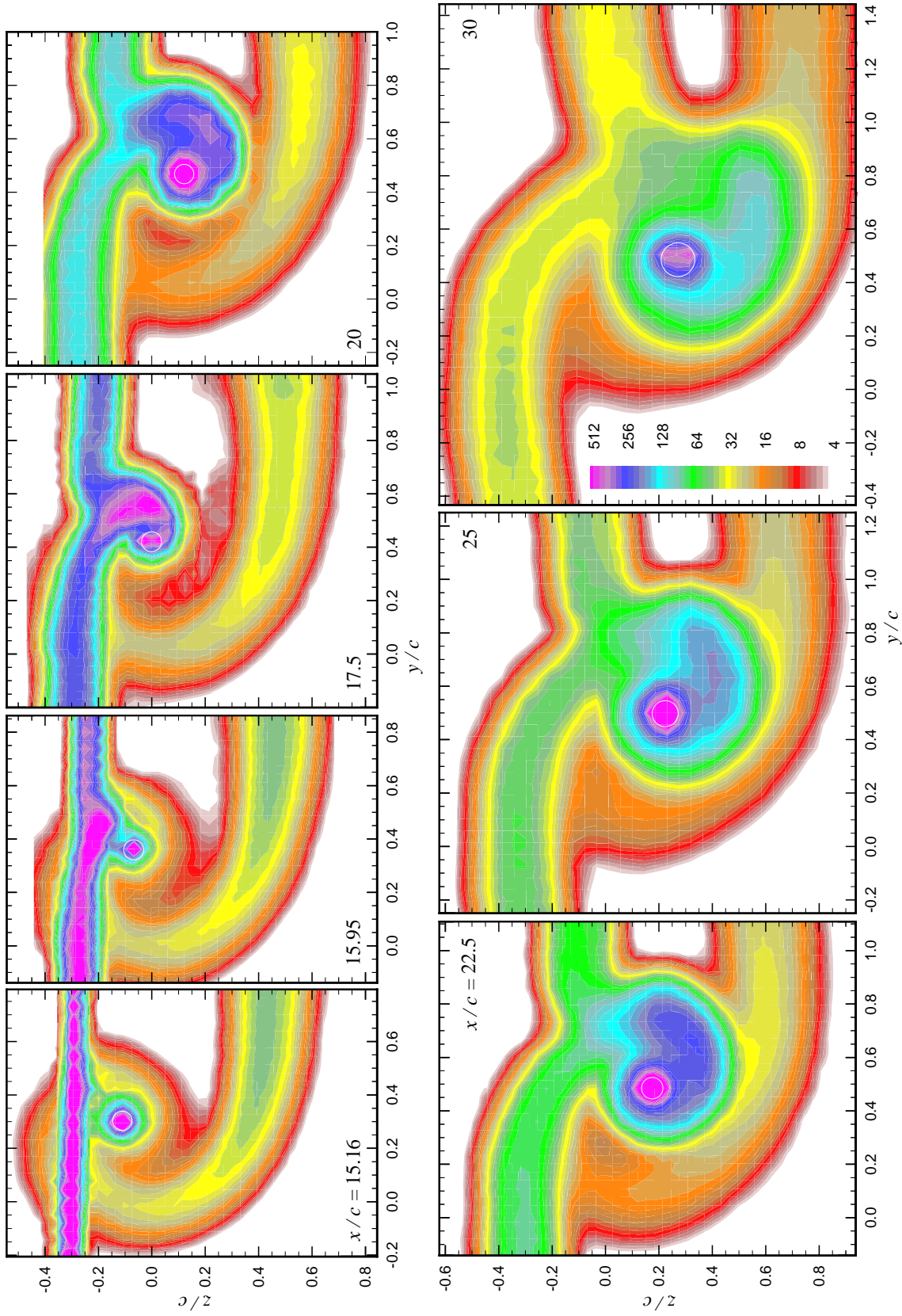
Figure 3.16: Contours of summed cross-flow normal turbulent stresses $((\overline{v^2} + \overline{w^2})/U_8^2 \times 10^5)$ for pressure side passage of $\Delta/c = -0.125$. $\alpha_1 = \alpha_2 = 5°$. Core edge outlined by circle.
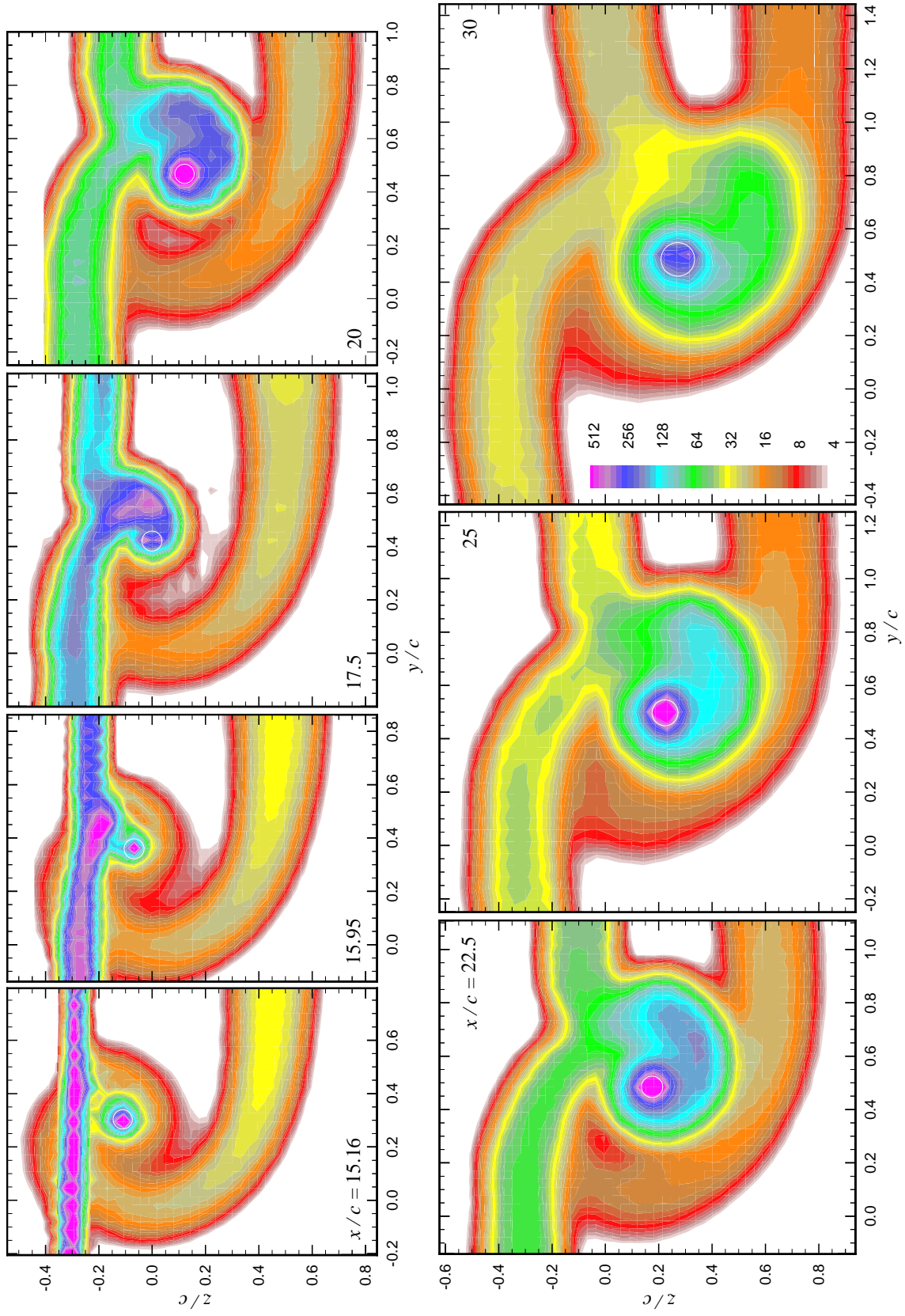
Figure 3.17: Contours of turbulence kinetic energy ($k/U_\infty^2 \times 10^5$) for pressure side passage of $\Delta/c = -0.125$. $\alpha_1 = \alpha_2 = 5°$. Core edge outlined by circle.
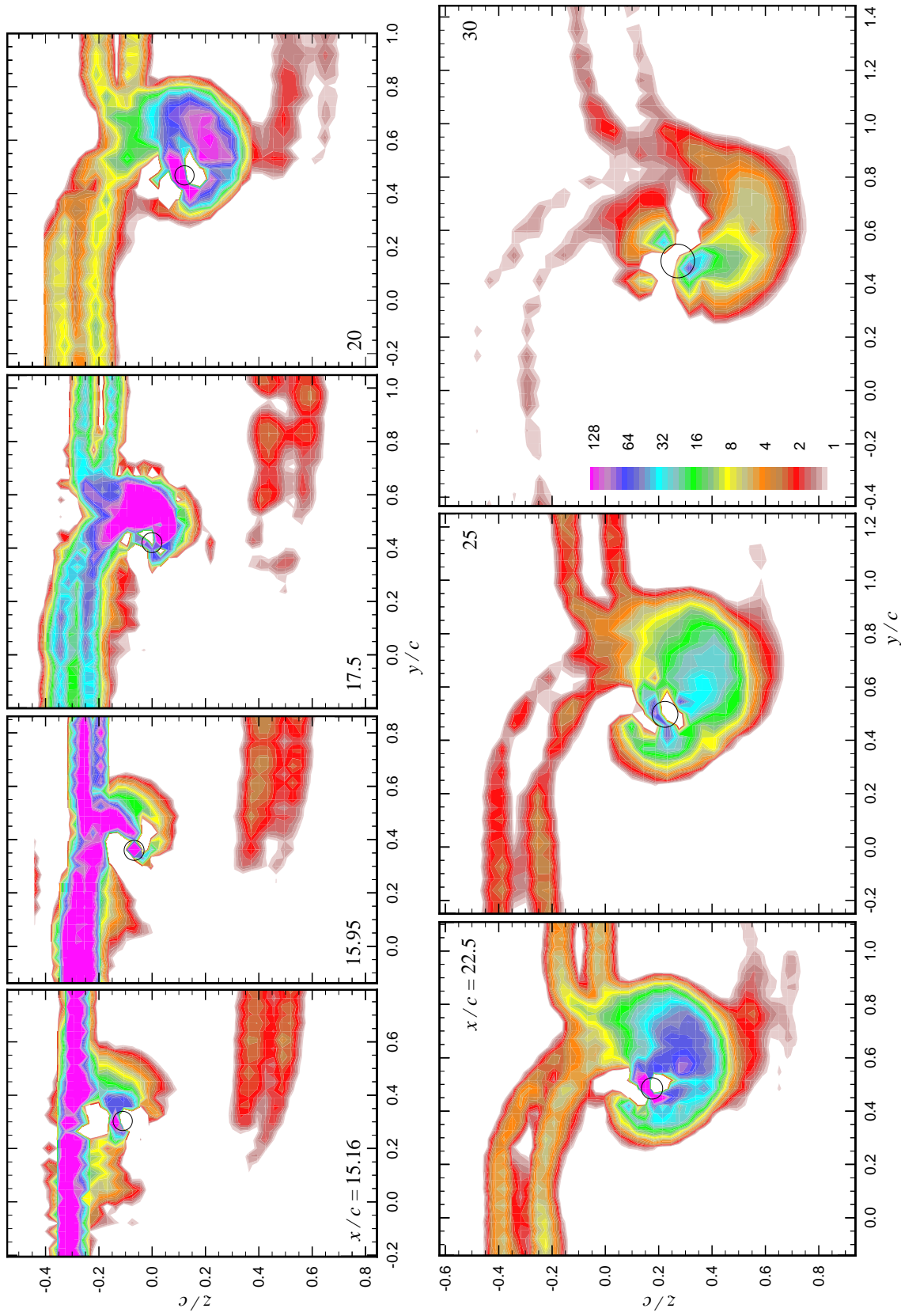
Figure 3.18: Contours of turbulence kinetic energy production ($Pc/U_\infty^3 \times 10^5$) for pressure side passage of $\Delta/c = -0.125$. $\alpha_1 = \alpha_2 = 5°$. Core edge outlined by circle.
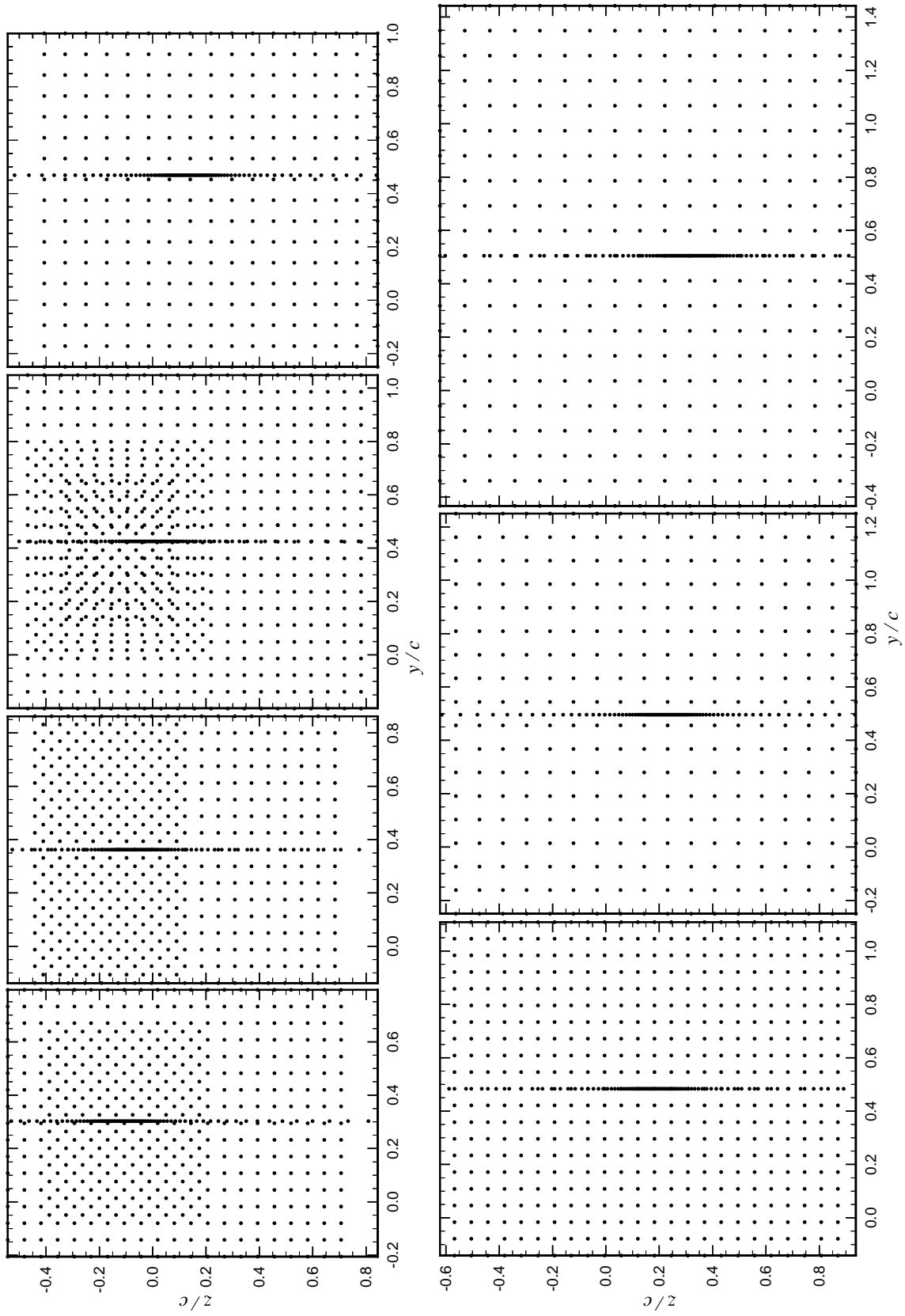
Figure 3.19: Scatter plots of the measurement locations used to determine contours for pressure side passage of $\Delta/c = -0.125$. $\alpha_1 = \alpha_2 = 5°$.

73
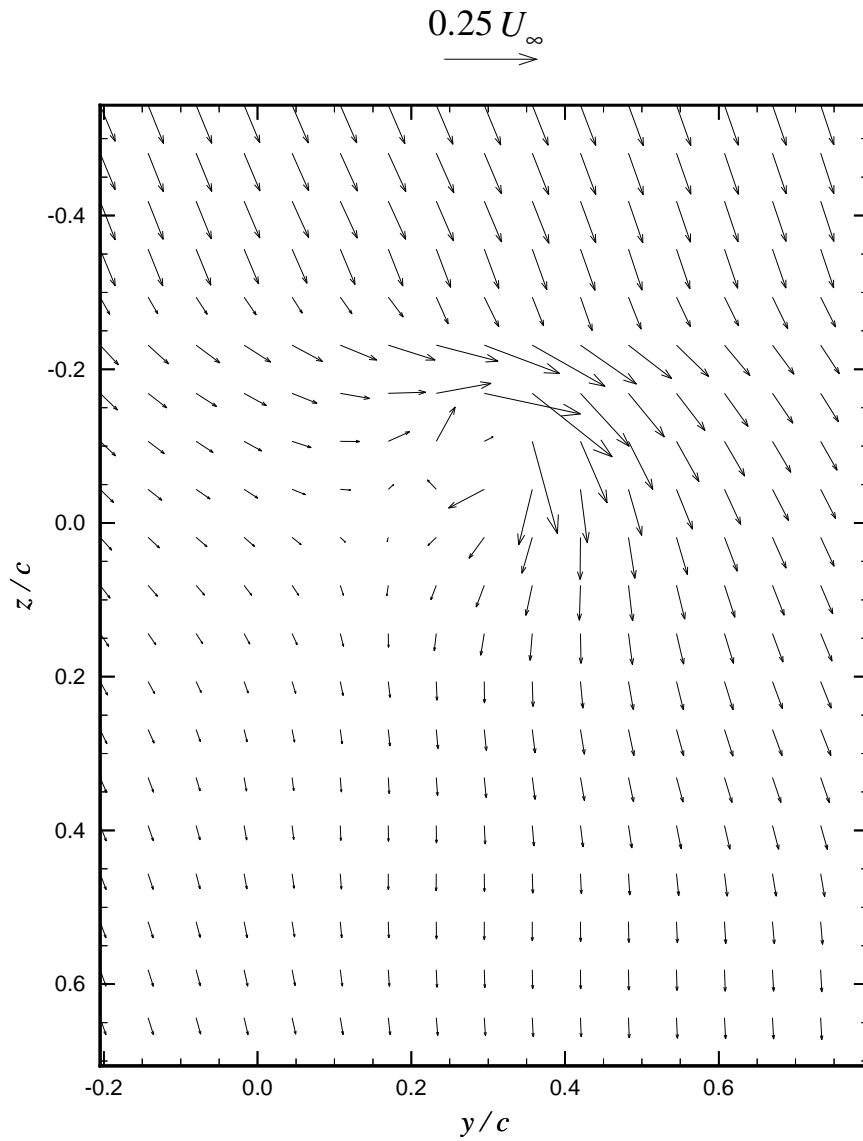
Figure 3.20: Mean cross flow velocity vectors $(V\hat{\imath} + W\hat{\jmath})$ at $x/c = 15.16$ for pressure side passage of $\Delta/c = -0.125$. $\alpha_1 = \alpha_2 = 5°$.
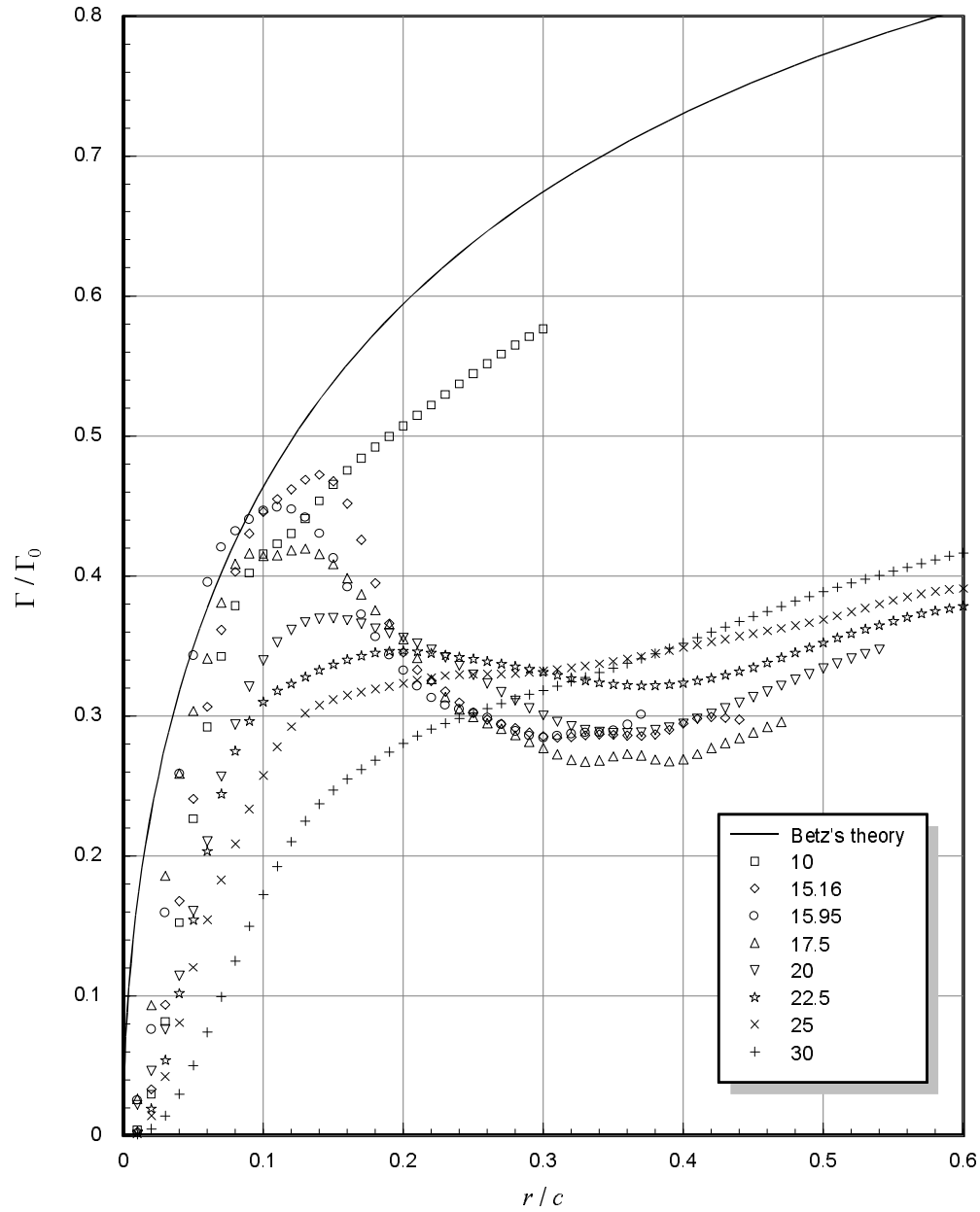
Figure 3.21: Circulation distributions at various locations downstream of a pressure side passage of $\Delta/c = -0.125$ estimated from y-z plane data. $\alpha_1 = \alpha_2 = 5°$. Numbers in legend are x/c locations.
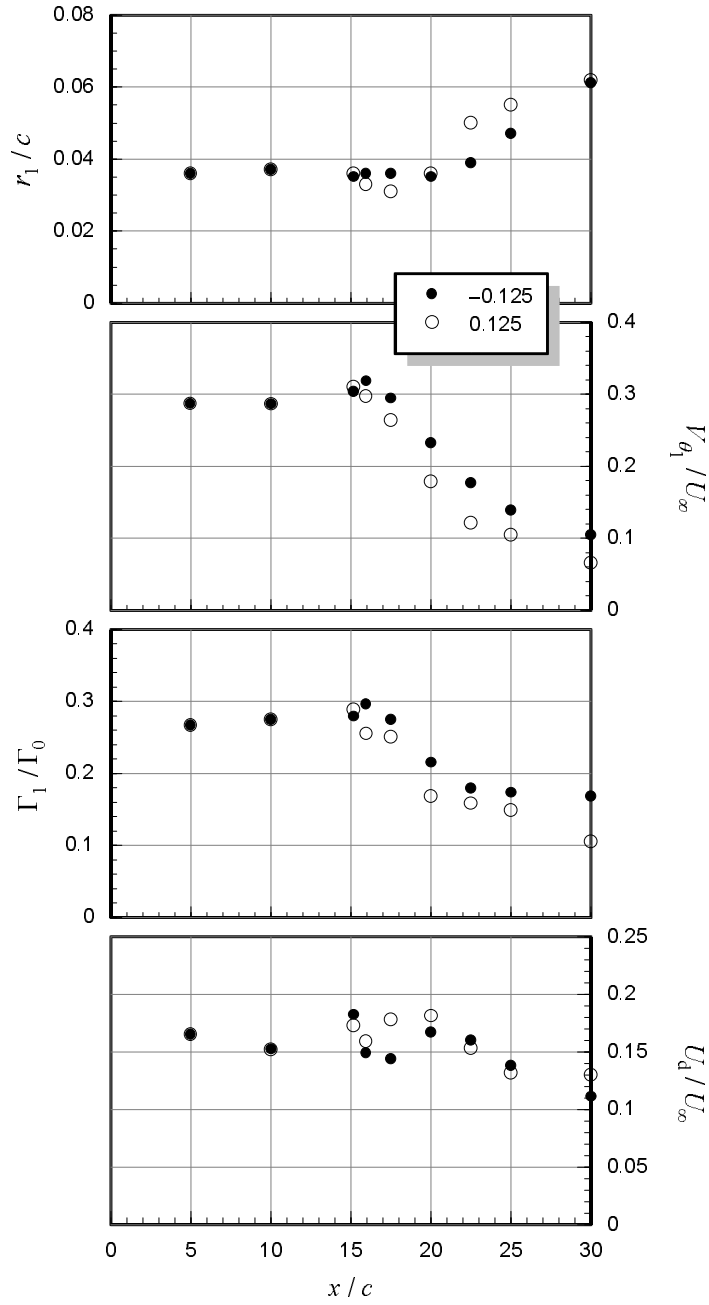
Figure 3.22: Core parameters (radius, peak tangential velocity, core circulation, and axial velocity deficit) as a function of downstream distance for pressure and suction side passages of $|\Delta/c| = 0.125$. $\alpha_1 = \alpha_2 = 5°$. Numbers in legend are Δ/c values.
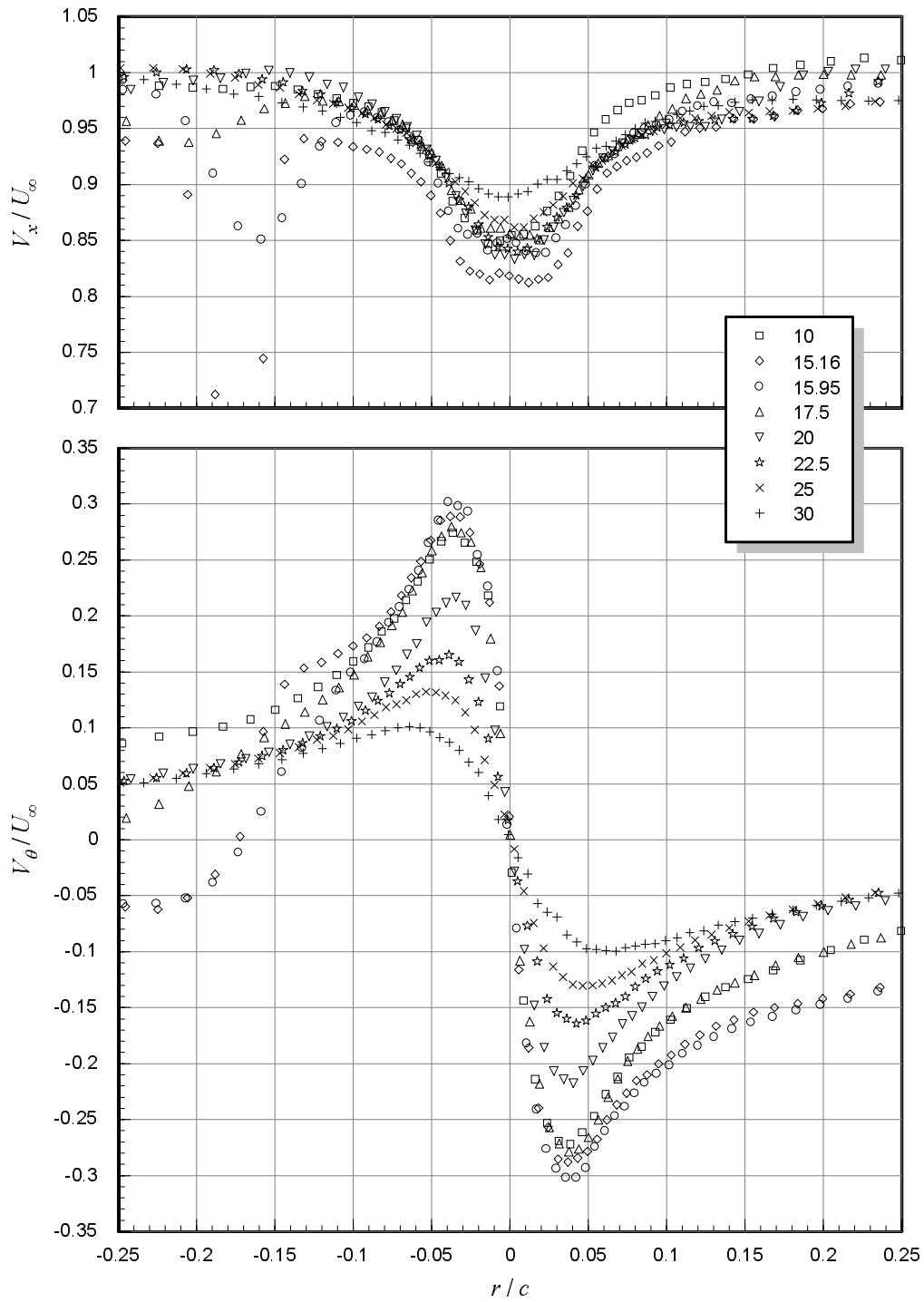
Figure 3.23: Mean axial and tangential velocities measured along z-wise profiles through the core center at various locations downstream of a pressure side passage of $\Delta/c = -0.125$. $\alpha_1 = \alpha_2 = 5°$. Numbers in legend are x/c locations.
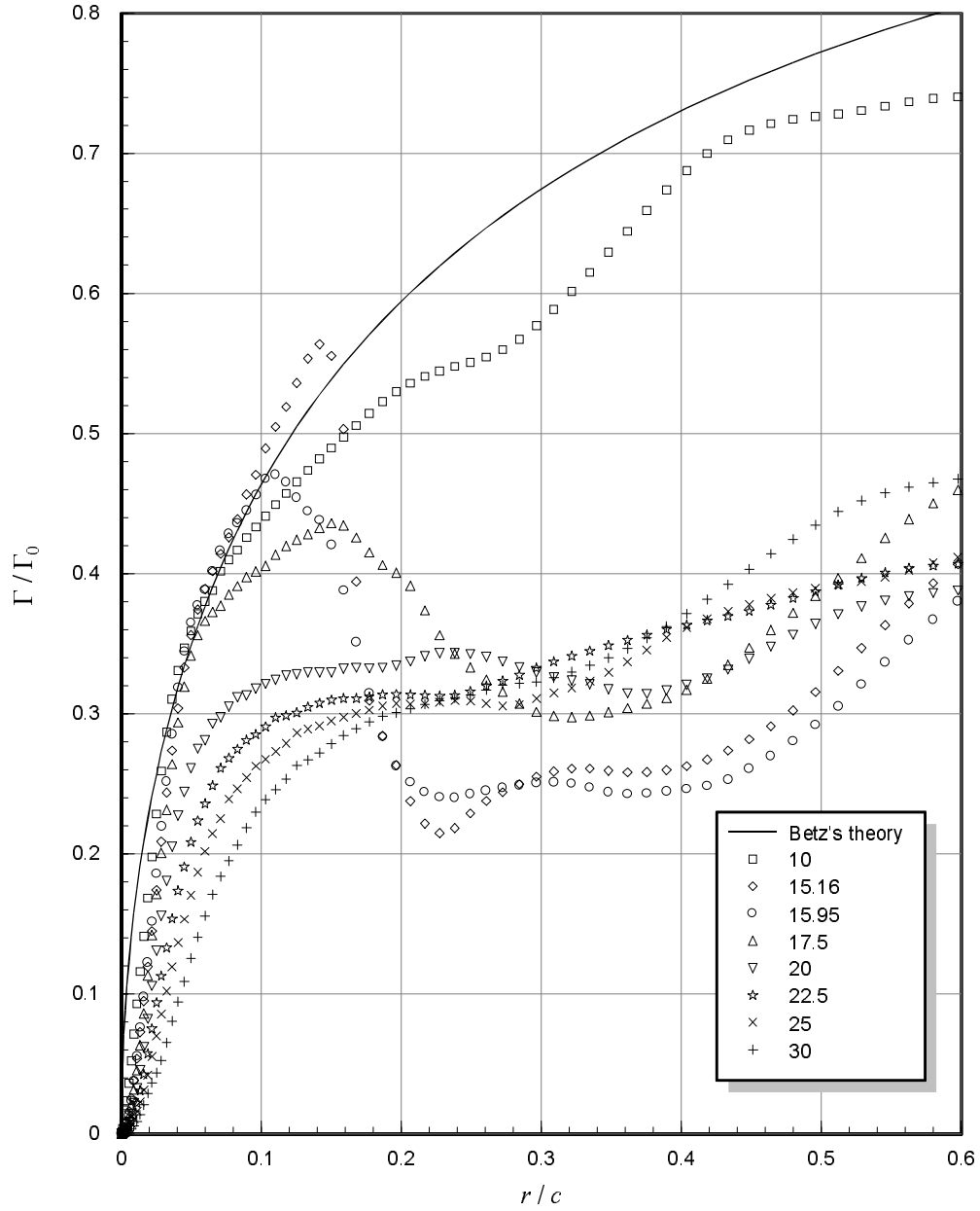
Figure 3.24: Circulation distributions estimated from z-wise profiles through the core center at various locations downstream of a pressure side passage of $\Delta/c = -0.125$. $\alpha_1 = \alpha_2 = 5°$. Numbers in legend are x/c locations.
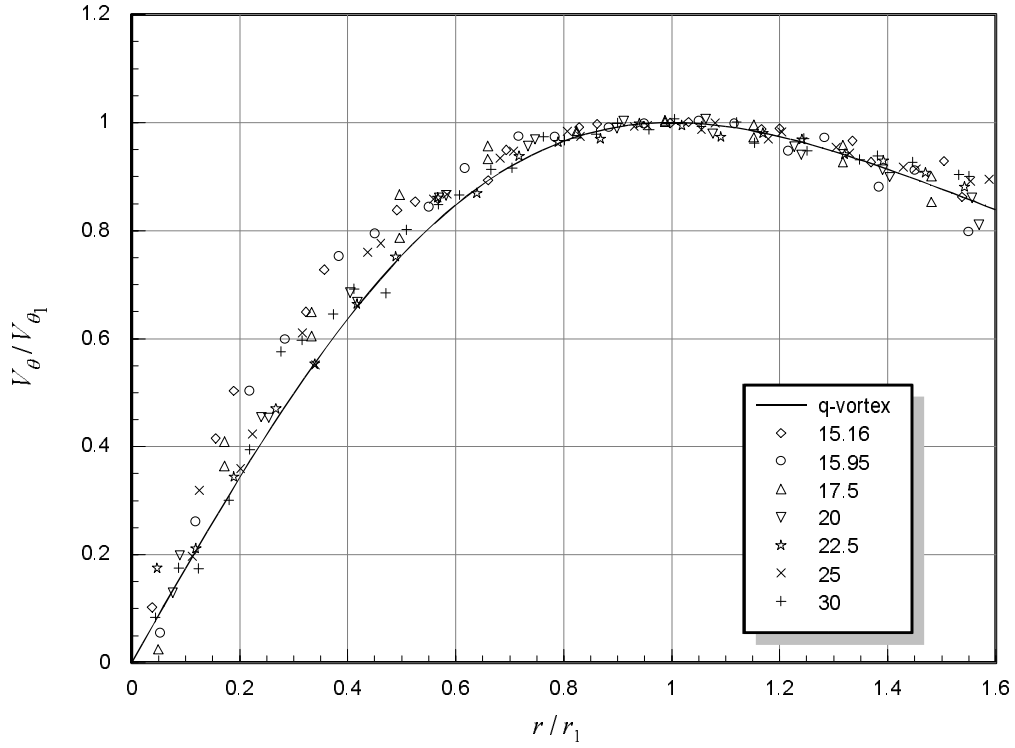
Figure 3.25: Tangential velocities from z-wise profiles through the core center normalized on measured core radius and peak tangential velocity at various locations downstream of a pressure side passage of $\Delta/c = -0.125$. $\alpha_1 = \alpha_2 = 5°$. Numbers in legend are x/c locations.
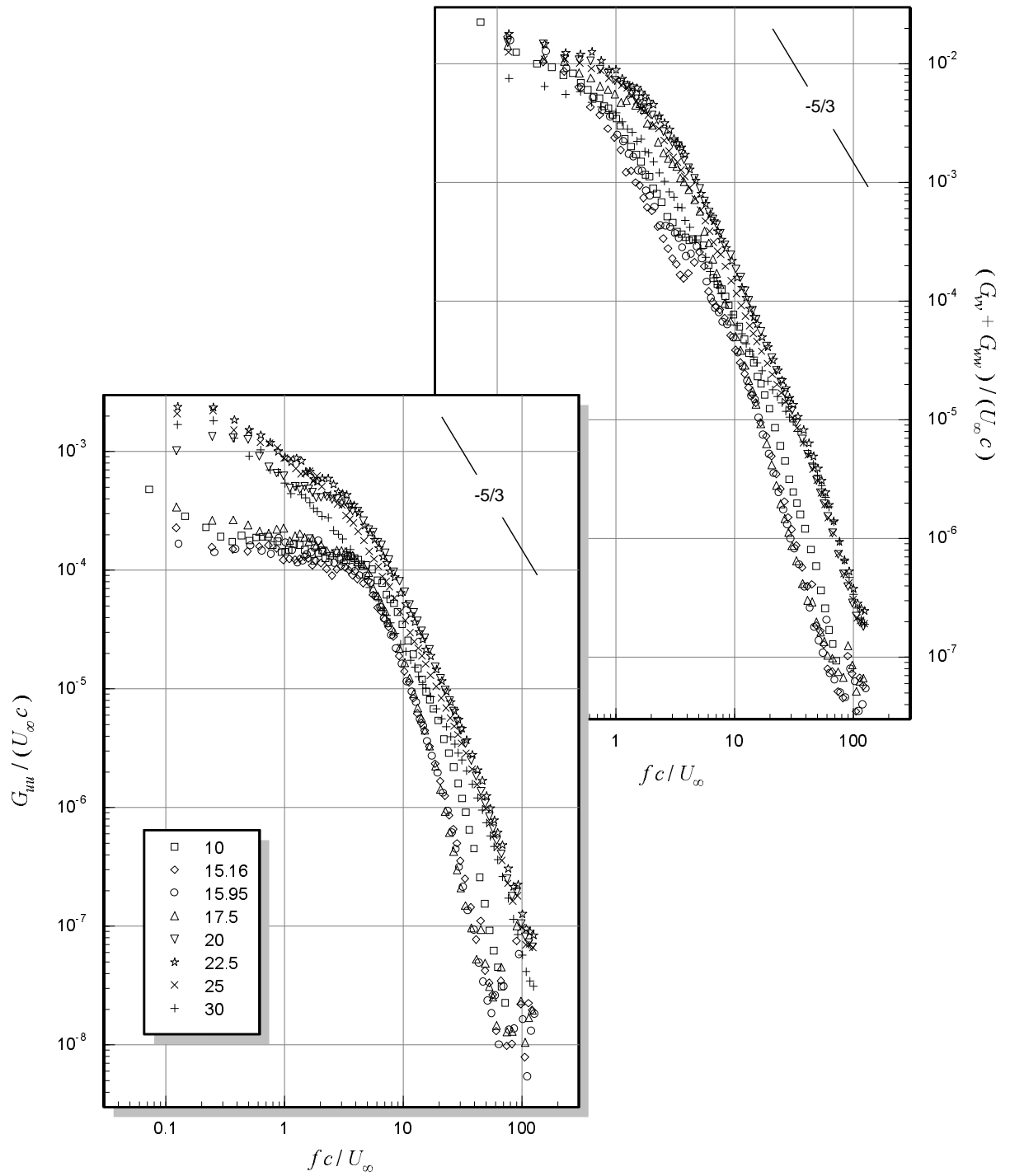
Figure 3.26: Core center velocity autospectra at various locations downstream of a pressure side passage of $\Delta/c = -0.125$. $\alpha_1 = \alpha_2 = 5°$. Numbers in legend are x/c locations.
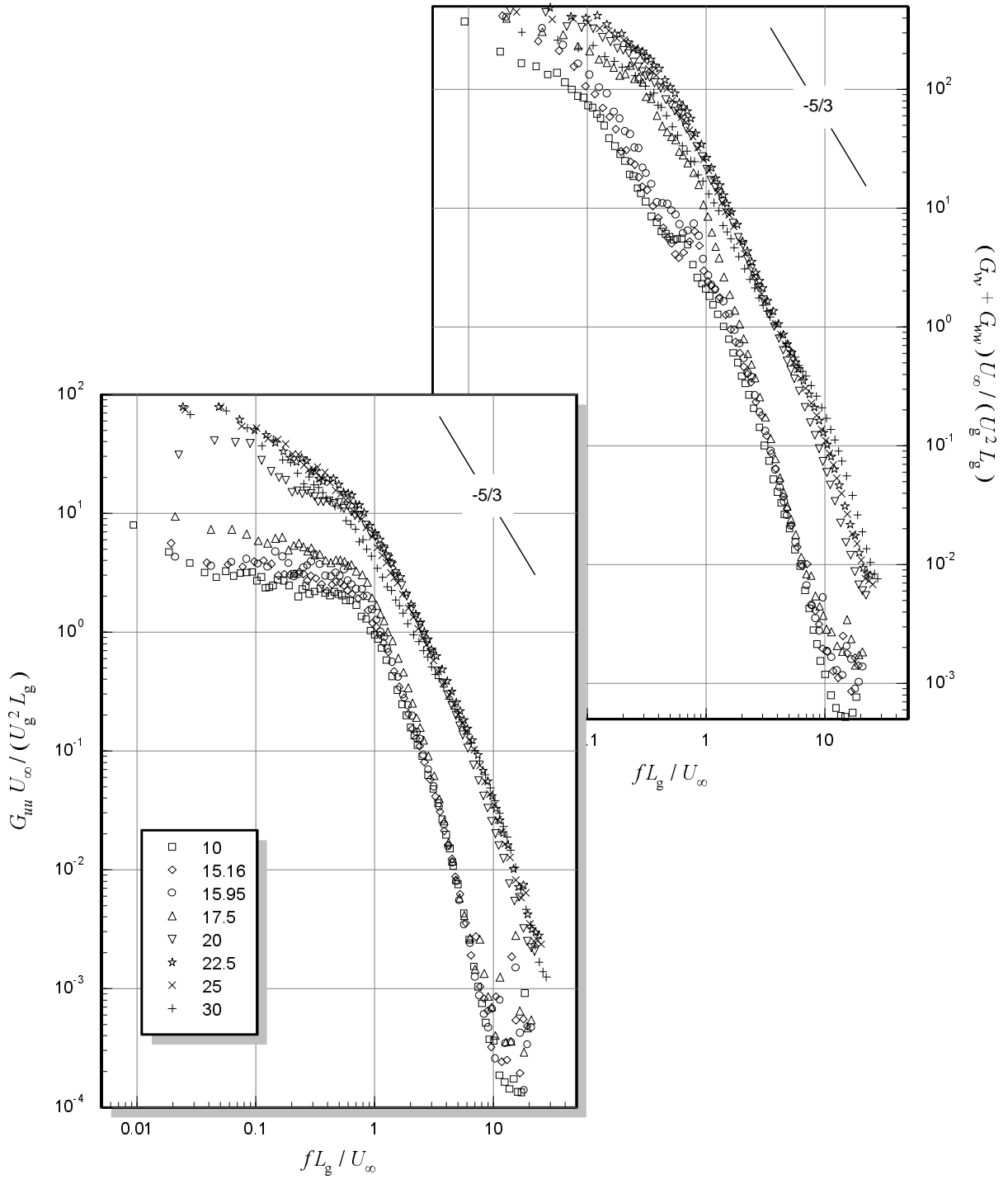
Figure 3.27: Core center velocity autospectra normalized on vortex generator wake scales at various locations downstream of a pressure side passage of $\Delta/c = -0.125$. $\alpha_1 = \alpha_2 = 5°$. Numbers in legend are x/c locations.
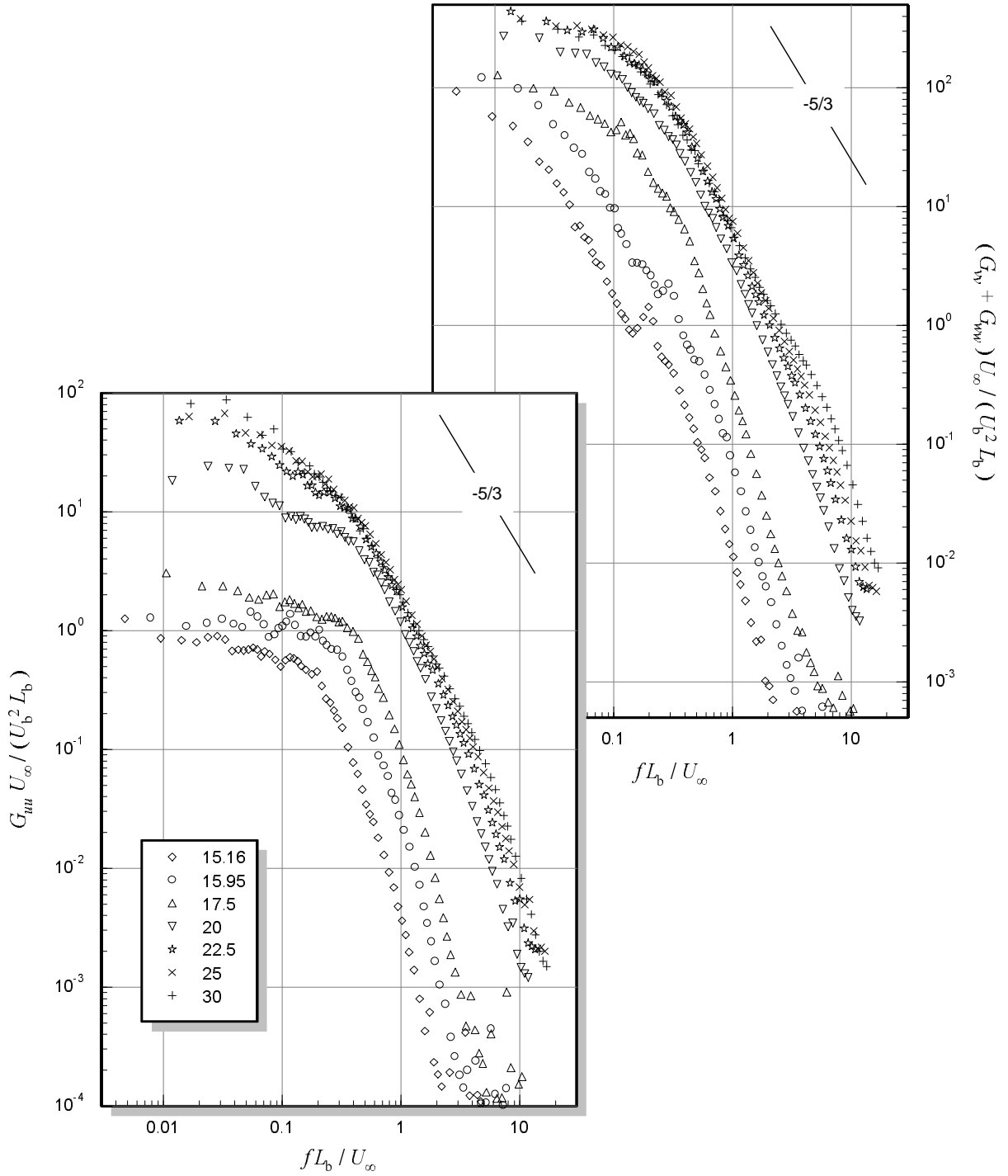
Figure 3.28: Core center velocity autospectra normalized on undistorted interaction blade wake scales at various locations downstream of a pressure side passage of $\Delta/c = -0.125$. $\alpha_1 = \alpha_2 = 5°$. Numbers in legend are x/c locations.
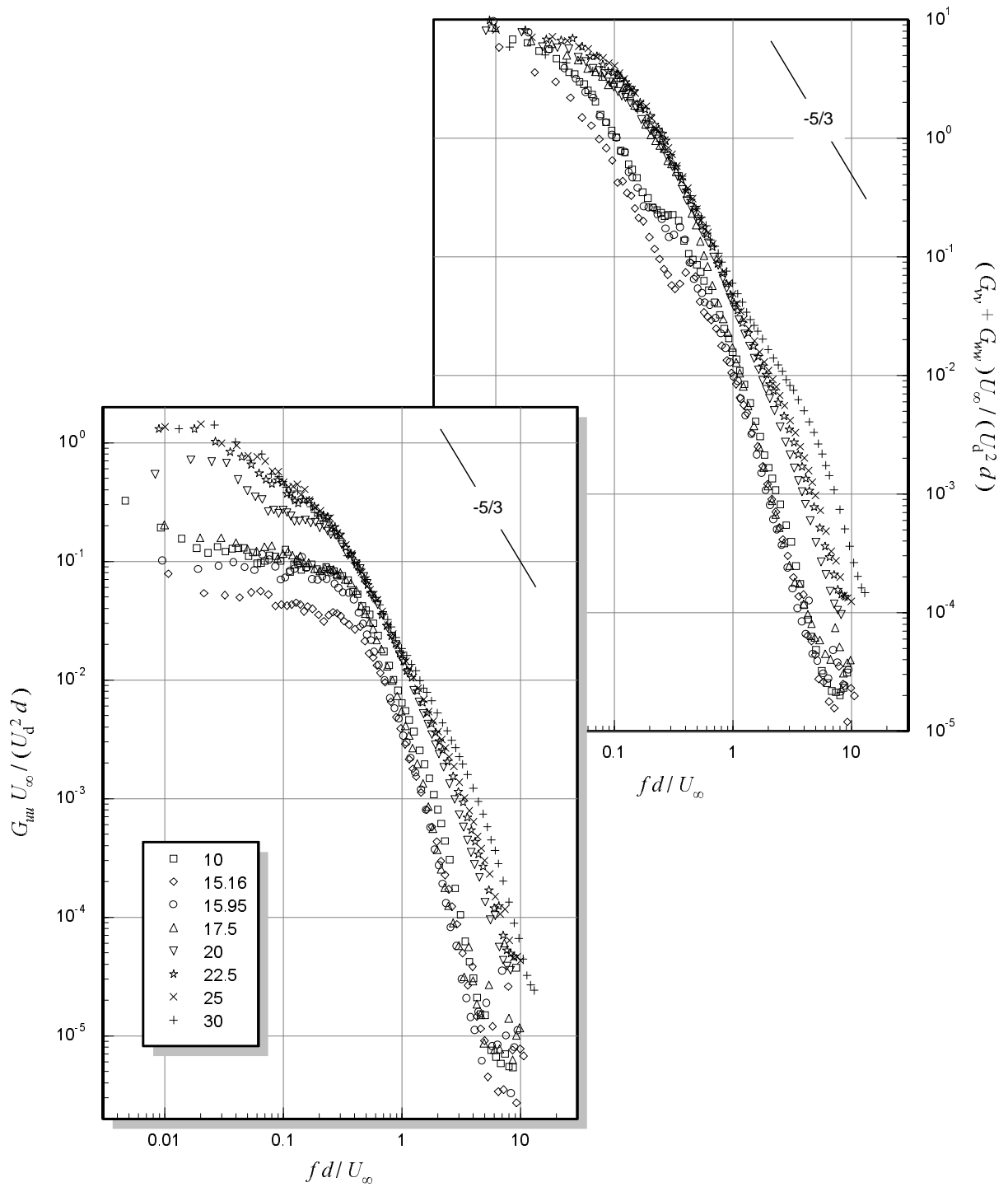
Figure 3.29: Core center velocity autospectra normalized on core centerline axial velocity deficit and radial scale of the deficit profile at various locations downstream of a pressure side passage of $\Delta/c = -0.125$. $\alpha_1 = \alpha_2 = 5°$. Numbers in legend are x/c locations.
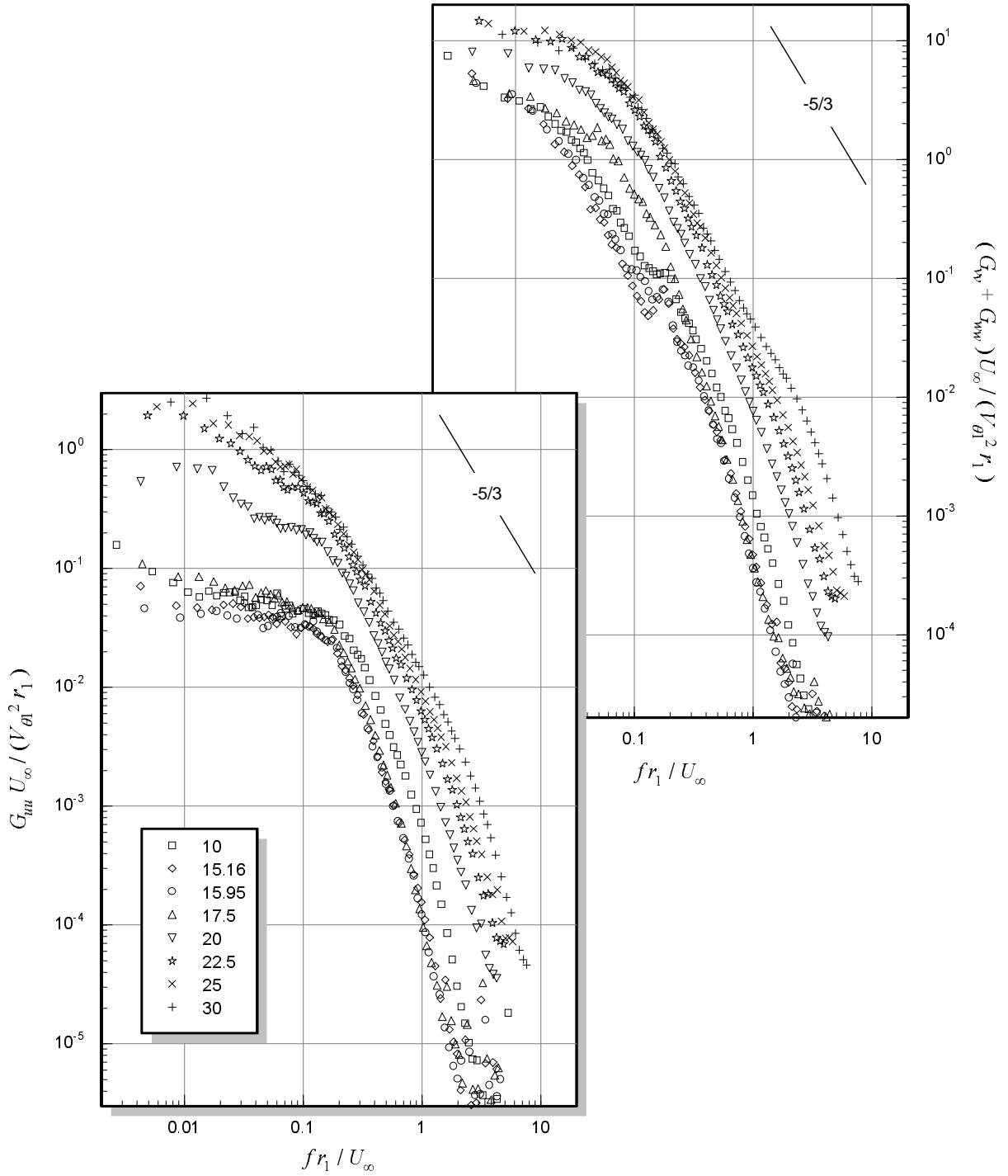
Figure 3.30: Core center velocity autospectra normalized on peak tangential velocity and core radius at various locations downstream of a pressure side passage of $\Delta/c = -0.125$. $\alpha_1 = \alpha_2 = 5°$. Numbers in legend are x/c locations.
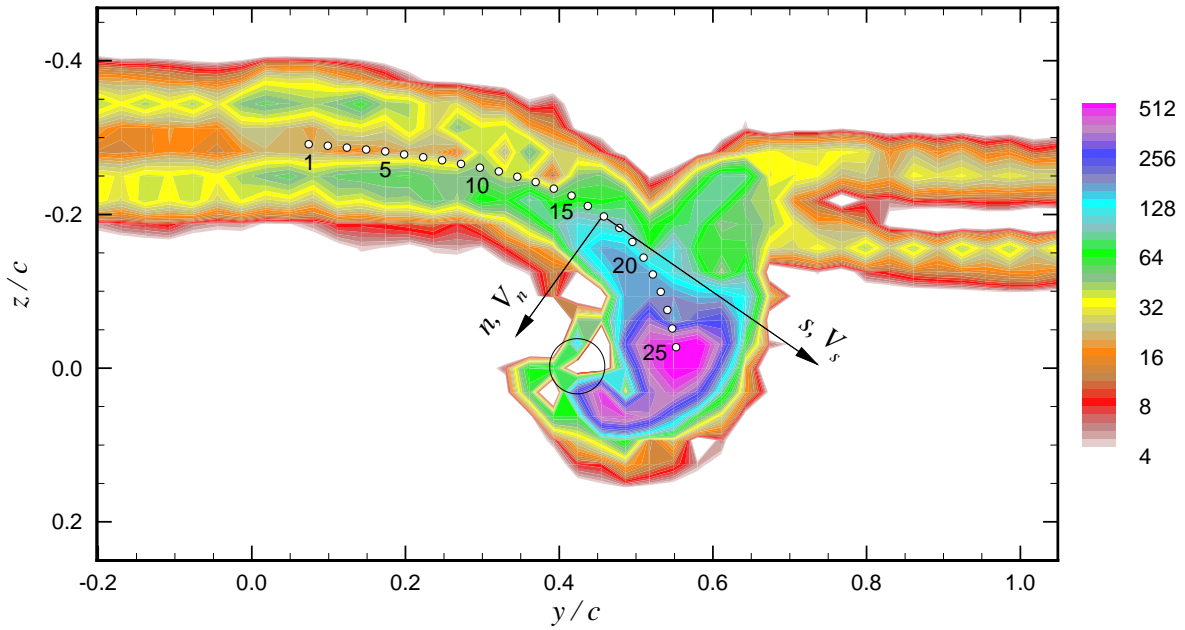
(a) $Pc/U_\infty^3 \times 10^5$
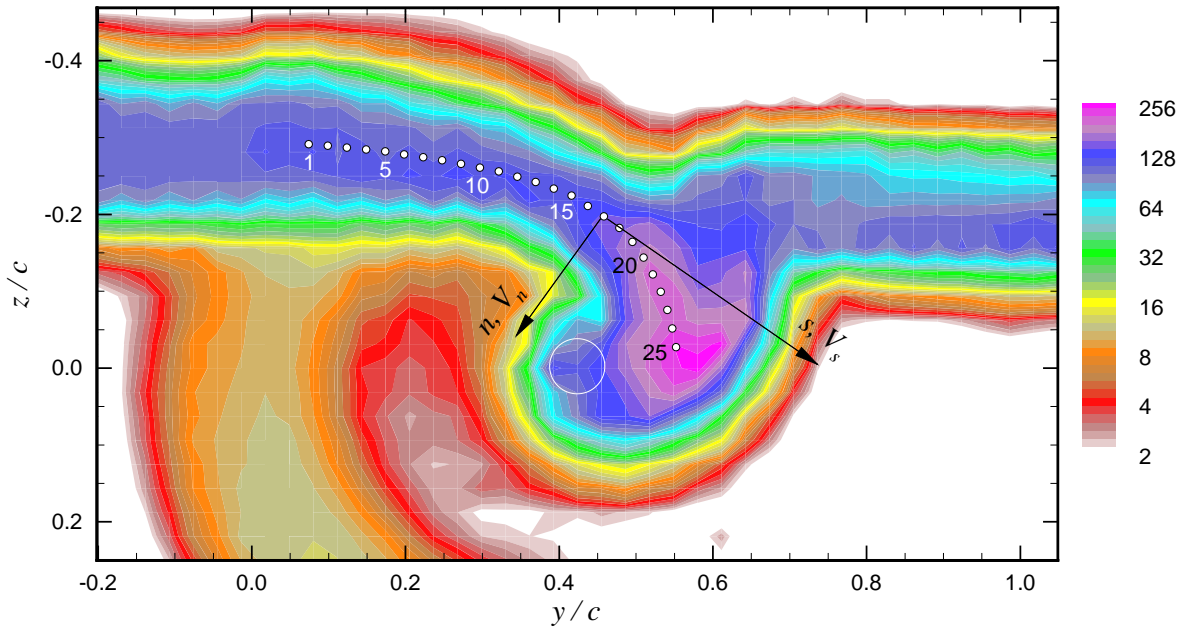
(b) $\overline{u^2}/U_\infty^2 \times 10^5$

Figure 3.31: Contours of: **(a)** turbulence kinetic energy production and **(b)** axial normal stress at $x/c = 17.5$. $\Delta/c = -0.125$, $\alpha_1 = \alpha_2 = 5°$.
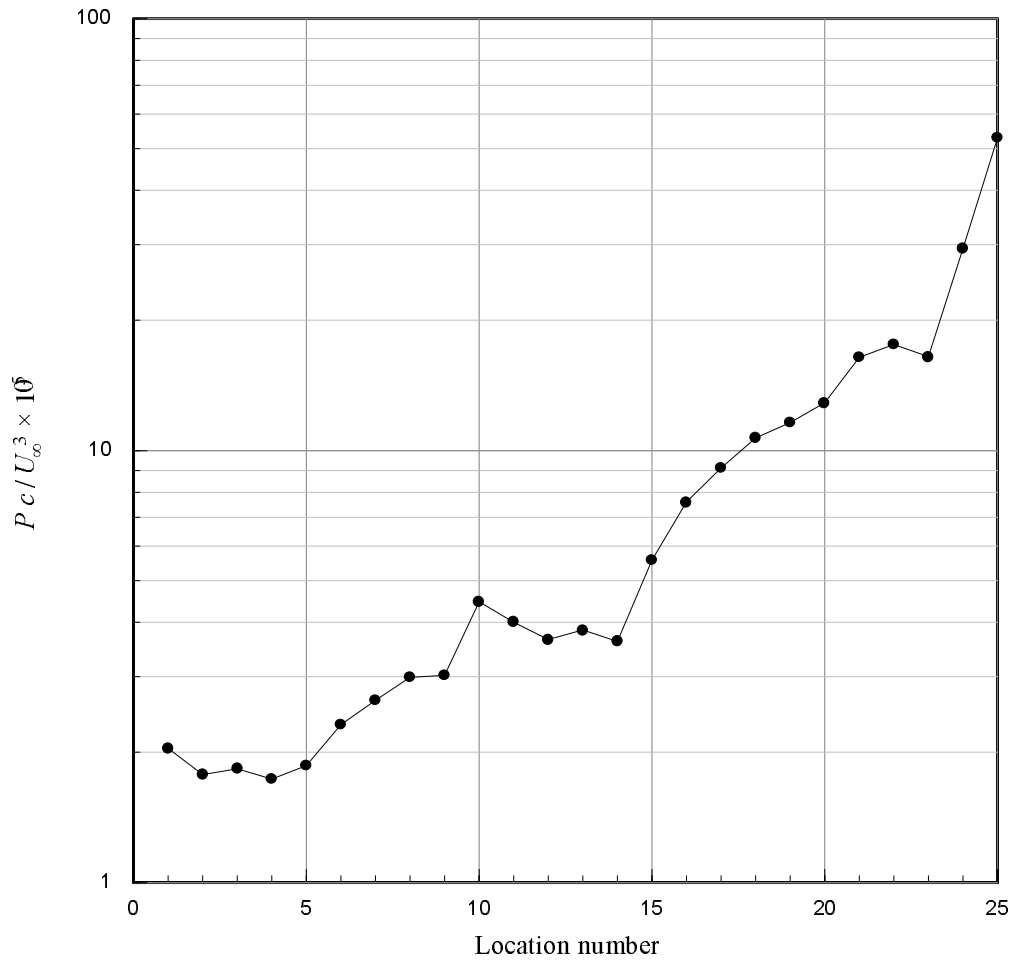
Figure 3.32: Turbulence kinetic energy production at locations identified in Figure 3.31. $x/c = 17.5$, $\Delta/c = -0.125$. $\alpha_1 = \alpha_2 = 5°$.
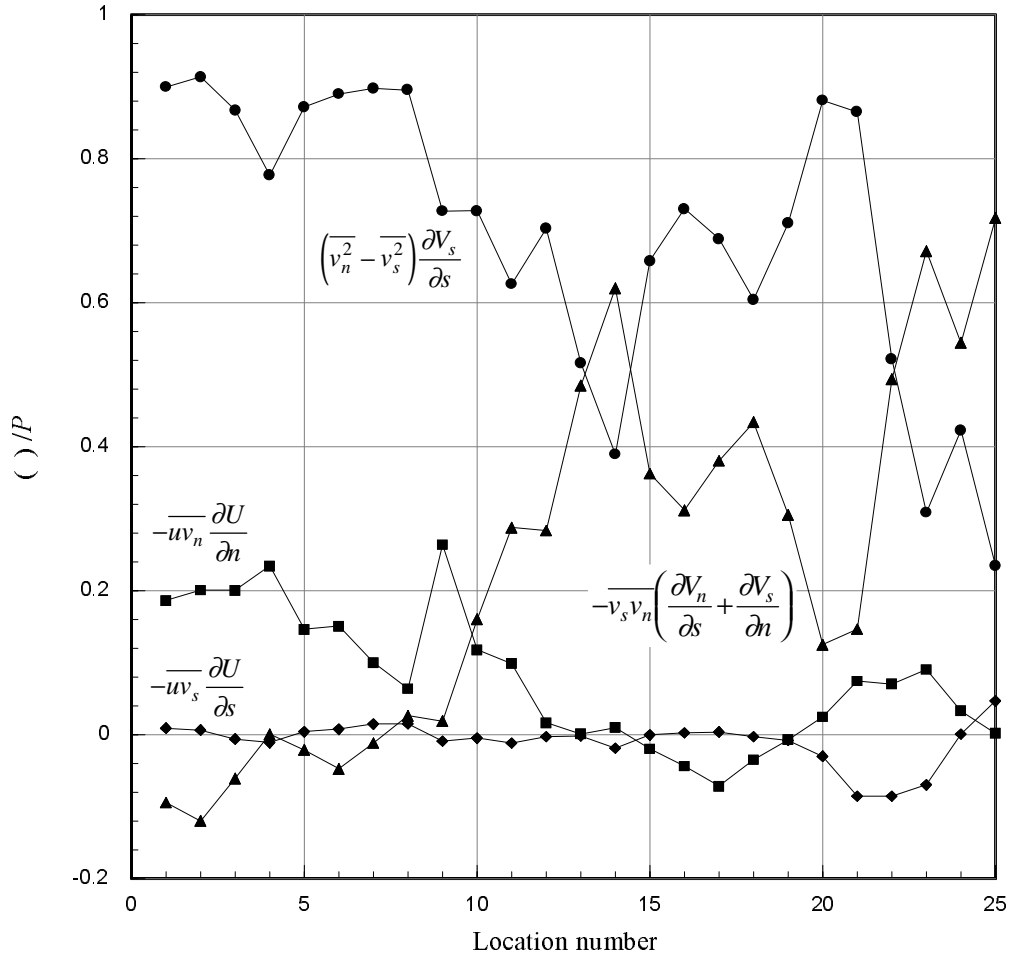
Figure 3.33: Contributions to turbulence kinetic energy production at locations identified in Figure 3.31. $x/c = 17.5$, $\Delta/c = -0.125$. $\alpha_1 = \alpha_2 = 5°$.
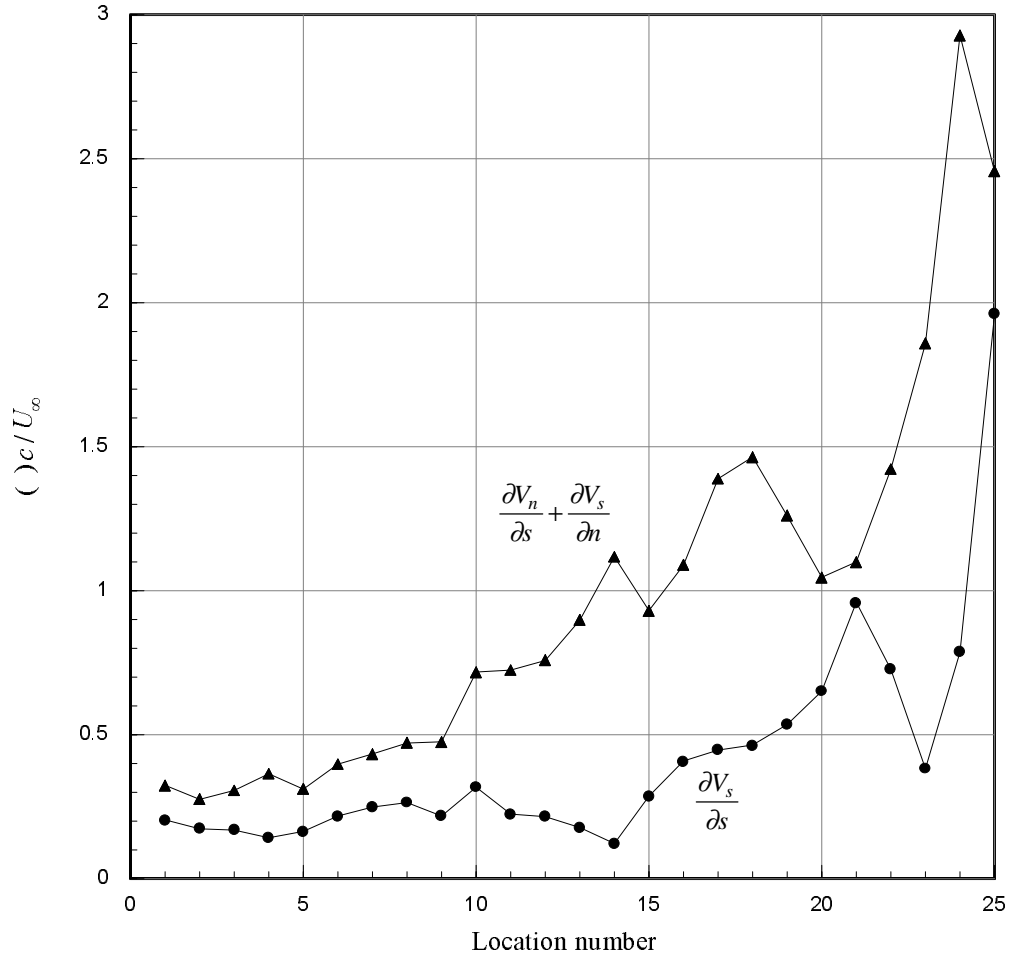
Figure 3.34: Strain rates contributing to turbulence kinetic energy production at locations identified in Figure 3.31. $x/c = 17.5$, $\Delta/c = -0.125$. $\alpha_1 = \alpha_2 = 5°$.
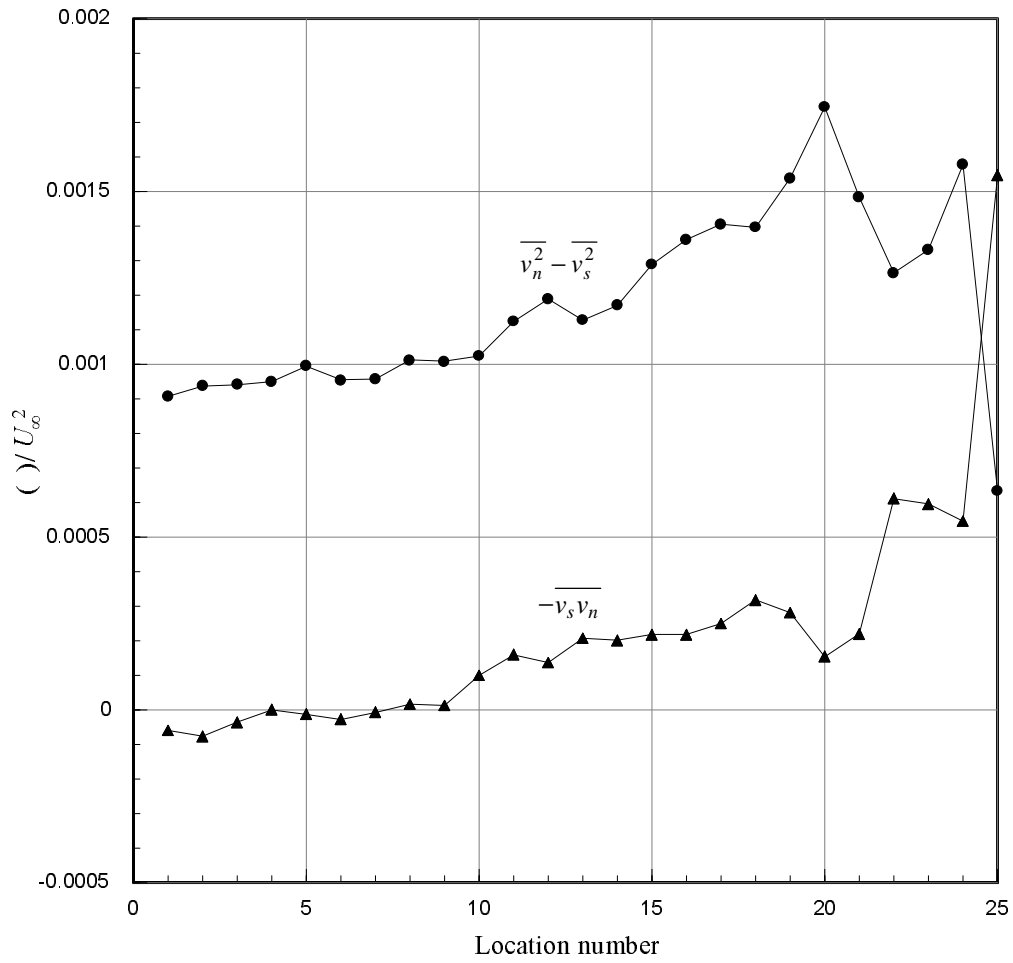
Figure 3.35: Turbulence stresses contributing to turbulence kinetic energy production at locations identified in Figure 3.31. $x/c = 17.5$, $\Delta/c = -0.125$. $\alpha_1 = \alpha_2 = 5°$.
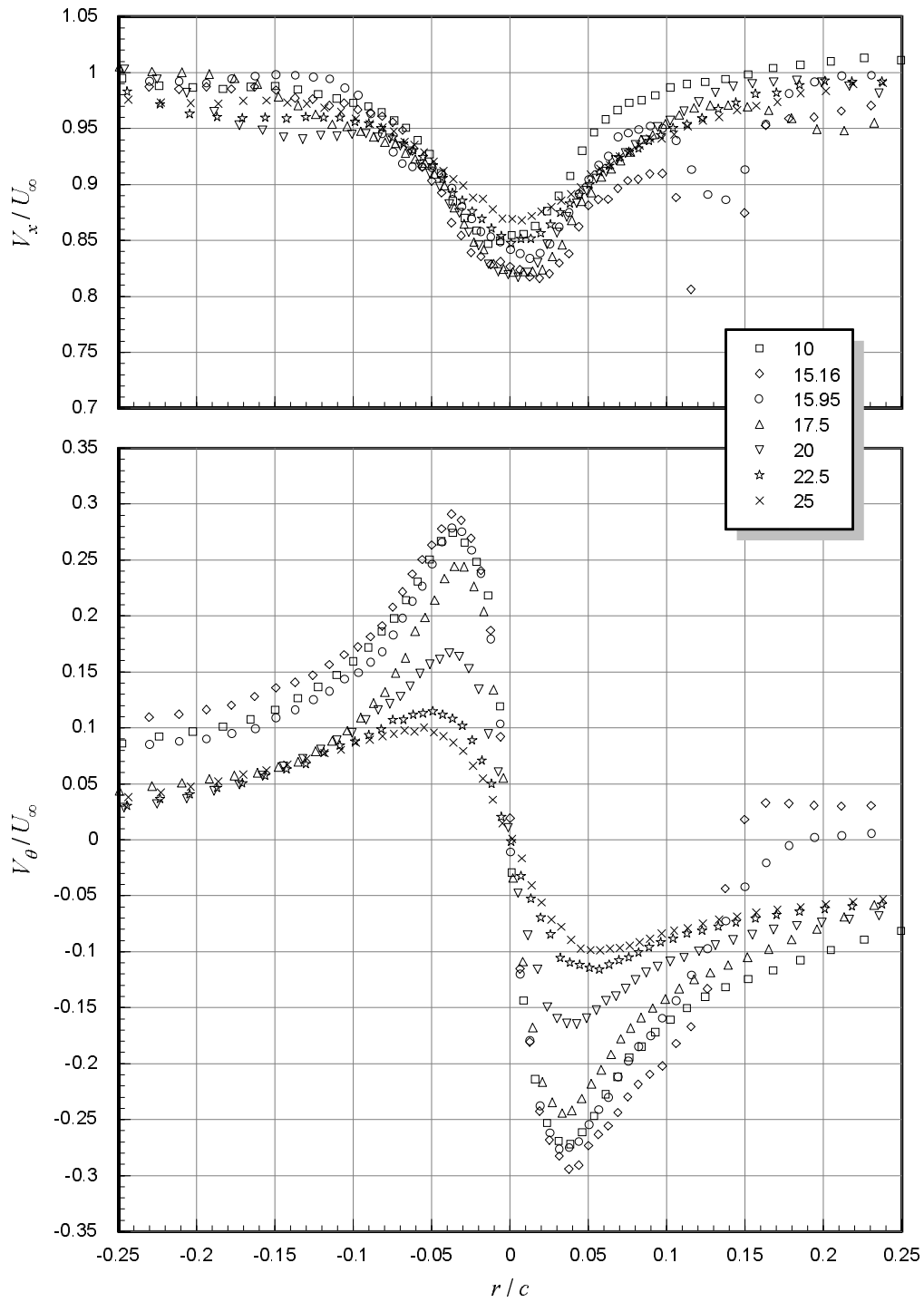
Figure 3.36: Mean axial and tangential velocities measured along z-wise profiles through the core center at various locations downstream of a pressure side passage of $\Delta/c = 0.125$. $\alpha_1 = \alpha_2 = 5°$. Numbers in legend are x/c locations.
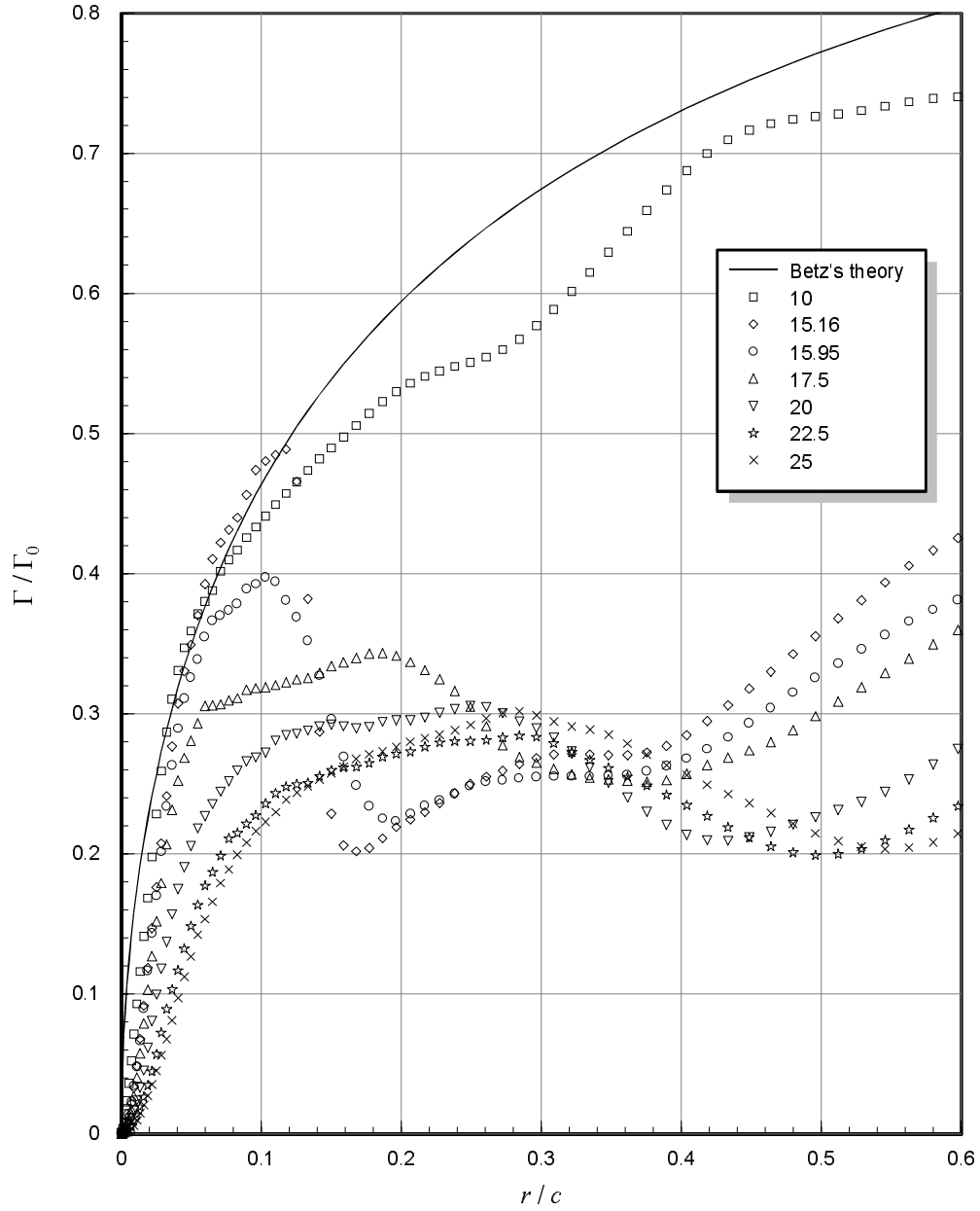
Figure 3.37: Circulation distributions estimated from z-wise profiles through the core center at various locations downstream of a pressure side passage of $\Delta/c = 0.125$. $\alpha_1 = \alpha_2 = 5°$. Numbers in legend are x/c locations.
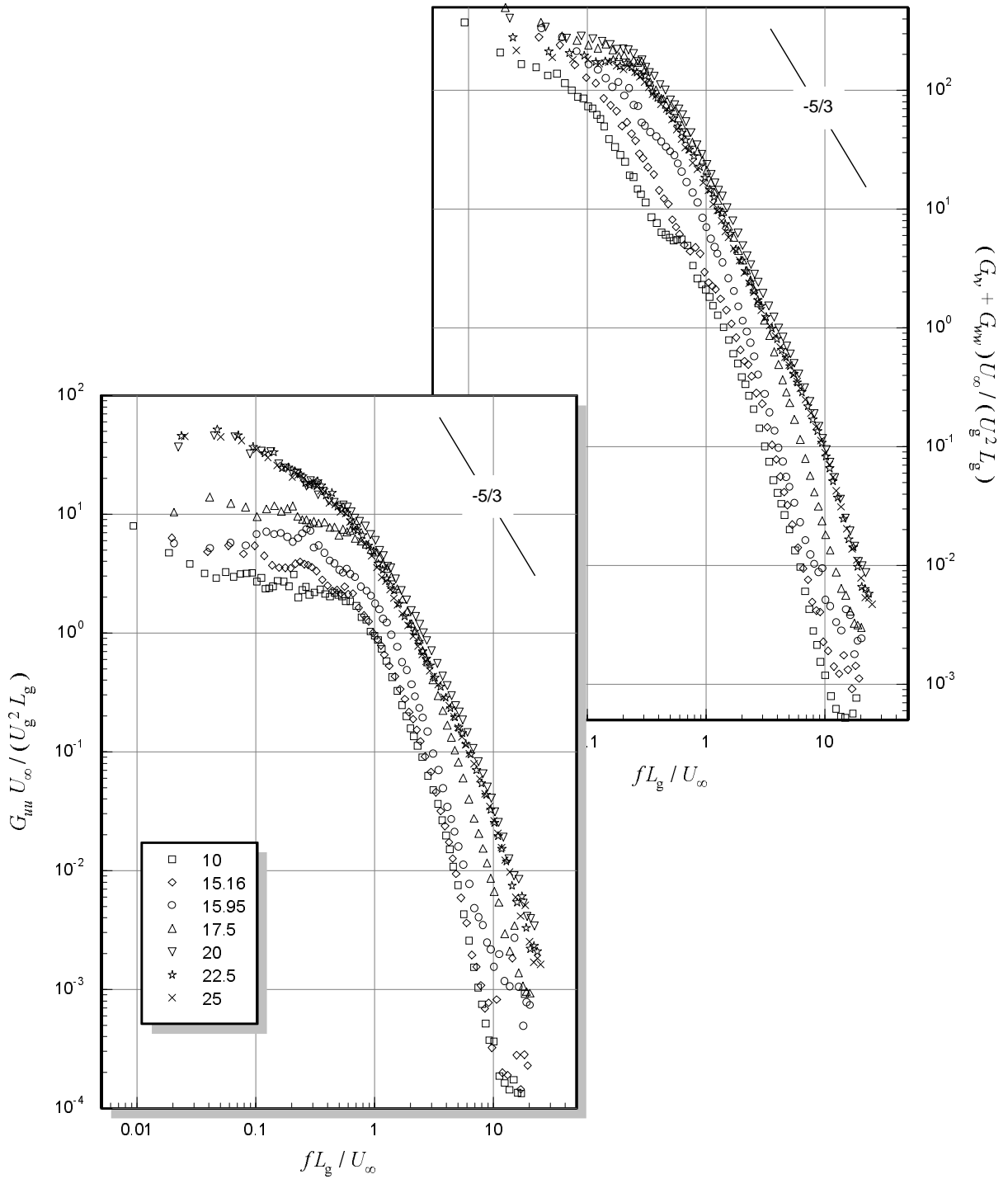
Figure 3.38: Core center velocity autospectra at various locations downstream of a suction side passage of $\Delta/c = 0.125$. $\alpha_1 = \alpha_2 = 5°$. Numbers in legend are x/c locations.
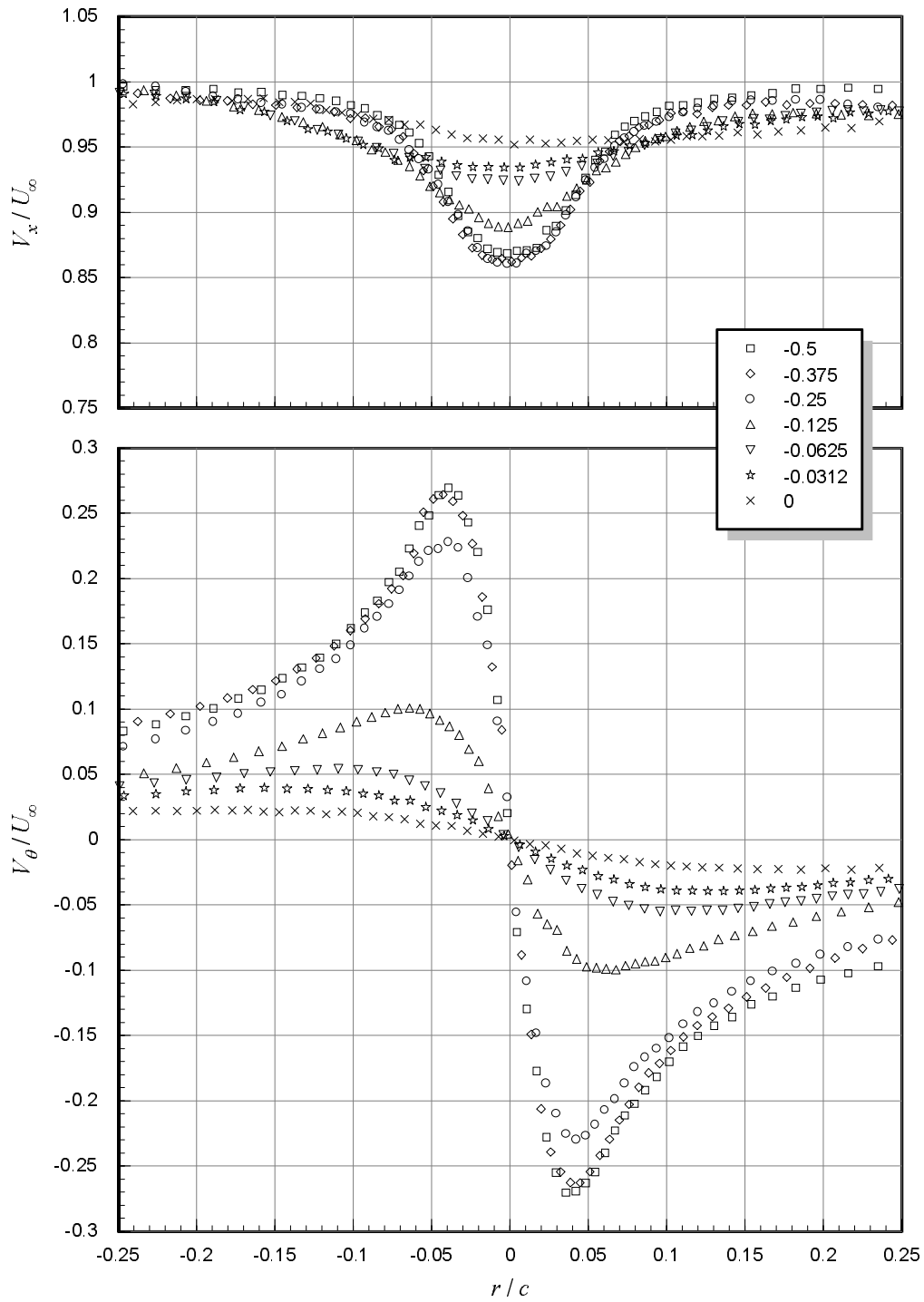
Figure 3.39: Mean axial and tangential velocities measured along z-wise profiles through the core center for various pressure side passage blade–vortex separations (baseline variation). $x/c = 30$, $\alpha_1 = \alpha_2 = 5°$. Numbers in legend are Δ/c values.
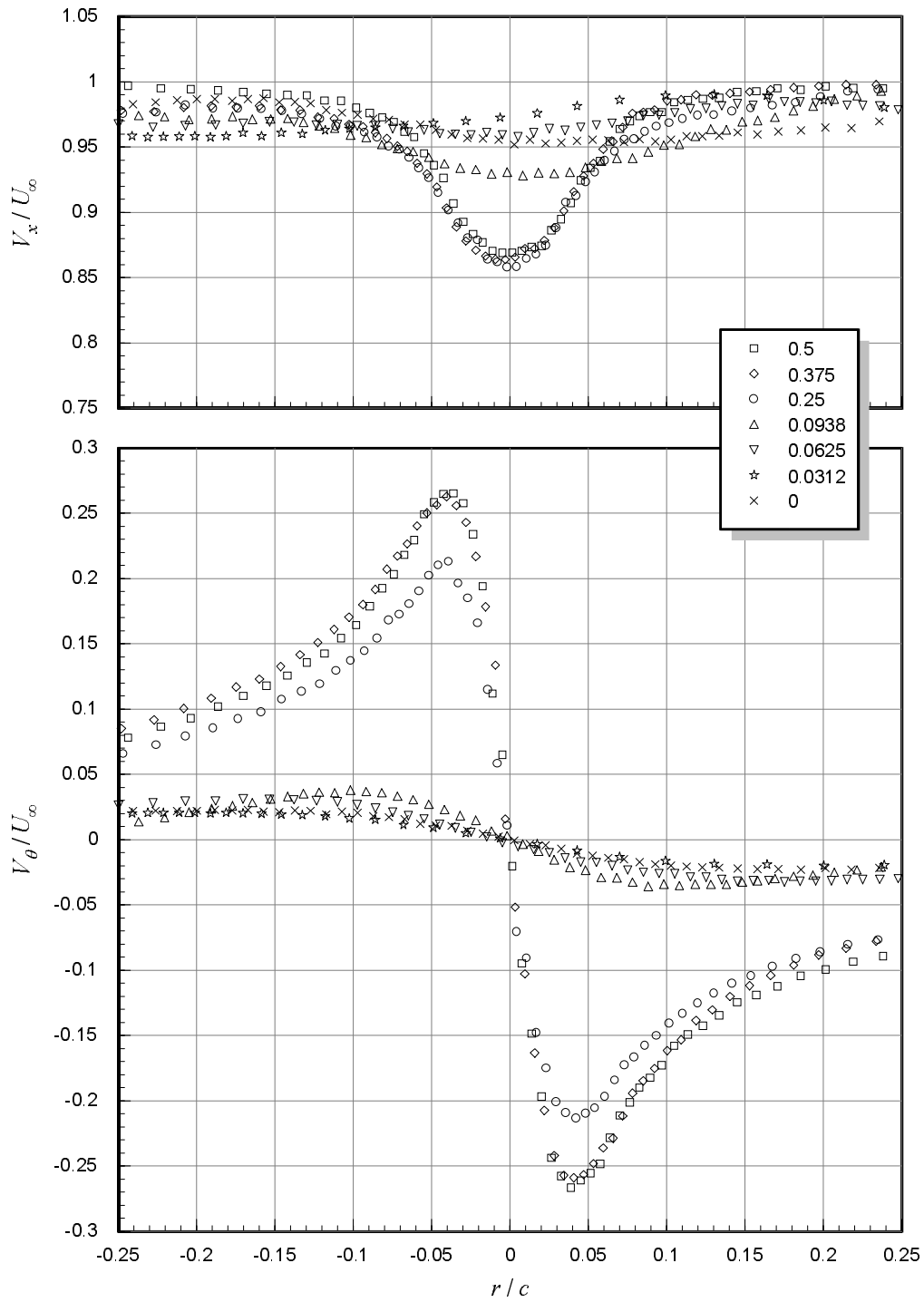
Figure 3.40: Mean axial and tangential velocities at measured along z-wise profiles through the core center for various suction side passage blade–vortex separations (baseline variation). $x/c = 30$, $\alpha_1 = \alpha_2 = 5°$. Numbers in legend are Δ/c values.
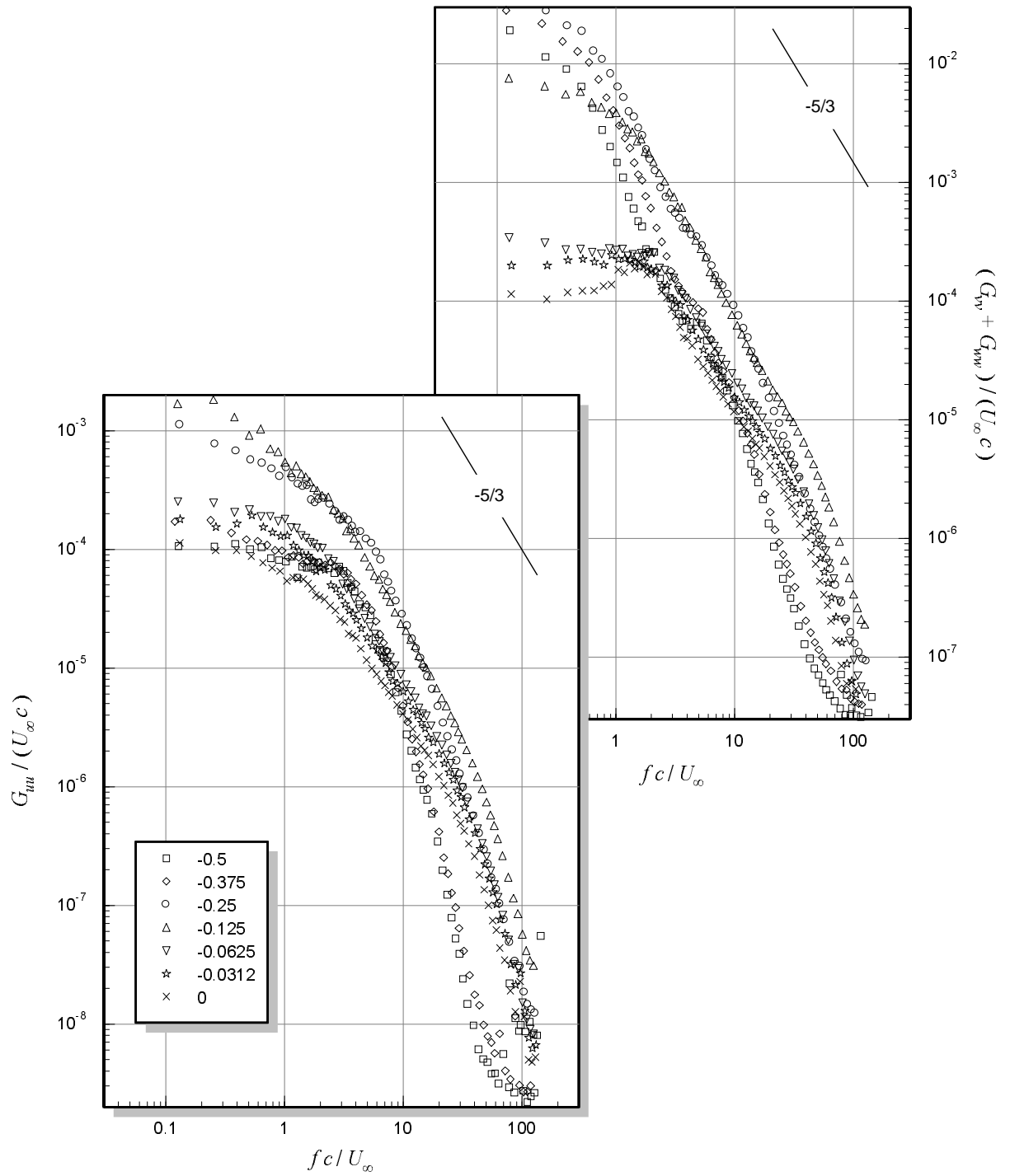
Figure 3.41: Core center velocity autospectra for various pressure side passage blade–vortex separations (baseline variation). $x/c = 30$, $\alpha_1 = \alpha_2 = 5°$. Numbers in legend are Δ/c values.
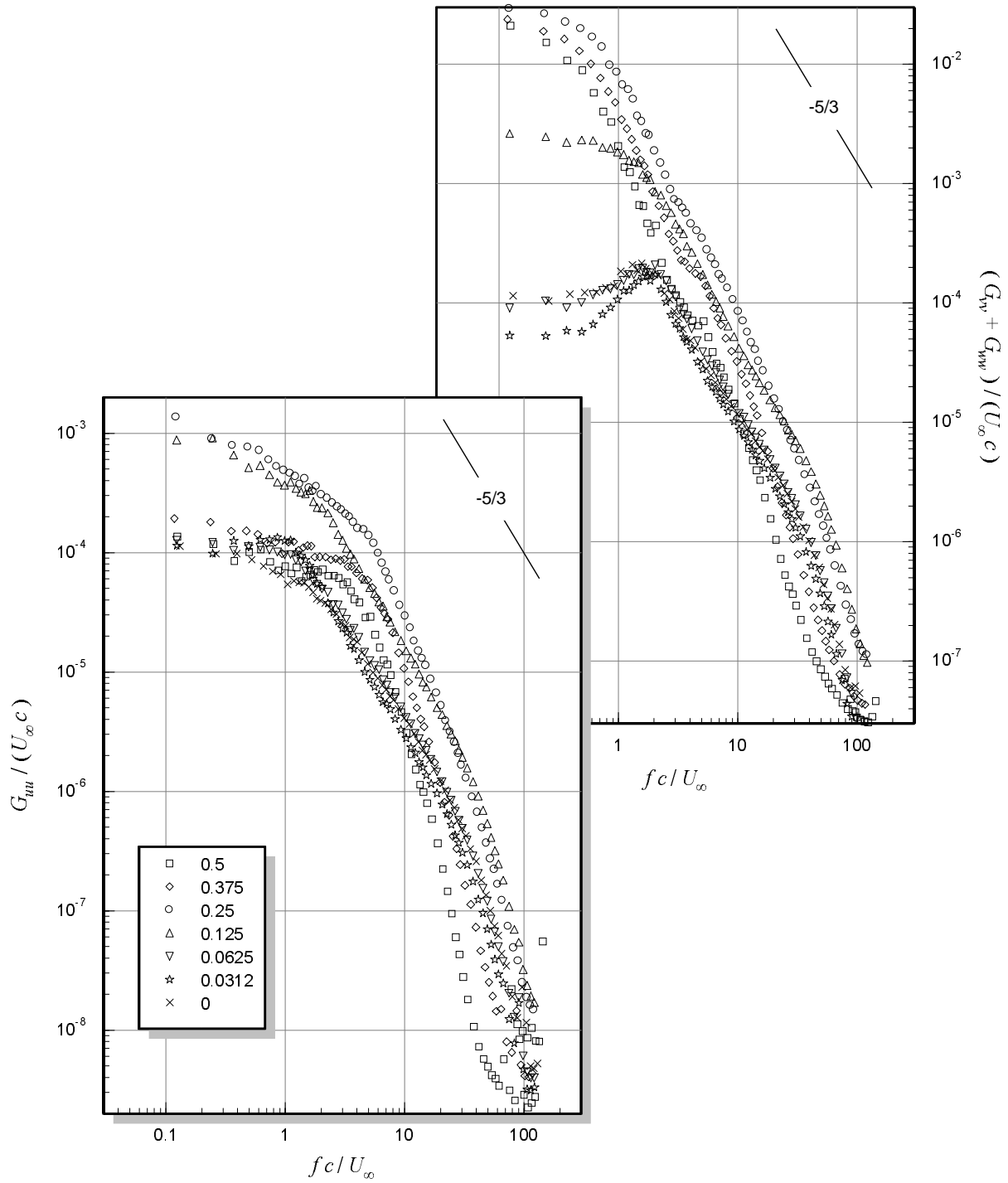
Figure 3.42: Core center velocity autospectra for various suction side passage blade–vortex separations (baseline variation). $x/c = 30$, $\alpha_1 = \alpha_2 = 5°$. Numbers in legend are Δ/c values.
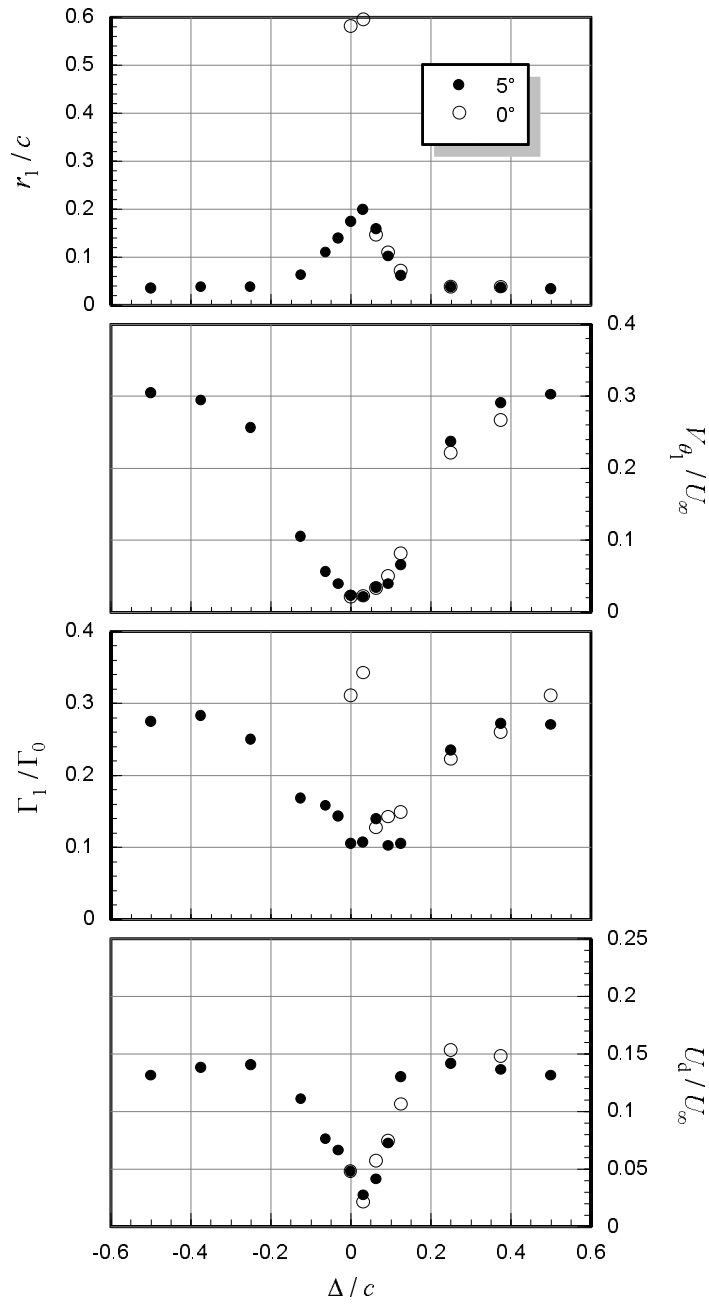
Figure 3.43: Core parameters (radius, peak tangential velocity, core circulation, and axial velocity deficit) as a function of blade–vortex separation for two different interaction blade angles of attack. $x/c = 30$, $\alpha_1 = 5°$. Numbers in legend are α_2 values.
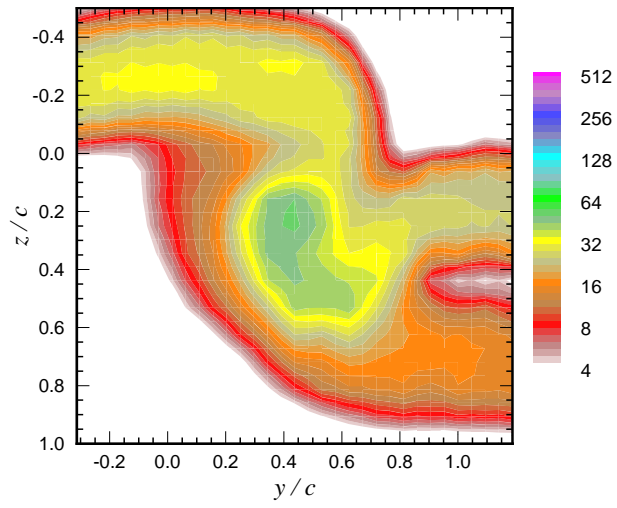
(a) $k/U_\infty^2 \times 10^5$
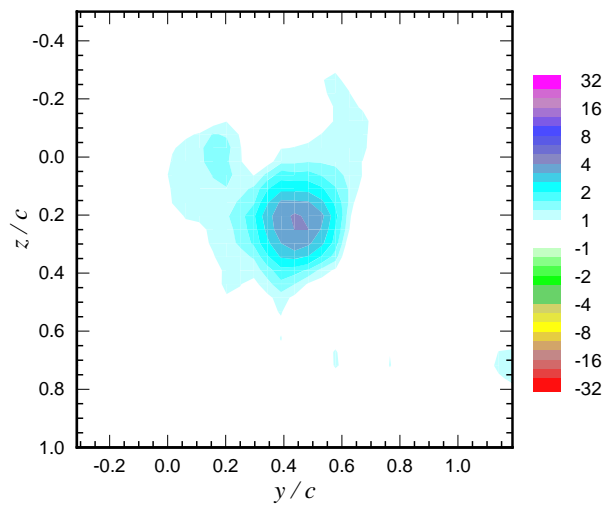
(b) $\Omega_x c/U_\infty \times 10$

Figure 3.44: Contours of: **(a)** turbulence kinetic energy and **(b)** mean axial vorticity at $x/c = 30$ for $\Delta = 0$. $\alpha_1 = \alpha_2 = 5°$.
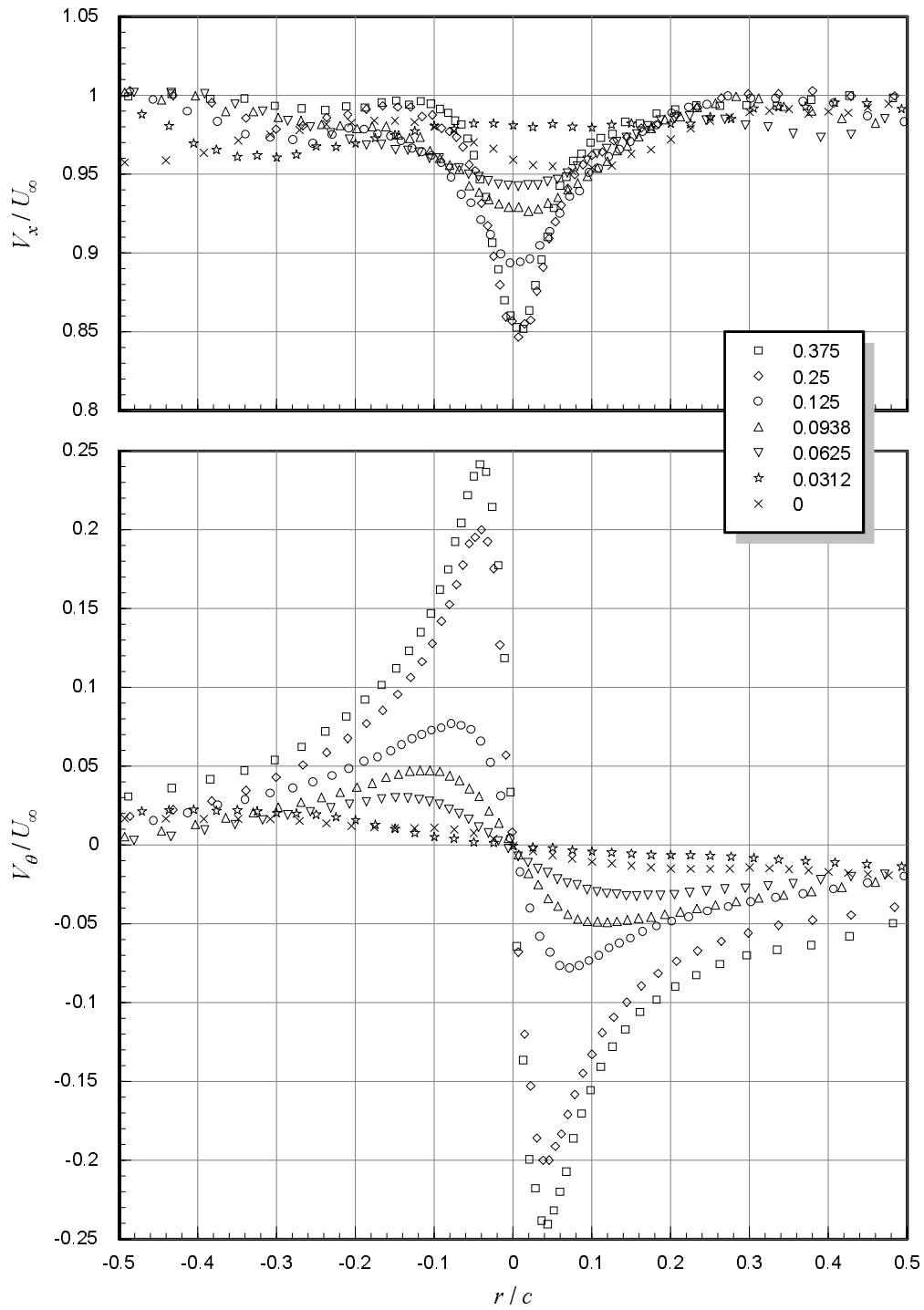
Figure 3.45: Mean axial and tangential velocities measured along z-wise profiles through the core center for various suction side passage blade–vortex separations with interaction blade at $0°$. $x/c = 30$, $\alpha_1 = 5°$. Numbers in legend are Δ/c values.
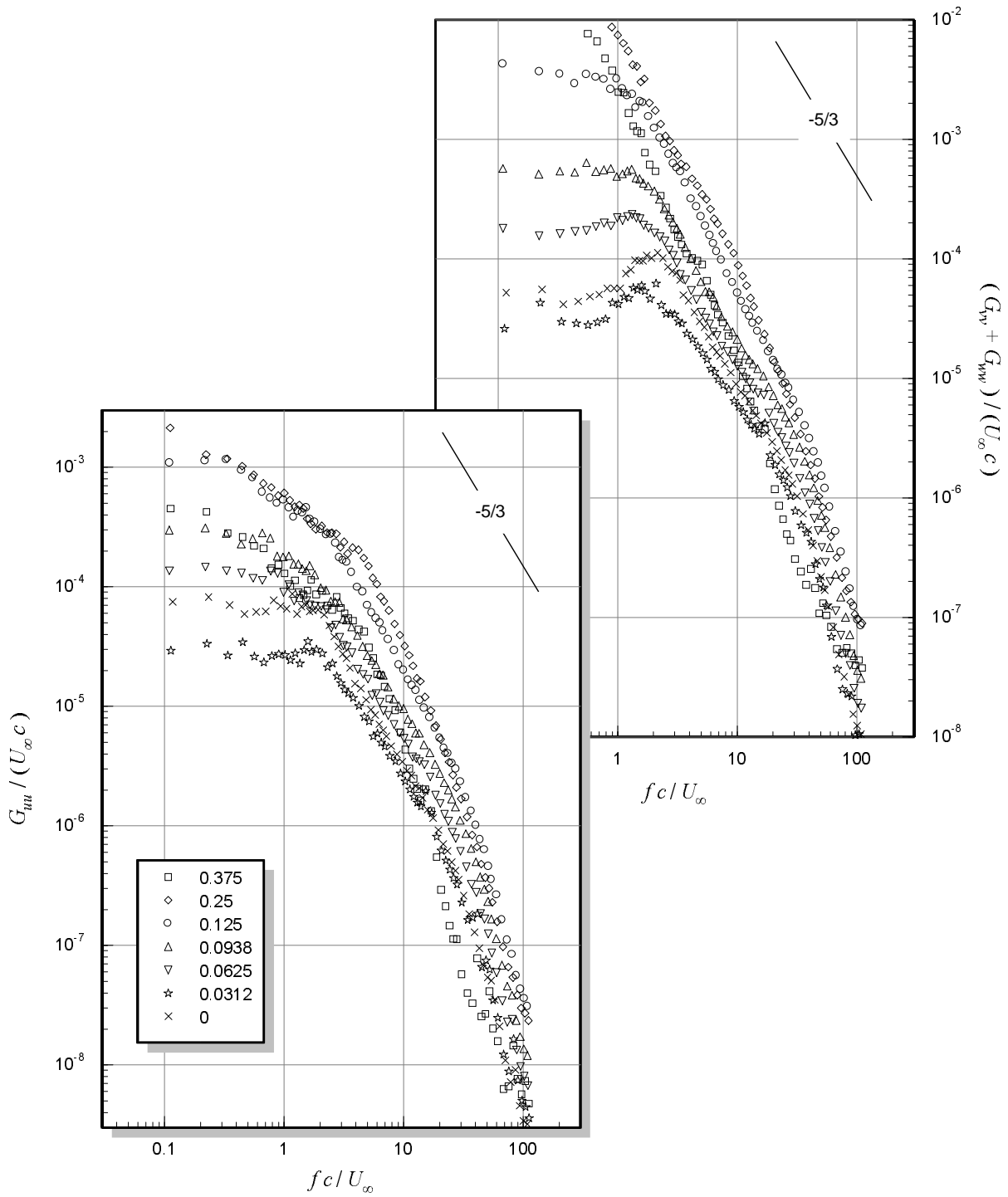
Figure 3.46: Core center velocity autospectra for various suction side passage blade–vortex separations with interaction blade at $0°$. $x/c = 30$, $\alpha_1 = 5°$. Numbers in legend are Δ/c values.
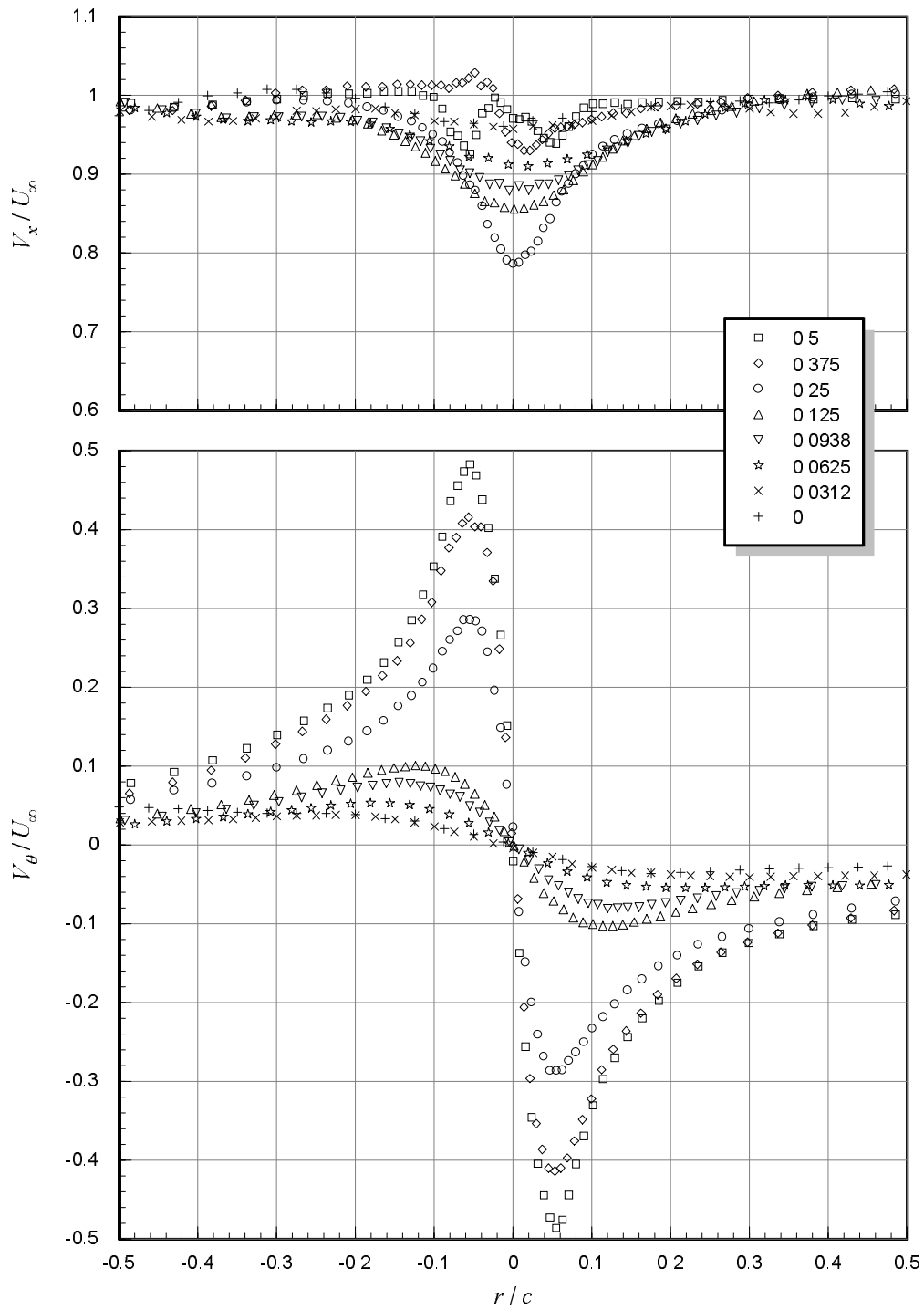
Figure 3.47: Mean axial and tangential velocities measured along z-wise profiles through the core center for various suction side passage blade–vortex separations with generator at $10°$. $x/c = 30$, $\alpha_1 = 5°$. Numbers in legend are Δ/c values.
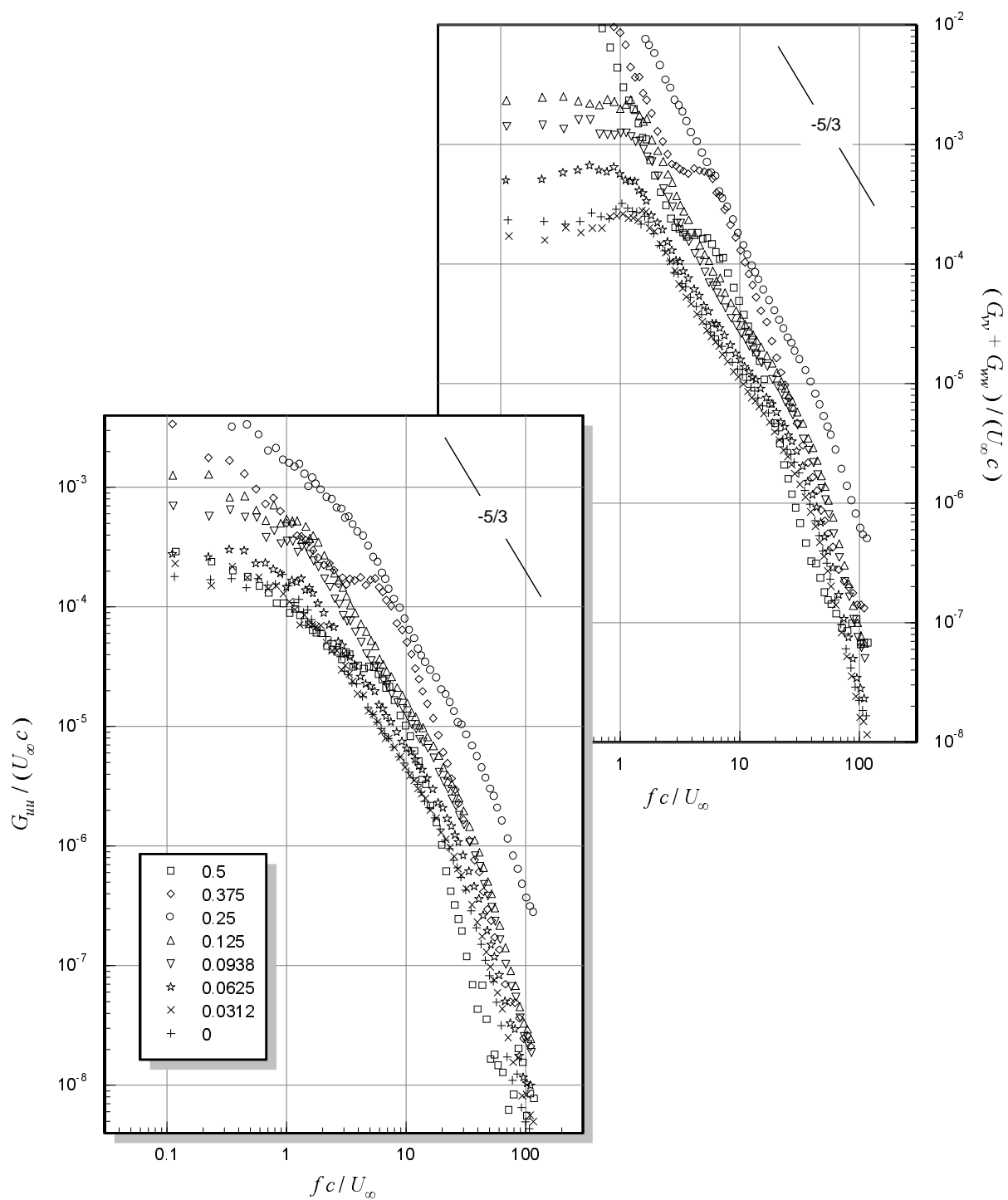
Figure 3.48: Core center velocity autospectra for various suction side passage blade–vortex separations with generator at 10°. $x/c = 30$, $\alpha_2 = 5°$. Numbers in legend are Δ/c values.
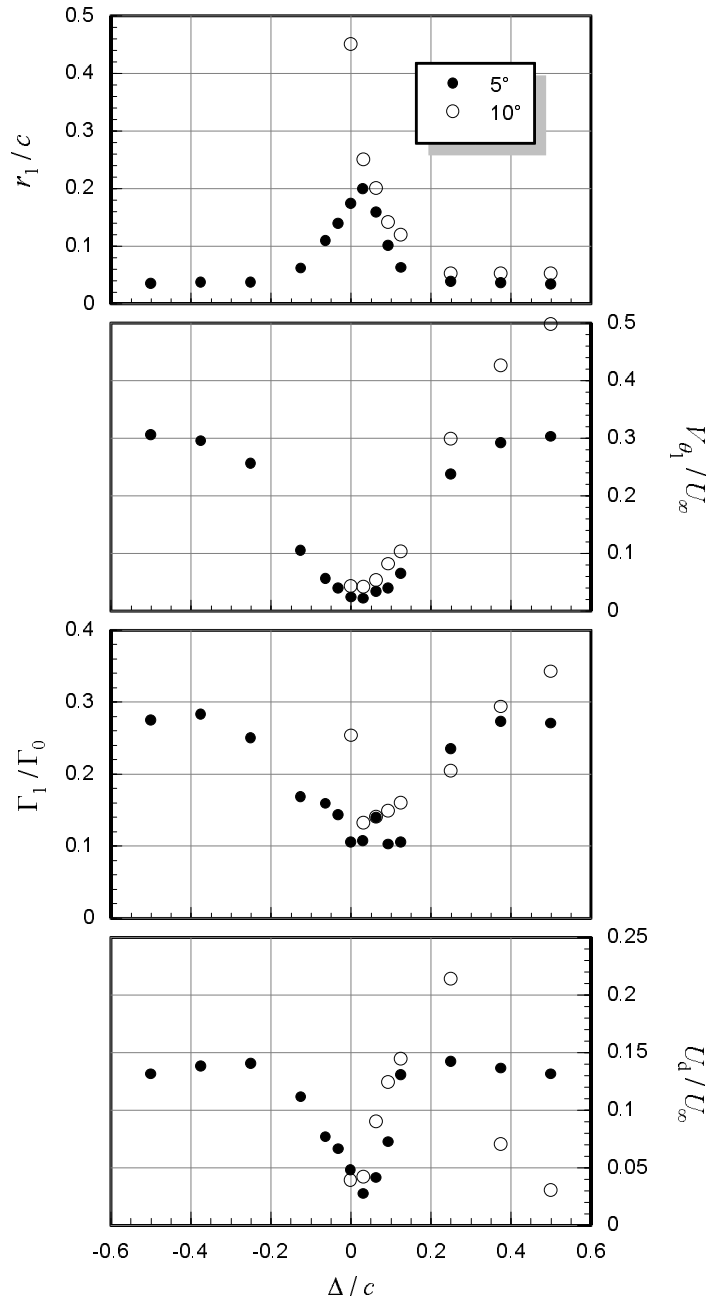
Figure 3.49: Core parameters (radius, peak tangential velocity, core circulation, and axial velocity deficit) as a function of blade–vortex separation for two different generator angles of attack. $x/c = 30$, $\alpha_2 = 5°$. Numbers in legend are α_1 values.
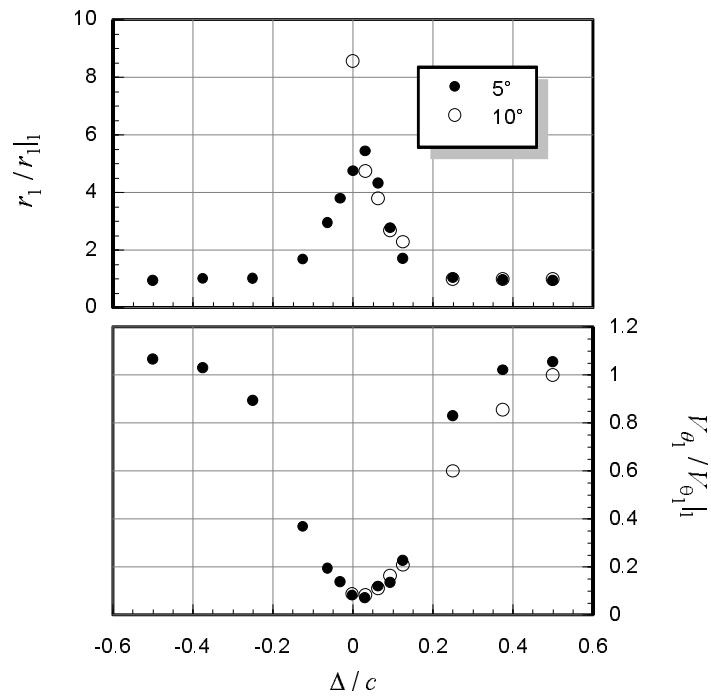
Figure 3.50: Core parameters (radius, peak tangential velocity, core circulation, and axial velocity deficit) as a function of blade–vortex separation for two different generator angles of attack normalized on undisturbed values. $x/c = 30$, $\alpha_2 = 5°$. Numbers in legend are α_1 values.
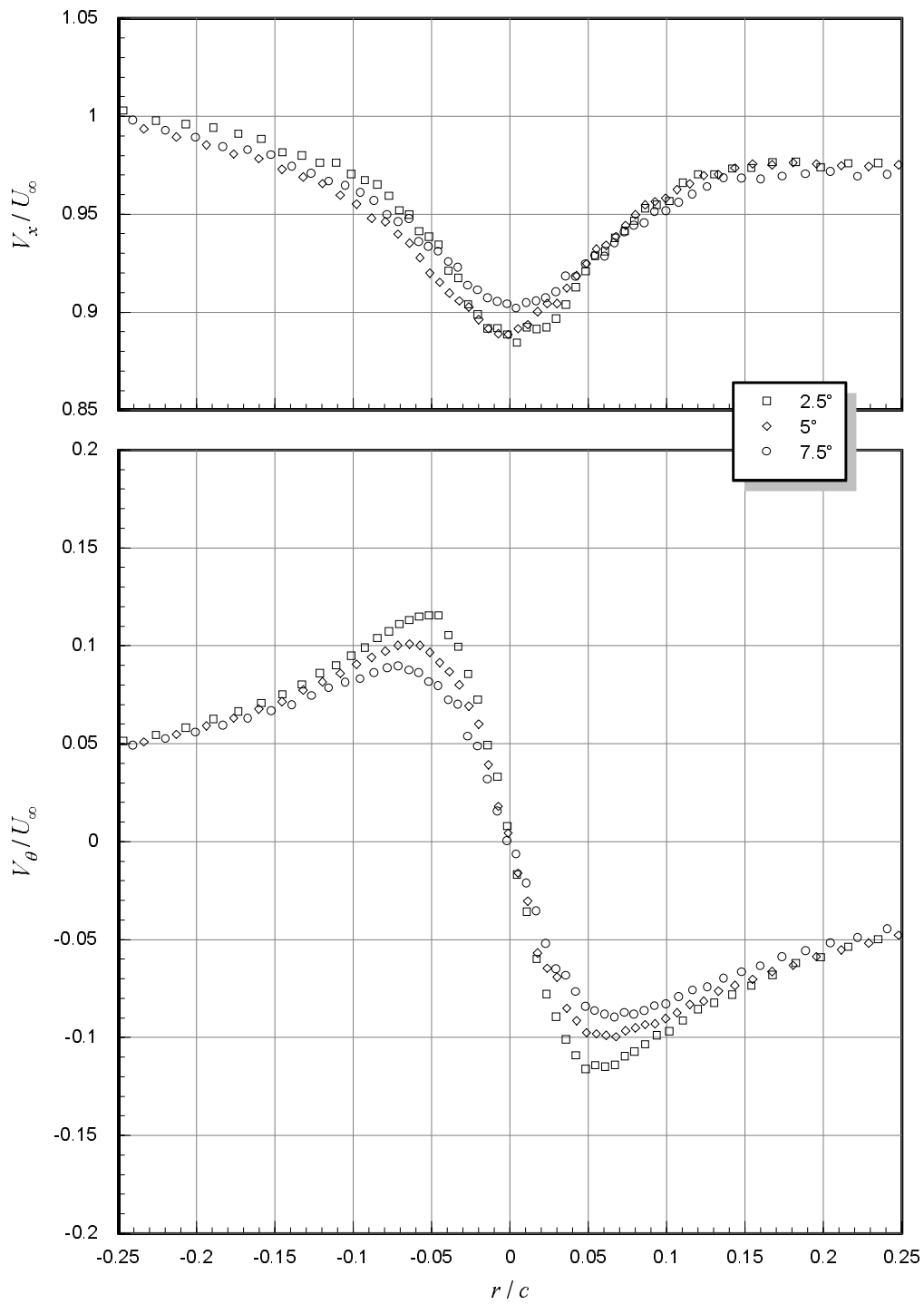
Figure 3.51: Mean axial and tangential velocities measured along z-wise profiles through the core center for various interaction blade angles of attack. $x/c = 30$, $\alpha_1 = 5°$. Numbers in legend are α_2 values.

105
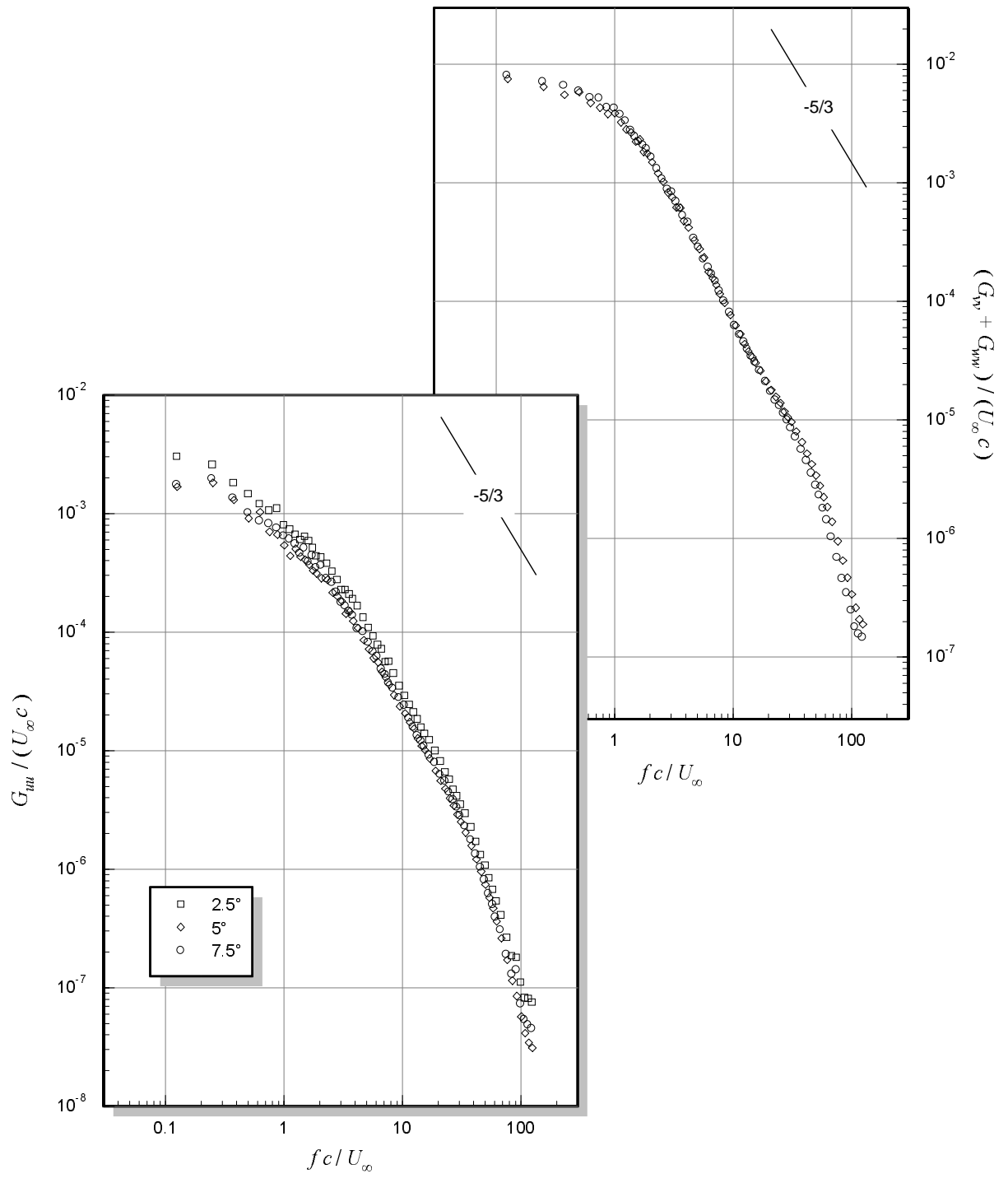
Figure 3.52: Core center velocity autospectra for various interaction blade angles of attack. $x/c = 30$, $\alpha_1 = 5°$. Numbers in legend are α_2 values.

106
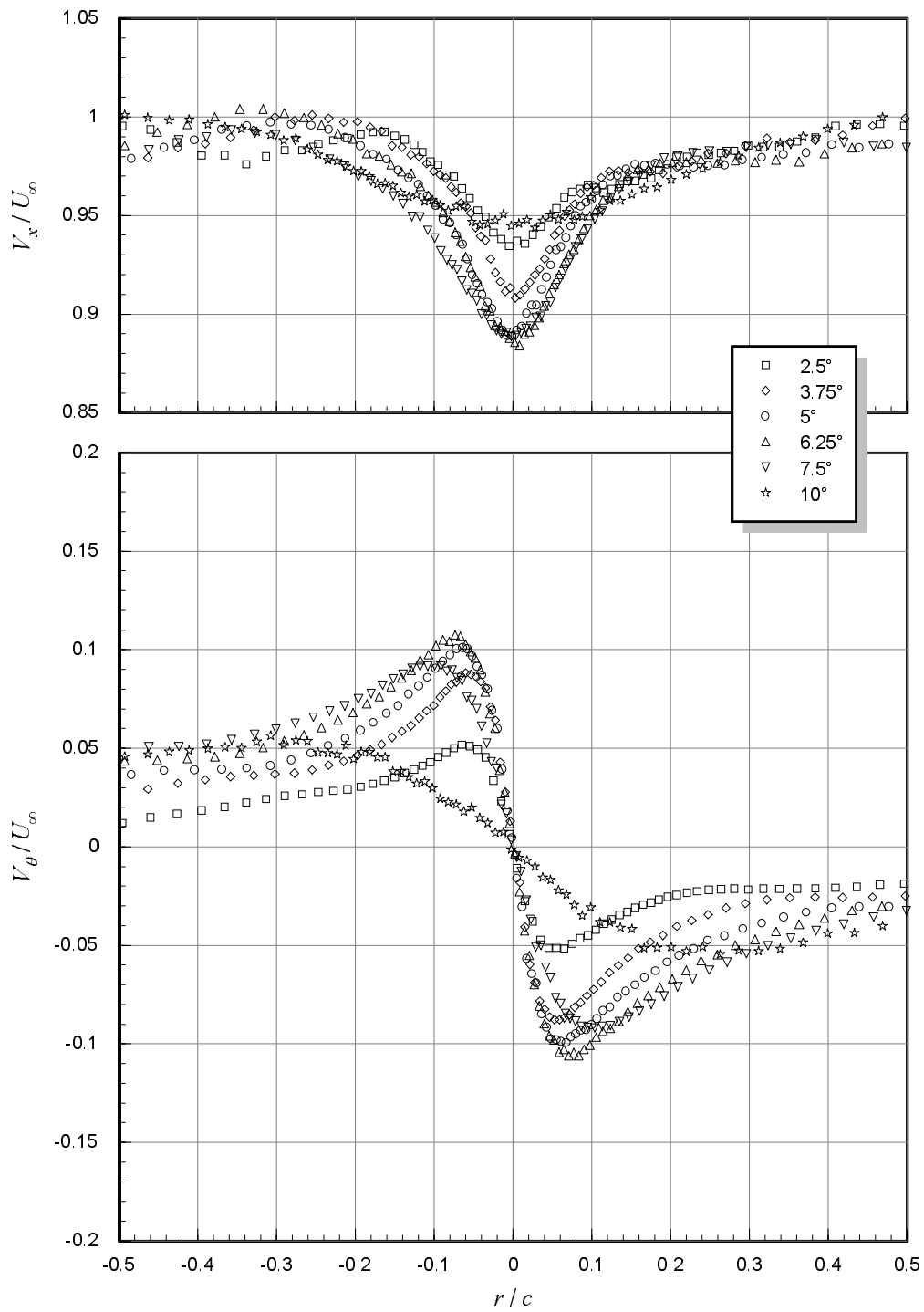
Figure 3.53: Mean axial and tangential velocities measured along z-wise profiles through the core center for various equal angles of attack of the vortex generator and interaction blade. $x/c = 30$. Numbers in legend are $\alpha_1 = \alpha_2$ values.
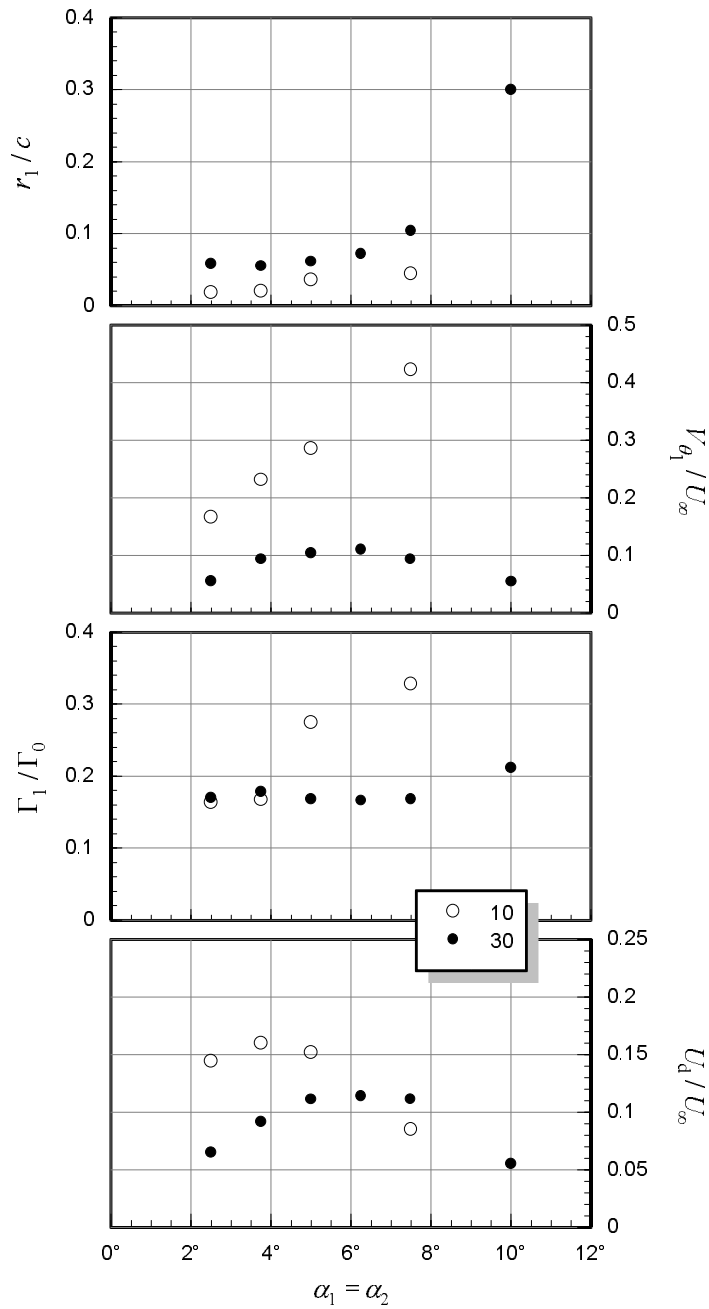
Figure 3.54: Core parameters (radius, peak tangential velocity, core circulation, and axial velocity deficit) as a function of equal vortex generator and interaction blade angles of attack. $x/c = 30$. Numbers in legend are $\alpha_1 = \alpha_2$ values.
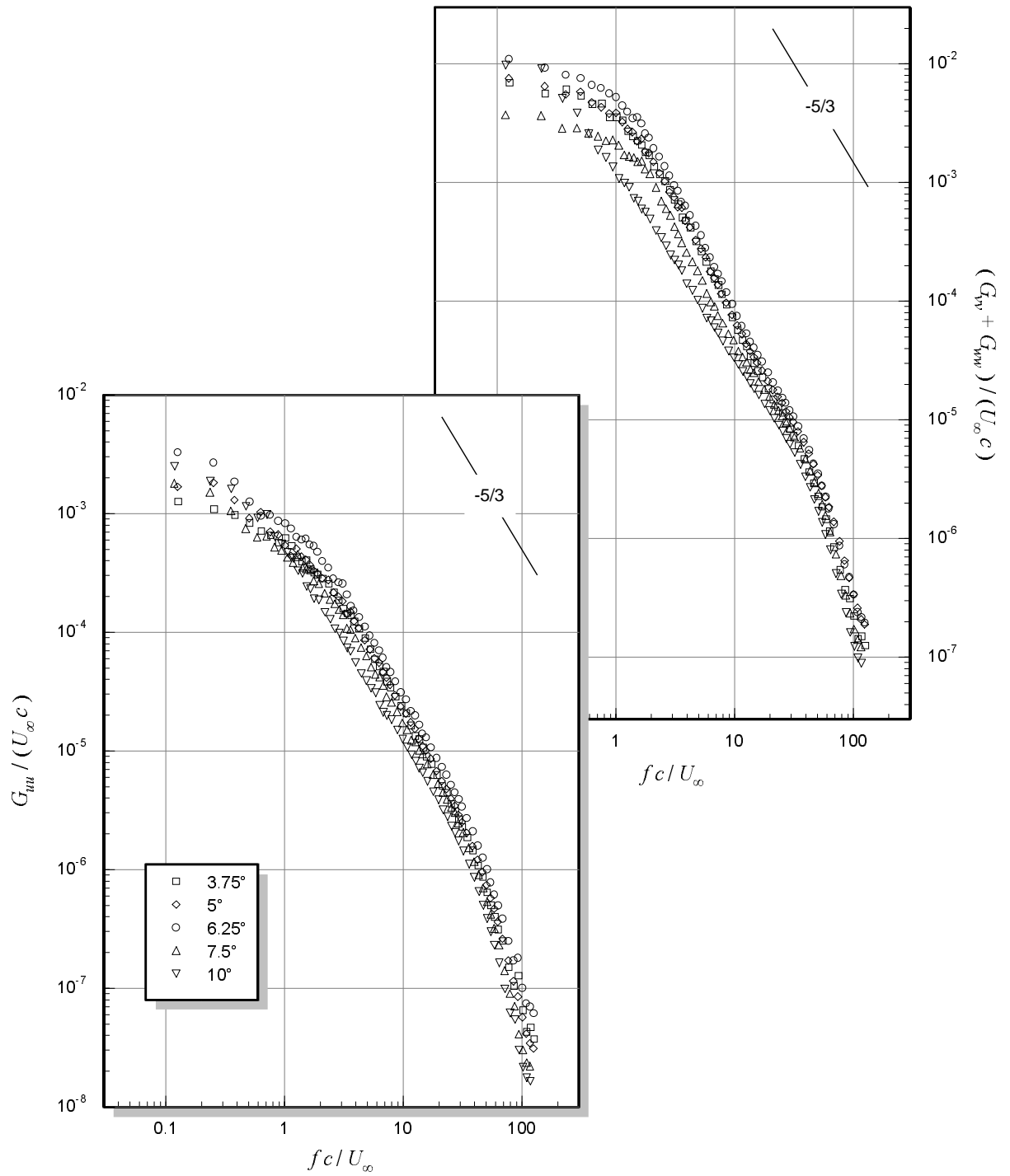
Figure 3.55: Core center velocity autospectra for various equal angles of attack of the vortex generator and interaction blade. $x/c = 30$. Numbers in legend are $\alpha_1 = \alpha_2$ values.
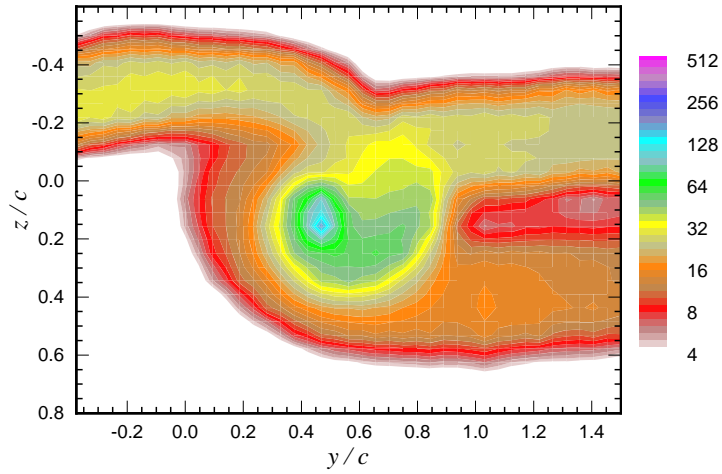
(a) $\alpha_1 = \alpha_2 = 2.5°$
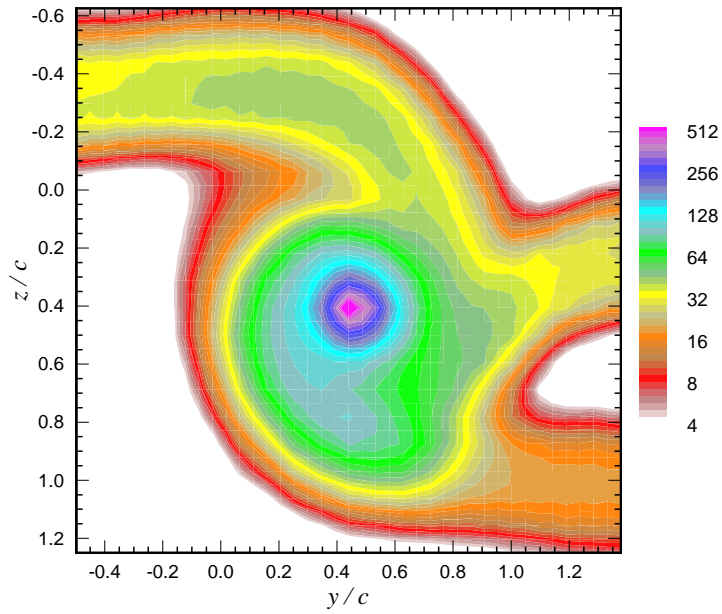
(b) $\alpha_1 = \alpha_2 = 7.5°$

Figure 3.56: Contours of turbulence kinetic energy $(k/U_\infty^2 \times 10^5)$. $x/c = 30$, $\Delta/c = -0.125$.

Chapter 4

Theoretical modeling

Although a large amount of data has been presented describing the flowfield downstream of a perpendicular interaction between a streamwise vortex and an airfoil, the data provides little predictive capability beyond interpolation. In the following sections, simple theoretical models are developed which attempt to predict some of the features seen in the flow. The intent was to include enough fluid dynamics into the models so that they could be used for situations outside the experimental test matrix.

4.1 Shed vorticity

Possibly the most interesting feature of the flow is the negative vorticity which is shed by the interaction blade as a result of the angle of attack variation induced by the passing vortex (see Figure 3.14). The following is a simple inviscid analysis which predicts the shed vorticity distribution using an adaptation of Prandtl's lifting line theory. The derivation shown here is for a vortex of arbitrary circulation distribution passing above a wing constrained at each end by infinite flat plates. This type of lifting line analysis has been performed previously by Hancock [27] for the loading produced by a free line vortex passing above a two-dimensional wing. Filotas [54] used a lifting surface analysis to predict the loading and found that Hancock's lifting line analysis overpredicts the span loading in regions of rapidly changing local angle of attack.

4.1.1 Derivation

Prandtl's lifting line theory is to be modified to account for the non-uniform inflow which the interaction blade experiences. It is assumed that the effects of the non-uniform inflow with respect to the shed vorticity are the same as those of a twist on the blade, with the twist angle distribution being equal to the angle of attack distribution produced by the vortex $(\alpha_v(y))$. For example, the situation shown in Figure 1.2 is assumed equivalent to a uniform flow impinging on a blade with an angle of attack $\alpha(y) = \alpha_2 + \alpha_v(y)$ where α_2 is the actual angle of attack of the interaction blade.

From the geometry and coordinates shown in Figure 4.1, $\alpha_{\mathrm{v}}(y)$ is calculated from the initial vortex circulation distribution ($\Gamma_{\mathrm{i}}(r)$) as

$$\alpha_{\mathrm{v}}(y) = \arctan\left(\frac{-W}{U_\infty}\right) \approx \frac{\Gamma_{\mathrm{i}}(r)\,(y_{\mathrm{v}} - y)}{2\pi r^2 U_\infty} \tag{4.1}$$

where y_{v} is the y-location of the vortex center and r is radial distance from the vortex center to the point on the blade located by y, *i.e.*

$$r = \sqrt{\Delta^2 + (y_{\mathrm{v}} - y)^2}. \tag{4.2}$$

Note that we are assuming that the blade has no influence on its inflow.

The lifting line theory equations used to compute the shed vortex sheet strength distribution from $\alpha(y)$ depend on the configuration. In the present situation of a blade which completely spans the wind-tunnel walls, the relationship between $\alpha(y)$ and the circulation distribution on the blade ($\Gamma_{\mathrm{b}}(y)$) is

$$\alpha(y) = \frac{\Gamma_{\mathrm{b}}(y)}{\pi c\, U_\infty} + \frac{1}{4\pi\, U_\infty} \int_{-\infty}^{\infty} \frac{1}{y - y'} \frac{d\Gamma_{\mathrm{b}}}{dy'}\, dy' \tag{4.3}$$

where y' is a dummy variable for y. The reflections provided by the wind tunnel walls will result in the $\Gamma_{\mathrm{b}}(y)$ being periodic over twice the distance between the walls ($2b$). Under these conditions the solution to this equation is the series

$$\Gamma_{\mathrm{b}} = b\, U_\infty \left[\mathrm{A}_0 \frac{\pi c}{b} + \sum_{n=1\ldots\infty} \mathrm{A}_n \left(\frac{b}{\pi c} + \frac{n\pi}{4}\right)^{-1} \cos\left(\frac{n\pi}{b}(y - h)\right) \right] \tag{4.4}$$

where h is defined in Figure 4.1 and the A_n's are coefficients in the Fourier cosine series for $\alpha(y)$, *i.e.*

$$\alpha(y) = \mathrm{A}_0 + \sum_{n=1\ldots\infty} \mathrm{A}_n \cos\left(\frac{n\pi}{b}(y - h)\right). \tag{4.5}$$

This soultion is quite different than the solution for a blade with a finite span in external flow. Now the strength of the vortex sheet shed from the blade can be calculated as

$$\gamma_{\mathrm{b}}(y) = -\frac{d\Gamma_{\mathrm{b}}}{dy} = \pi\, U_\infty \sum_{n=1\ldots\infty} n\mathrm{A}_n \left(\frac{b}{\pi c} + \frac{n\pi}{4}\right)^{-1} \sin\left(\frac{n\pi}{b}(y - h)\right) \tag{4.6}$$

4.1.2 Comparison with experimental data

The theoretical shed vorticity distribution described above is dependent only on the magnitude of the blade–vortex separation, *i.e.* it is the same for either pressure or suction side passage. The experimental data presented in Section 3.3 and 3.4.1 indicate that there are some differences between pressure and suction side passages. Possible contributors to these differences are hypothesized, but

this inviscid analysis is not capable of accounting for any of these complex viscous effects. However, the definition of the blade–vortex separation used in the theoretical model (*i.e.* the distance between the vortex centerline and the blade quarter-chord) is not the same as the definition used in the experiment (see Figure 2.2). Obviously the blade has an influence on the vortex path upstream which is not accounted for in the model, but the location of the vortex near the blade leading edge is more significant than its location further upstream. Since this location is not precisely known, the definition of the blade–vortex separation used for the experimental data will also be used in the theoretical model when comparing the two.

The second observation immediately apparent from the results of the derivation, is that the shed vorticity is not dependent upon the interaction blade angle of attack. (Equation 4.6 is not dependent upon $A_0 = \alpha_2$.) Experimental data discussed in Sections 3.4.2 and 3.5.1 shows that the core parameters are not heavily dependent upon the interaction blade angle of attack; thereby supporting the results of the inviscid analysis, at least for separations large enough where changes to the core have been shown to occur primarily due to its interaction with the shed vorticity.

Two calculations of the vortex sheet strength are shown in Figure 4.2 for a blade–vortex separation of $|\Delta/c| = 0.125$. The first is a direct evaluation of Equations 4.5 and 4.6 using the measured undisturbed generator vortex circulation distribution at $x/c = 10$ (see Figure 3.7). Another calculation was done with a limit imposed on the change in lift coefficient which can be experienced by the blade $\Delta C_{L_{max}}$. The idea of imposing a limit is based upon the research of Ham [25] which suggests that the spanwise pressure gradient supplied by the vortex limits, through flow separation, the amount of loading which can be induced on the blade. For typical helicopter rotor blade–vortex interactions, this limits the maximum incremental lift coefficient to less than 0.3.

To estimate the shed vorticity distribution from the experimental data, the y-z plane measurements made at $x/c = 15.16$ with $\alpha_1 = \alpha_2 = 5°$ and $\Delta/c = -0.125$ were used (Figure 3.20). The vortex sheet strength is simply the difference in the V-component of velocity on either side of the sheet. However, Figure 3.14 shows that the shed vorticity is not infinitely thin in the z-direction, therefore the z-locations defining the edges of the sheet must be chosen. This decision must be carefully made considering the contours of the V-component of velocity shown in Figure 4.3. Included in the figure are contour lines showing the edge of the negative vorticity region and the edge of the turbulence. The lower boundary (more positive z) was chosen to be $z/c = -0.2$ since this line corresponds closely to the turbulent edge of the blade wake and the negative vorticity boundary. The upper boundary is more difficult to determine since the edge of the turbulent blade wake ($z/c \approx -0.375$) does not correspond to the edge of the negative vorticity region ($z/c \approx -0.3$) on this side of the sheet. Fortunately, there is very little change in the contours of V between $z/c = -0.3$ and -0.4, so $z/c = -0.35$ was safely chosen as the upper boundary. Figure 4.2 shows that the theoretical distribution without any limit on $\Delta C_{L_{max}}$ significantly overpredicts the strength of the shed vorticity, however with $\Delta C_{L_{max}} = 0.2$, the theoretical distribution matches the shape

113

and levels of the measured distribution surprisingly well. Obviously, additional experimental data measured in the y-z plane immediately behind the blade for different blade–vortex separations, vortex strengths and interaction blade angles of attack is needed to completely validate the usefulness of this model. It is likely that the $\Delta C_{\mathrm{L_{max}}}$ parameter will be dependent upon the interaction blade angle of attack and the blade–vortex separation (which changes the extent of the spanwise flow on the blade).

The $\Delta C_{\mathrm{L_{max}}}$ limit is much more restrictive than the stall limit for the NACA 0012 airfoil section. The data of Abbott and von Doenhoff [55] indicate that stall occurs at approximately $16°$ which is well above the predicted maximum angle of attack experienced by the interaction blade of $9°$ (see Figure 4.4). Although surface roughness can cause premature airfoil stall, Abbott and von Doenhoff found that there was little effect on the maximum lift coefficient or lift curve slope for roughness strips located more than about $0.2\,c$ behind the leading edge. Since the boundary layer trip on the interaction blade was located 0.2–$0.4\,c$ behind the leading edge, stall due to roughness is not considered a factor.

The analysis of Filotas [54] showed that in regions of rapidly changing local angle of attack lifting line analysis overpredicts the span loading compared to lifting surface analysis. However, neither analysis accounts for the spanwise velocities induced on the blade which might cause localized stall; thereby limiting the strength of the shed streamwise vorticity.

4.2   Combined circulation distribution

The experimental data of Section 3.3 shows that the shed vorticity has a profound effect on the circulation distribution of the vortex. By using a method similar to Betz's theory (Betz [46]) circulation distribution of the vortex downstream of the interaction can be predicted. It is assumed that the vorticity contained by an incremental portion of the vortex sheet lying at a distance r from the vortex center remains at this distance, but becomes distributed into an annulus. The final circulation distribution of the vortex is therefore $\Gamma_{\mathrm{f}}(r) = \Gamma_{\mathrm{i}}(r) + \delta\Gamma(r)$ where $\delta\Gamma(r)$ is the additional circulation provided by the vortex sheet at $r > \Delta$ which can be calculated as:

$$\delta\Gamma(r) = \int_{\sqrt{r^2-\Delta^2}}^{-\sqrt{r^2-\Delta^2}} \frac{d\Gamma_{\mathrm{b}}}{dy}\, dy = 2\Gamma_{\mathrm{b}}(\sqrt{r^2 - \Delta^2}). \tag{4.7}$$

Figure 4.5 shows a comparison between predicted circulation distributions and the distributions calculated from the y-z plane measurements for $x/c = 15.16$, 15.95, 17.5, and 20. The predicted distribution with $\Delta C_{\mathrm{L_{max}}} = 0.2$ matches the measured distributions for $x/c < 20$ exceptionally well. These measured distributions do not change significantly even though the vorticity field (see Figure 3.14) is being distorted. This supports the assumption that the vorticity contained in the interaction blade wake remains at a constant distance from the vortex center even though the fluid

associated with this vorticity is highly turbulent. It is not until the vortex core becomes turbulent at $x/c = 20$ that a marked change in the circulation distribution is seen.
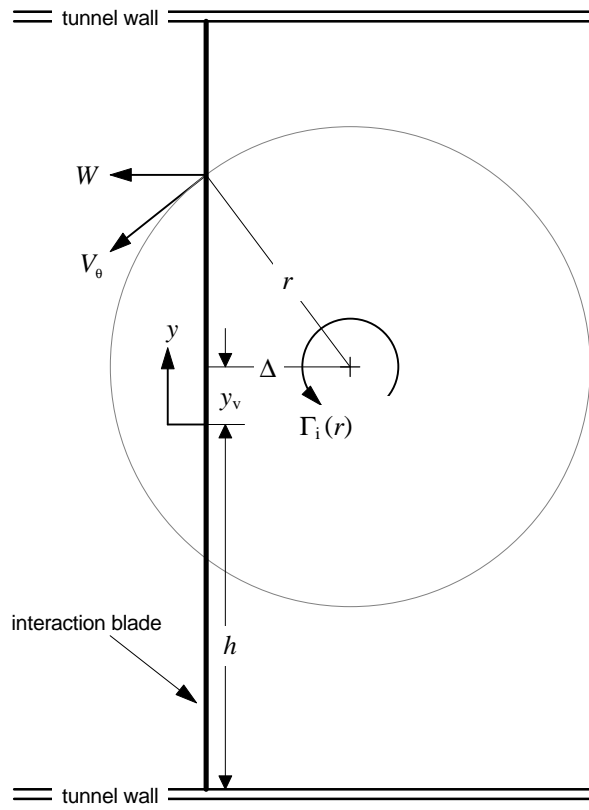
Figure 4.1: Geometry and coordinates used in derivation of theoretical shed vorticity distribution
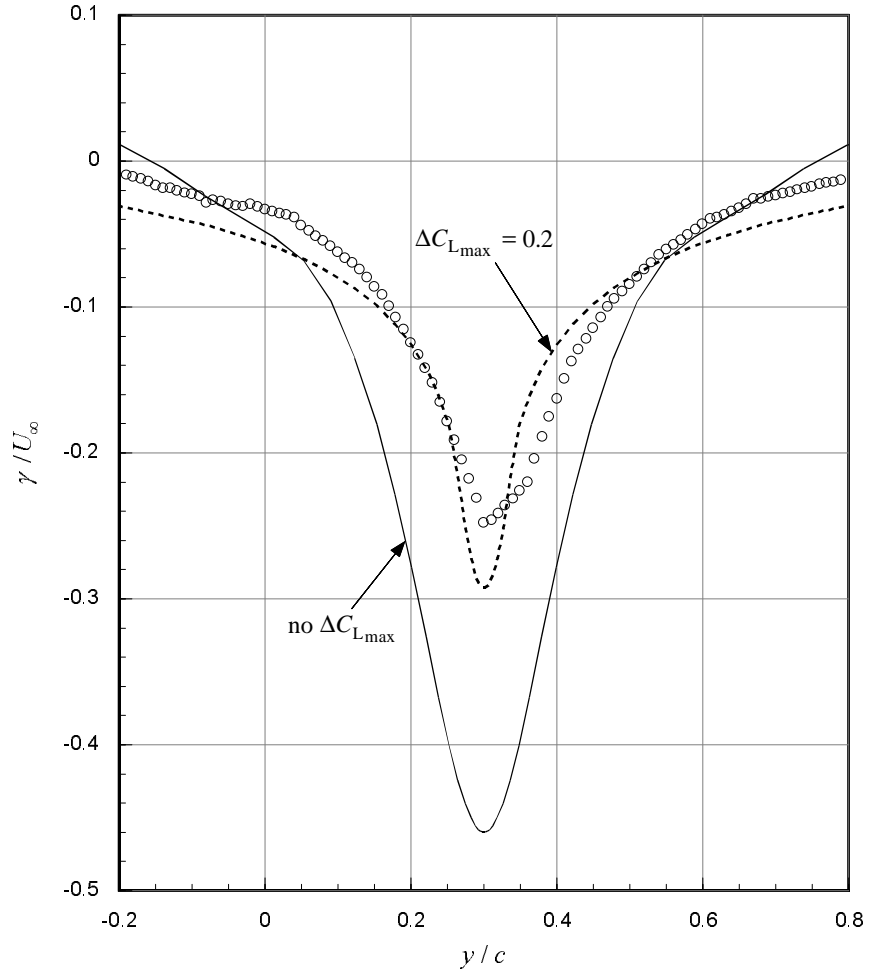
Figure 4.2: Comparison between theoretical and measured shed vortex sheet strengths. Experimental data (symbols) from y-z plane measurements at $x/c = 15.16$ with $\alpha_1 = \alpha_2 = 5°$ and $\Delta/c = -0.125$.
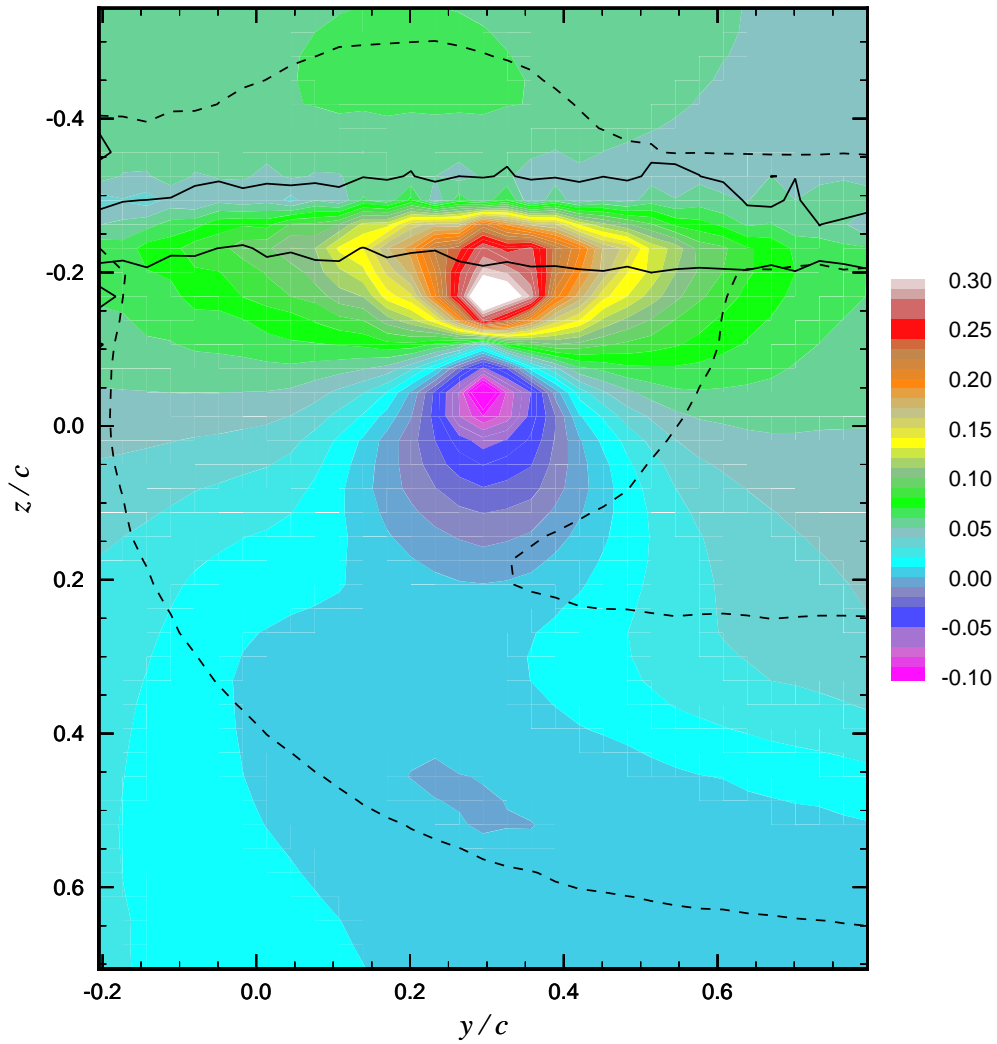
Figure 4.3: Contours of V/U_∞ at $x/c = 15.16$ with $\alpha_1 = \alpha_2 = 5°$ and $\Delta/c = -0.125$. Solid contour line is $\Omega_x c/U_\infty = -0.1$. Dashed contour line is $k/U_\infty = 4 \times 10^5$.
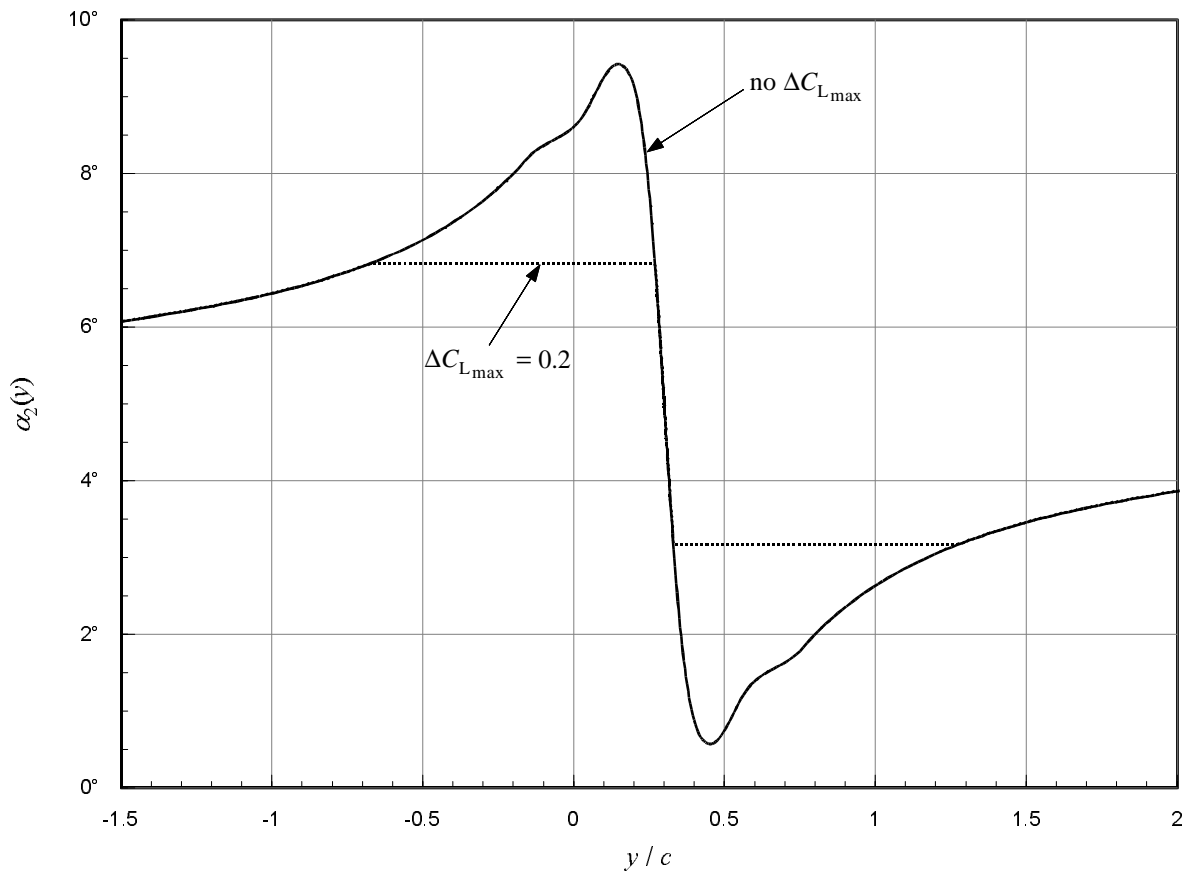
Figure 4.4: Predicted spanwise angle of attack distribution experienced by the interaction blade. $\alpha_1 = \alpha_2 = 5°$ and $\Delta/c = -0.125$
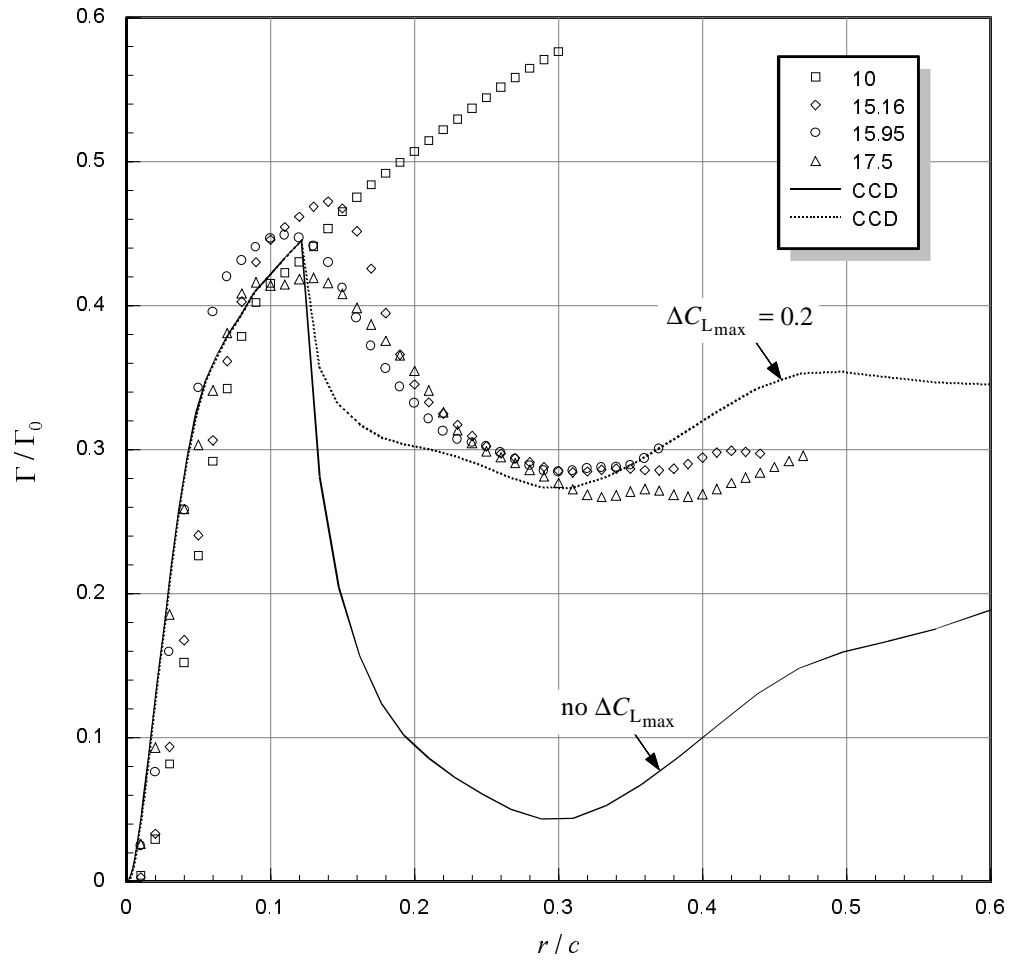
Figure 4.5: Comparison between predicted circulation distributions and the distributions calculated from the y-z plane measurements. Numbers in legend are x/c values.

Chapter 5

Conclusions

The experiments which were performed document the turbulent flowfield resulting from the interaction of a streamwise vortex with an airfoil (referred to as the interaction blade) in incompressible flow. Prior to this study, very little was known about the downstream effects of perpendicular interactions. Interactions were produced using two rectangular NACA 0012 blades of 0.203 m chord at a chord Reynolds number of 530,000. The vortex generator was mounted in the wind tunnel test section as a half wing with 0.879 m extending into the flow. The interaction blade, which completely spanned the 1.85 m test section, was mounted 14 chords downstream. Three-component velocity and turbulence measurements were made using a miniature four-sensor hot-wire probe.

Numerous configurations were studied to determine the extent to which the parameters of blade–vortex separation, vortex strength, and interaction blade angle of attack effect the interaction. The downstream development of the flow was documented in detail for a representative configuration, providing insight into the fluid dynamics responsible for the changes which occur to the vortex and the turbulent flowfield surrounding it. The results of this study should be directly relevant to the helicopter noise prediction problem—BWI noise prediction in particular.

Analysis of the detailed velocity measurements throughout the flowfield support the following conclusions.

1. Even for a close separation of only 3.7 core radii, the vortex core passes the interaction blade virtually unchanged.

2. The strain rates imposed by the vortex on the spanwise vorticity of the interaction blade wake cause an increase in flow anisotropy and therefore an increase in turbulence production.

3. Streamwise vorticity of opposite sign relative to the vortex is contained in the interaction blade wake (due to the angle of attack variation induced by the passing vortex) which imposes an unstable circulation distribution onto the vortex according to Rayleigh's criterion.

4. Although the rotational motion of the core suppresses turbulent fluctuations, the centrifugal

121

instability eventually results in a turbulent vortex core and subsequent reorganization of the vortex to a stable circulation distribution.

5. The reorganization results in a loss of core circulation due to the peak tangential velocity decreasing in a proportion greater than the increase in core radius.

6. As the magnitude of the blade–vortex separation is decreased, the effects on the vortex core increase due to increases in the centrifugal instability and strain rates.

7. Blade–vortex separation effects are largely independent of interaction blade angle of attack and only weakly dependent upon vortex strength.

8. Ultimately, the downstream interaction leaves the vortex surrounded by a large region of intense turbulence which differs considerably from the turbulence surrounding an isolated vortex.

Appendix A

Sample measurement data

To help quantify the importance of the full angle calibration and velocity gradient effects, measurements presented in Section 3.4.1 will be used. In particular, the z-wise profile through the core center at $x/c = 15.95$ shown in Figure 3.23 will be the representative data set (see Figures 3.13–3.18 for y-z plane data).

A.1 Angle calibration corrections

The importance of the angle calibration can be seen by comparing the estimates of the mean velocities U, V, W (Figure A.1) and the turbulence stresses $\overline{u^2}$, $\overline{uw}$ (Figure A.2) are compared to the values obtained after correction with the angle calibration. The largest differences are seen when the V-component of velocity is above $20\% \, U_\infty$, which could be predicted considering the error fractions increase as the edge of the acceptance cone is approached. The corrections in the W-component of the mean velocity are quite small since the mean flow direction is mainly yaw along the profile. Corrections in the $\overline{uw}$ turbulence stress are up to 100% of the estimated value indicating that the angle calibration is even more important when considering turbulence quantities.

A.2 Velocity gradient corrections

The mean velocities along the profile show considerable gradients exist in this flow (Figure A.1). To assess the extent of the effect which these gradients might have on the mean velocity measurements, the analysis described in Section 2.3.3 was performed (*i.e.* Equations 2.22–2.24 were evaluated). To calculate the gradients, the velocities obtained from the angle calibration corrected profile were used in conjunction with the measurements in the y-z plane and the flow was assumed to be axisymmetric in the vicinity of the vortex center. The actual probe dimensions used in the profile measurement (and the calculation) are: $\Delta_y = 0.42 \, \text{mm}$, $\Delta_z = 0.46 \, \text{mm}$, $\theta_1 = 35.6°$,

$\theta_2 = 39.0°$, $\theta_1 = 34.8°$, $\theta_1 = 44.2°$. The predicted effect which the gradients have on the original velocity estimates is shown in Figure A.3.   As can be seen, the effect is very small (less than 1.5% at all locations) even in this example of extreme velocity gradients and a probe geometry which is far from ideal.
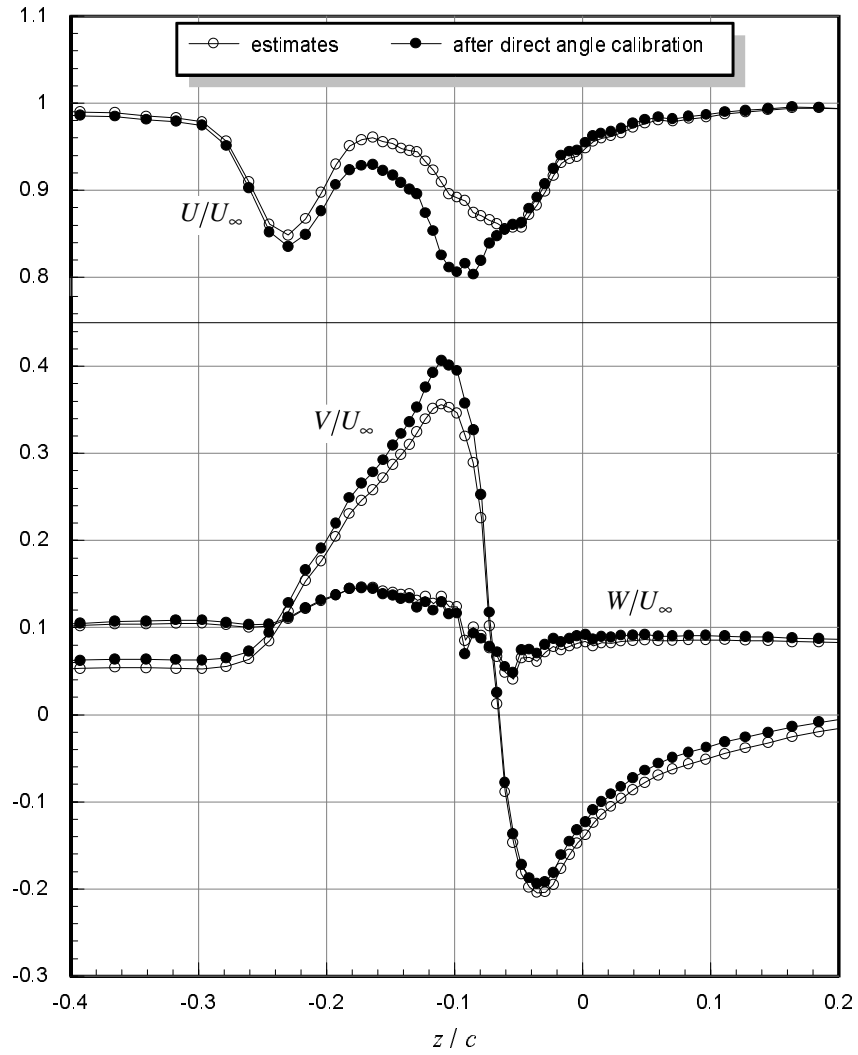
Figure A.1: Comparison between initial estimates and estimates corrected using direct angle calibration of mean velocities measured along a z-wise profile through the core center. $x/c = 30$, $\Delta/c = -0.125$, $\alpha_1 = \alpha_2 = 5°$.
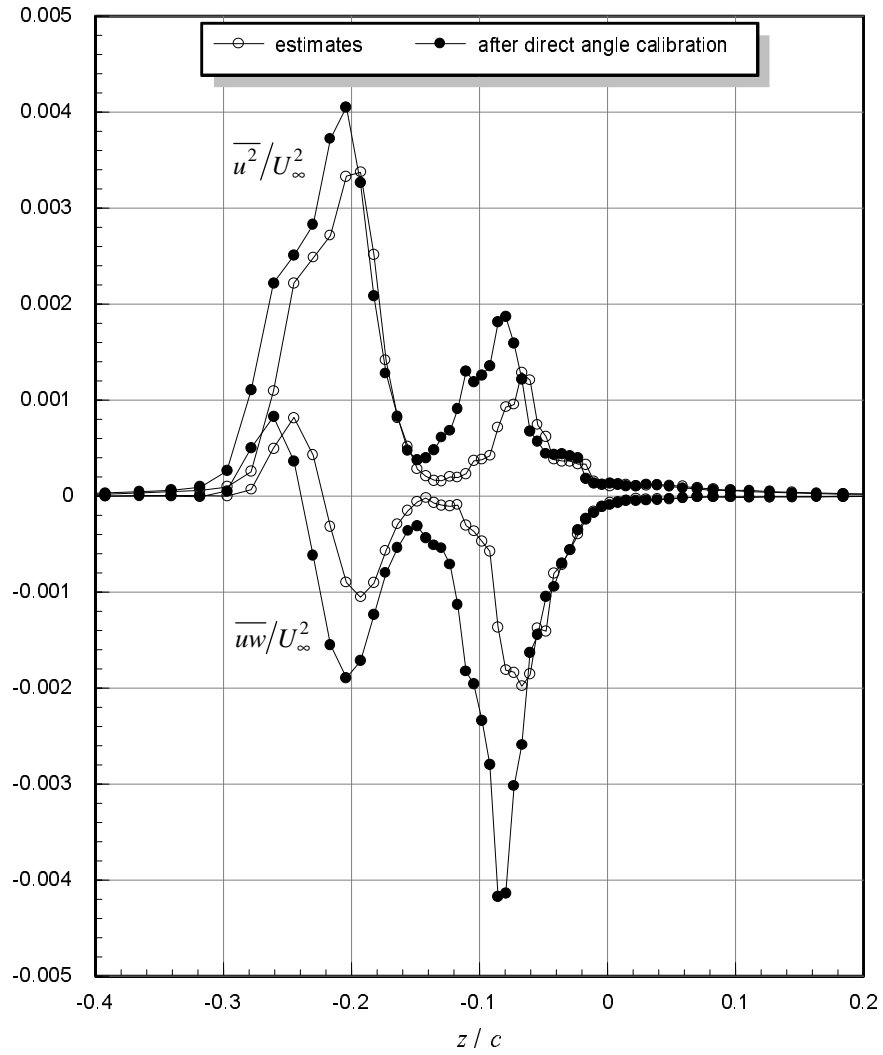
Figure A.2: Comparison between initial estimates and estimates corrected using direct angle calibration of turbulent stresses measured along a z-wise profile through the core center. $x/c = 30$, $\Delta/c = -0.125$, $\alpha_1 = \alpha_2 = 5°$.
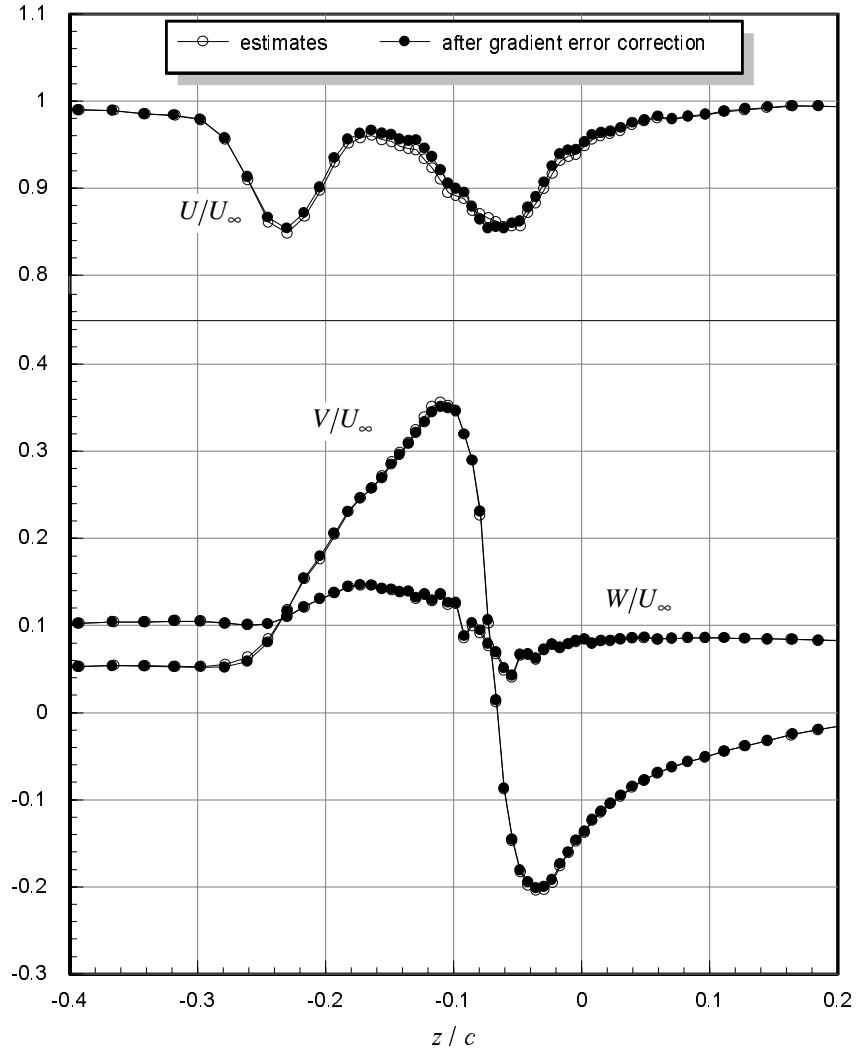
Figure A.3: Comparison between initial estimates and estimates corrected for gradient errors of mean velocities measured along a z-wise profile through the core center. $x/c = 30$, $\Delta/c = -0.125$, $\alpha_1 = \alpha_2 = 5°$.

Bibliography

[1] A. J. Landgrebe. The wake geometry of a hovering helicopter rotor and its influence on rotor performance. 28th Annual National Forum of the American Helicopter Society, May 1972. Preprint no. 620.

[2] I. A. Simons, R. E. Pacifico, and J. P Jones. The movement, structure, and breakdown of trailing vorticies from a rotor blade. In *Proceedings from CAL/USAAVLABS Symposium*, 1966.

[3] W. Johnson. A comprehensive analytical model of rotorcraft aerodynamics and dynamics, part 1, analysis and development. NASA TM-81182, June 1980.

[4] J. S. Preisser, T. F. Brooks, and R. M. Martin. Recent studies of rotorcraft blade–vortex interaction noise. *Journal of Aircraft*, 31(5):1009–1015, Sep–Oct 1994.

[5] A. R. George. Helicopter noise: State-of-the-art. *Journal of Aircraft*, 15(11):707–715, November 1978.

[6] D. R. Hoad. Helicopter model scale results of bladevortex interaction impulsive noise as affected by tip modification. 36th Annual Forum of the American Helicopter Society, May 1980.

[7] T. A. Egolf and A. J. Landgrebe. Helicopter rotor wake geometry and its influence in forward flight, volume 1–generalized wake geometry and wake effect on rotor airloads and performance. NASA CR-3726, October 1983.

[8] S. E. Widnall and T. L. Wolf. Effect of tip vortex structure on helicopter noise due to blade–vortex interaction. *Journal of Aircraft*, 17(10):705–711, October 1980.

[9] J. C. Hardin and S. L. Lamkin. Concepts for reduction of blade/vortex interaction noise. *Journal of Aircraft*, 24(2):120–125, February 1987.

[10] G. R. Srinivasan, W. J. McCroskey, and J. D. Baeder. Aerodynamics of two-dimensional blade–vortex interaction. AIAA Paper 85-1560, July 1985.

[11] H. Tadghighi, A. A. Hassan, and B. Charles. Prediction of blade–vortex interaction noise using airloads generated by a finite-difference technique. *Journal of the American Helicopter Society*, pages 38–47, October 1992.

[12] D. J. Lee and C. A. Smith. Distortion of vortex core during blade/vortex interaction. AIAA Paper 87-1243, June 1987.

[13] T. F. Brooks, M. A. Marcolini, and D. S. Pope. Main rotor broadband noise study in the DNW. *Journal of the American Helicopter Society*, 34(2):3–12, 1989.

[14] W. J. Devenport, S. A. L. Glegg, and G. Sharma. Turbulence measurements in trailing vortices for B.W.I. noise prediction. Report to NASA Langely under grant NAG-1-1119, 1992.

[15] S. A. L. Glegg. The prediction of blade–wake interaction noise based on a turbulent vortex model. *AIAA Journal*, 29(10):1545–1551, October 1991.

[16] K. S. Wittmer, W. J. Devenport, and M. C. Rife. Perpendicular blade vortex interaction. *AIAA Journal*, 33(9):1667–1674, September 1995.

[17] W. J. Devenport, S. A. L. Glegg, K. S. Wittmer, and M. C. Rife. Perpendicular blade vortex interaction and its implications for helicopter noise prediction. Report VPI-AOE-214, VPI&SU, Blacksburg, VA, 1994.

[18] J. W. Leverton. Reduction of helicopter noise by the use of a quite tail rotor. *Vertica*, 6:37–47, 1982.

[19] R. H. Schlinker and R. K. Amiet. Rotor–vortex interaction noise. AIAA Paper 83-0720, April 1983.

[20] J. W. Leverton. Twenty-five years of rotorcraft aeroacoustics: Historical perspective and important issues. *Journal of Sound and Vibration*, pages 261–287, 1989.

[21] J. B. Rorke, R. C. Moffitt, and J. F. Ward. Wind tunnel simulation of full scale vortices. 28th Annual National Forum of the American Helicopter Society, May 1972. Preprint no. 623.

[22] G. J. Follin. The turbulence structure of trailing vortex wakes. Master's thesis, VPI&SU, Blacksburg, VA, 1996.

[23] N. D. Ham. Some preliminary results from an investigation of blade–vortex interaction. *Journal of the American Helicopter Society*, pages 45–48, April 1974.

[24] W. Johnson. Application of a lifting-surface theory to the calculation of helicopter airloads. 27th Annual Forum of the American Helicopter Society, May 1971.

[25] N. D. Ham. Some conclusions from an investigation of blade–vortex interaction. *Journal of the American Helicopter Society*, pages 26–31, October 1975.

[26] M. H. Patel and G. J. Hancock. Some experimental results of the effect of a streamwise vortex on a two-dimensional wing. *Aeronautical Journal*, pages 151–155, April 1974.

[27] G. J. Hancock. Aerodynamic loading induced on a two-dimensional wing by a free vortex in incompressible flow. *The Aeronautical Journal of the Royal Aeronautical Society*, 75:413–416, June 1971.

[28] R. W. Paterson, R. K. Amiet, and C. L. Munch. Isolated airfoil–tip vortex interaction noise. *Journal of Aircraft*, 12(1):34–40, January 1975.

[29] J. J. Phillipe and C. Armand. Onera aerodynamic research on helicopters. *Rotorcraft Design*, January 1978. AGARD CP-223.

[30] D. D. Seath and D. R. Wilson. Vortex–airfoil interaction tests. AIAA Paper 86-0354, January 1986.

[31] R. H. G. Müller. Special vortices at a helicopter rotor blade. *Journal of the American Helicopter Society*, pages 16–22, October 1990.

[32] I. M. Kalkhoran, D. R. Wilson, and D. D. Seath. Experimental investigation of the perpendicular rotor blade–vortex interaction at transonic speeds. *AIAA Journal*, 30(3):747–755, March 1992.

[33] K. Choi and R. L. Simpson. Some mean-velocity, turbulence, and unsteadiness characteristics of the VPI&SU Stability Wind Tunnel. Report VPI-AOE-161, VPI&SU, Blacksburg, VA, 1987.

[34] L. S. G. Kovasznay. *Physical Measurements in Gas Dynamics and Combustion*, page 227. Princeton University Press, 1954.

[35] F. E. Jorgensen. Directional sensitivity of wire and fiber-film probes. *DISA Information*, (11):31–37, May 1971.

[36] K. Mathioudakis and F. A. E. Breugelmans. Use of triple hot wires to measure unsteady flows with large direction changes. *Journal of Physics E: Scientific Instruments*, 18:414–419, 1985.

[37] L. B. W. Browne, R. A. Antonia, and L. P. Chua. Calibration of X-Probes for turbulent flow measurement. *Experiments in Fluids*, 7:201–208, 1989.

[38] R. M. Leuptow, K. S. Breuer, and J. H. Haritonidis. Computer-aided calibration of X-probes using a look-up table. *Experiments in Fluids*, 7:201–208, 1988.

[39] K. Döbbeling, B. Lenze, and W. Leuckel. Computer-aided calibration with a quadruple hotwire probe. *Experiments in Fluids*, 8:257–262, 1990.

[40] P. W. Bearman. Corrections for the effect of ambient temperature drift on hot-wire measurements in incompressible flow. *DISA Information*, (11):25–30, May 1971.

[41] P. Vukoslavĉević and J. M. Wallace. Influence of velocity gradients on measurements of velocity and streamwise vorticity with hot-wire X-array probes. *Review of Scientific Instrumentation*, 52(6):869–879, 1981.

[42] A. D. Cutler and P. Bradshaw. A crossed hot-wire technique for complex turbulent flows. *Experiments in Fluids*, 12:17–22, 1991.

[43] W. J. Devenport, M. C. Rife, S. I. Liapis, and G. J. Follin. The structure and development of a wing-tip vortex. *Journal of Fluid Mechanics*, 312:67–106, 1996.

[44] G. K. Batchelor. Axial flow in trailing line vortices. *Journal of Fluid Mechanics*, 20:645–658, 1964.

[45] D. W. Moore and P. G. Saffman. Axial flow in laminar trailing vortices. In *Proceedings of the Royal Society of London A*, volume 333, pages 491–508, 1973.

[46] A. Betz. Behavior of vortex systems. NACA TM 713, June 1933.

[47] V. J. Rossow. On the inviscid rolled-up structure of lift-generated vortices. *Journal of Aircraft*, 10(11):647–650, November 1973.

[48] C. duP. Donaldson, R. S. Snedeker, and R. D. Sullivan. Calculation of aircraft wake velocity profiles and comparison with experimental measurements. *Journal of Aircraft*, 11(9):547–555, September 1974.

[49] M. K. Sreedhar and S. A. Ragab. Large eddy simulation of a longitudinal vortex. AIAA Paper 94-0529, January 1994.

[50] E. W. Mayer and K. G. Powell. Similarity solutions for viscous vortex cores. *Journal of Fluid Mechanics*, 238:487–507, 1992.

[51] S. A. Ragab and M. K. Sreedhar. Numerical simulation of vortices with axial velocity deficits. *Physics of Fluids*, 7:549–558, 1995.

[52] H. Tennekes and J. L. Lumley. *A First Course in Turbulence*. The MIT Press, 1972.

[53] M. C. Rife and W. J. Devenport. Flow visualizations of perpendicular blade vortex interactions. Report VPI-AOE-197, VPI&SU, Blacksburg, VA, 1993.

[54] L. T. Filotas. Finite chord effects on vortex induced wing loads. *AIAA Journal*, 11(6):888–890, June 1973.

[55] I. H. Abbott and A. E. von Doenhoff. *Theory of Wing Sections*. Dover Publications, Inc., 1959.

Vita
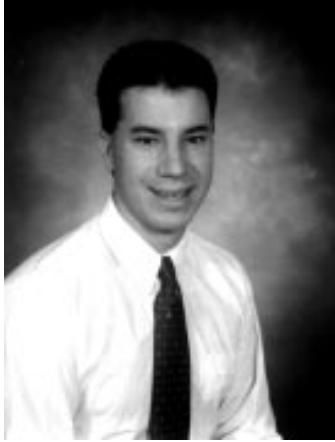
Kenneth S. Wittmer

Education:

B.S. Aerospace Engineering, May 1992, Virginia Tech, Blacksburg, VA

Magna Cum Laude, Commonwealth Scholar, Minor in Mathematics

Summer study abroad at Oxford University, England, 1989

High School Diploma, June 1988, Newtown High School, Sandy Hook, CT

Employment:

Research/Teaching Assistant, August 1992-November 1996, Aerospace and Ocean Engineering Department of Virginia Tech

JOURNAL PUBLICATIONS:

K. S. Wittmer, W. J. Devenport, and M. C. Rife. Perpendicular blade vortex interaction. *AIAA Journal*, 33(9):1667–1674, September 1995.

CONFERENCE PUBLICATIONS:

K. S. Wittmer and W. J. Devenport. Turbulence structure resulting from a perpendicular airfoil–vortex interaction. AIAA Paper 96-2014, June 1996.

K. S. Wittmer and W. J. Devenport. Interaction of a streamwise vortex with a full–span blade. AIAA Paper 95-2214, June 1996.

Computer Consultant, April–October 1994, Virginia Tech Computing Center

Engineering Consultant, August–September 1993, Butler Service Group, Inc., Shelton, CT

Developed a computer model to predict the unsteady forces and moments on a helicopter tail rotor during a maneuver

Engineering CO-OP Student, May–August 1991, 1992, 1993, Sikorsky Aircraft, Stratford, CT

Contributed to the engine simulation and validation program for the MH-53E-419 Super Stallion helicopter

Evaluated the trim and maneuvering loads incurred by the VH-3D Executive helicopter

Contributed to the design analysis of the CYPHER unmanned air vehicle by generating stability derivatives and correlating the computer generated results to wind tunnel test data

Evaluated the maneuvering charateristics of the S-76 FANTAIL helicopter with a bearingless main rotor

Tutor, January–May 1992, College of Engineering, Virginia Tech

Computer Consultant, September 1991–May 1992, College of Engineering, Virginia Tech